Faculdade de Engenharia da Universidade do Porto

Biomechanical simulation of erythrocytes and ovalocytes cells

Sara Daniela da Silva Ferreira

PROVISIONAL VERSION

Thesis submitted to Faculdade de Engenharia da Universidade do Porto as a requirement to obtain the MSc Degree in Biomedical engineering

Supervisor: Prof. Dr. Jorge Américo Oliveira Pinto Belinha
Co-Supervisor: Prof. Dr. Renato Manuel Natal Jorge

June 2018

U.PORTO
FEUP FACULDADE DE ENGENHARIA UNIVERSIDADE DO PORTO

MEB – MESTRADO EM ENGENHARIA BIOMÉDICA 2017/2018

A Dissertação intitulada

"Biomechanical Simulation of Erythrocytes and Ovalocytes Cells"

foi aprovada em provas realizadas em 05-07-2018

o júri

Presidente Prof. Doutor João Manuel Ribeiro da Silva Tavares
Professor Associado c/ Agregação do Departamento de Engenharia Mecânica da FEUP - U.Porto

Doutor Jorge Americo Oliveira Pinto Belinha
Investigador Pós-Doutoramento do Instituto de Ciência e Inovação em Engenharia Mecânica e Engenharia Industrial da U. Porto - INEGI - U.Porto

Doutora Carla Maria da Cunha Roque
Investigadora do Instituto de Ciência e Inovação em Engenharia Mecânica e Engenharia Industrial da U. Porto

O autor declara que a presente dissertação (ou relatório de projeto) é da sua exclusiva autoria e foi escrita sem qualquer apoio externo não explicitamente autorizado. Os resultados, ideias, parágrafos, ou outros extratos tomados de ou inspirados em trabalhos de outros autores, e demais referências bibliográficas usadas, são corretamente citados.

Autor - Sara Daniela da Silva Ferreira

Faculdade de Engenharia da Universidade do Porto

Abstract

The red blood cells (RBCs) are the highest concentration component in blood. These cells can modify their biomechanical properties due to various pathologies. The treatment methods available for these conditions are often expensive and not always effective.

With this dissertation, it is intend to open a new path to a possible treatment method based on the assumption that all bodies have a natural vibration frequency. Thus, the purpose of this dissertation is to determine the natural vibration frequency of healthy RBCs and pathological RBCs. With these frequencies, it will be possible to create a new treatment based inducing the natural frequencies (by means of external sound sources) to destroy the ill RBCs. Thus, efforts will be made to find the first vibration frequencies of three distinct forms of RBCs: one in the form of a biconcave disc (healthy), another oval and the last sickle-shaped. The latter two forms are associated with ovalocytosis and sickle cell anemia, respectively.

In this dissertation, a bi-dimensional model and a three-dimensional model of a three RBCs: healthy, with sickle anemia and with ovalocytosis were constructed. These models were used to determine the deformation, the effective stress of Von Mises and the equivalent strain experimented by the cell when a force is applied to it in a certain direction. For these models the first three modes of vibration were also determined. The discrete numerical techniques used were the finite element method (FEM) and the meshless methods (MMS) RPIM and NNRPIM.

Resumo

As células vermelhas do sangue (RBCs) constituem o componente em maior concentração no sangue. Estas células podem alterar as suas propriedades biomecânicas devido a diversas patologias. Os métodos de tratamento disponíveis para essas patologias são muitas vezes dispendiosos e nem sempre eficazes.

Nesta dissertação procura-se abrir caminho para um possível novo método de tratamento baseado no pressuposto de que todos os corpos possuem uma frequência de vibração natural. Deste modo, o objetivo desta dissertação é a determinação da frequência de vibração naturais das RBCs saudáveis e das RBCs com patologia. Descobertas estas frequências, é possível criar um novo tratamento baseado na aplicação das vibrações corretas para destruir as RBCs com patologia. Assim serão feitos esforços para encontrar as frequências de vibração de três formas distintas de RBCs: uma em forma de um disco achatado (forma saudável), outra oval e outra em forma de foice. As duas últimas formas estão associadas às patologias ovalocitose e anemia falciforme, respectivamente.

Nesta dissertação foi construído um modelo bidimensional e um modelo tridimensional de três tipos de eritrócitos: saudáveis, com anemia falciforme e com ovalocitose. Esses modelos foram usados para determinar a deformação, a tensão efetiva de Von Mises e a tensão equivalente experimentada pela célula quando uma força é aplicada com uma determinada direção. Para esses modelos, os três primeiros modos de vibração também foram determinados.

As metodologias utilizadas foram o método dos elementos finitos (FEM) e os métodos sem malha (MMS) RPIM e NNRPIM.

Agradecimentos

Esta dissertação marca o fim de uma etapa muito importante da minha vida, e como tal não posso deixar de estar grata por todos os incentivos e apoio recebido ao longo destes 5 anos.
Ao professor Doutor Jorge Américo Pinto Belinha agradeço a oportunidade, o seu incentivo e todo o empenho demonstrado na procura de soluções para os inúmeros problemas que surgiram ao longo da dissertação.
Aos meus avós obrigada pelo exemplo humilde, por todo o carinho e motivação para lutar sempre pelos meus objetivos.
À minha irmã agradeço todos os conselhos e a sua alegria contagiante.
Às minhas amigas de sempre Sílvia, Ana e Tânia obrigada por estarem sempre presentes em todos os momentos importantes.
À Helena e à Catarina obrigada pelo companheirismo e apoio ao longo destes dois anos.
A ti Simão obrigada por toda a motivação, ajuda e calma para resolver todos os problemas.
E como sem eles nada disto era possível deixo um agradecimento muito especial aos meus pais que são um exemplo de coragem, determinação. Obrigada pelo vosso amor e compreensão e pela vossa luta diária, em busca de um futuro melhor para as vossas filhas.

Institutional Acknowledgments

The author truly acknowledges the work conditions provided by the Applied Mechanics Division (SMAp) of the department of mechanical engineering (DEMec) of Faculty of Engineering of the University of Porto (FEUP), and by the MIT-Portugal project "MIT-EXPL/ISF/0084/2017", funded by Massachusetts Institute of Technology (USA) and "Ministério da Ciência, Tecnologia e Ensino Superior - Fundação para a Ciência e a Tecnologia" (Portugal).

Additionally, the authors gratefully acknowledge the funding of Project NORTE-01-0145-FEDER-000022 - SciTech - Science and Technology for Competitive and Sustainable Industries, cofinanced by Programa Operacional Regional do Norte (NORTE2020), through Fundo Europeu de Desenvolvimento Regional (FEDER).

Finally, the author acknowledges the synergetic collaboration with the collaborators of "Computational Mechanics Research Laboratory CMech-Lab" (ISEP/FEUP/INEGI), and its director, Prof.Dr. Jorge Belinha, and its senior advisors, Prof.Dr. Renato Natal Jorge and Prof.Dr. Lúcia Dinis.

Contents

List of Figures

List of tables

Abbreviations

List of abbreviations

2D	*Bidimensional*
3D	Tridimensional
FEM	Finite Element Method
FEMAS	Finite Element and Meshless Method Analysis Software
NNRPIM	Natural Neighbor Radial Point Interpolation Method
RPIM	Radial Point Interpolation Method
SPH	Smooth Particle Hydrodynamics Method
MMs	Meshless methods
RBCs	Red blood cells
PO_2	Oxygen pressure
Hb	Hemoglobin
ATP	Adenosine 5-triffosphate
HS	Hereditary spherocytosis
HE	Hereditary elliptocytosis
O	Ovalocytosis
SC	Sickle cell anemia
H	Healthy
MAX	Maximum
MIN	Minimum

Chapter 1

Introduction

RBCs have high biological importance since they are responsible for the oxygenation of all cells, tissues and organs of living organisms. These cells have a high deformability, allowing them to cross narrow capillaries. The mentioned deformability depends on several factors such as its geometry, the elasticity of the membrane and its internal and external viscosity.

Scientific studies have suggested that certain pathologies are associated with changes in the deformability of RBCs. Among these diseases stand out cancer, malaria, diabetes, Alzheimer's disease, spherocytosis, the elliptocytosis and sickle cell anemia. These diseases represent a real challenge for researchers around the world. The need to research these diseases is visible from the numbers of new diagnosis and deaths arising every day around the world.

Every second elapsed, new diagnoses of cancer are attributed. The severity of this disease and the high percentages of new diagnoses determine the need to know the causes, the methods of progression, the possible treatments as well as the way of prevention. Similarly, malaria affects a high proportion of the population, accounting for 2-3 million deaths a year (Suresh 2006). Their treatment often entails high costs for families, who in most cases live with a very low financial condition. With a likewise alarming data, diabetes in 2011 caused the death of 4.6 million people in the age group of 20 to 79 years (Pereira et al. 2013). In Europe, Portugal is the country with the most diabetics (Sousa-uva et al. 2016).

However, it is important to note that in the last decades many scientific advances have emerged, particularly in the field of computational biomechanics. The development of computers is seen in many situations as one of the main responsible for current scientific discoveries.

It is well known that independently of they are at rest or not, all bodies have their own natural vibration frequency. From this point of view and in order to open the way for future

studies, in this thesis it will be carried out a computational simulation of healthy RBCs and pathological RBCs.

To simulate these cells, it will be used a meshless method. This numerical method (unlike the finite element method) does not require the discretization of the problem in elements. In short, what is proposed for this thesis is to determine the natural frequency of vibration of healthy RBCs and pathological RBCs, opening new ways to new forms of treatments based on the induction of a resonance vibration (equal to the pathological RBC natural frequency) to potentially destroy only the pathological cells.

1.1 – Motivation

An in-depth knowledge of the mechanisms, functions and structure of RBCs is of utmost importance. RBCs appear to exhibit distinct biomechanical properties in certain pathologies. These pathologies affecting the quality of life of millions of people around the world and which entail very expensive costs for families and for the state. In this way, the implementation of biomechanical simulations of RBCs arouses an increased interest.

1.2 – Objectives

This thesis aims to take the first steps for creating a possible new treatment method based on the assumption that all bodies have a unique vibration frequency. Thus, it is proposed the construction of a new three-dimensional model based on the elastic constitutive model and using the Radial Point Interpolation Method (RPIM) and Natural Neighbor Radial Point Interpolation Method (NNRPIM), both meshless methods (MMs).

Since, for the simulation of RBCs, it is the first time that a meshless methods is going to be applied, simple elastic material assumptions will be considered. It is also proposed to include the constituents of the membrane and the spectrin network existent in the RBCs.

After constructing the model, the natural vibration frequency of healthy RBCs and pathological RBCs will be determined. Thus, efforts will be made to find the natural vibration frequencies of three distinct forms of RBCs: one in the form of a biconcave disc (healthy form), another oval and another in sickle shape. The latter two forms are associated with ovalocytosis and sickle cell anemia.

1.2 - Document outline

This dissertation consists of eight chapters: Introduction, Red Blood Cells, Numerical Methods, Solid mechanics, State of art the review, Red blood cells static analisis, Red blood cells- free vibrations and Important Conclusions and Future Work. To facilitate the understanding of the organization of the dissertation, a summary of each of the chapters is presented below:

Chapter 1: Introduction

Introduction and contextualization of the subject of study and the intended objectives.

Chapter 2: Red Blood Cells

Socioeconomic context of the presented problem. Description of structure, function, composition of RBCs. Bibliographical review of some of the many pathologies that appear to be associated with changes in the biomechanical properties of RBCs.

Chapter 3: Numerical Methods

Presentation and description of numerical methods available for simulations of RBCs.

Chapter 4: Solid mechanics

Basics of solids mechanics relevant to the context of the problem.

Chapter 5: State of art the review

Presentation of the relevant scientific studies developed in the last decades. Description of some numerical techniques available for simulations with RBCs.

Chapter 6: Red blood cells – static analysis

Preliminary studies: The convergence of different nodal meshes was studied for three different numerical methods. It was also determined the deformation, the effective stress of Von Mises and the equivalent strain experimented by the cell when a force is applied to it in a certain direction for a 2D and 3D models. Additionally, in this preliminary study, the cell is subject to two distinct boundary conditions.

Chapter 67: Red blood cells – free vibrations

Study of the first three modes of vibration for healthy cells, with sickle cell anemia and with ovalocytosis, for three numerical methods.

Chapter 8: Conclusions and Future Work

Presentation of the preliminary conclusions obtained, as well as future plans.

Chapter 2

Red Blood Cells

2.1 - Social and economic impact

The knowledge of the structure and function of red blood cells is of highest importance, since the alterations in these cells seem to be associated with several pathologies, such as malaria, diabetes, Alzheimer's disease, hereditary spherocytosis, ovalocytosis, sickle cell anemia, among others. Thus, it is possible to affirm that the biomechanical properties of the RBCs and in particular their capability of deformability have a high pathophysiological importance. Thus, changes in the properties of RBCs function as biomarkers of certain pathologies. These pathologies imply high costs for the state and for the families. Thus, a policy of prevention, together with a detailed knowledge of the RBCs, can lead to a reduction of costs and an improvement in the well-being of the population.

The diabetes is one of the major public health problems causing a high number of deaths worldwide and leading to comorbidities such as amputations, kidney failure and blindness.

A global study for the 20 to 79 age group was conducted in 2011 and it was concluded that 4.6 million died from diabetes in that year (Pereira et al. 2013). Portugal is the country with the highest incidence rate of diabetes in Europe. It is estimated that each year there is an average increase of 4.29% in new cases of diabetes in Portugal. Given that, this disease does not seem to be gender dependent, since to the year 1998 the number of cases of women with diabetes was greater than that of men, but between 1998 and 2000 and from 2013 to 2015 men were the most affected ones (Sousa-uva et al. 2016). It is predicted that between 2022 and 2024 this disease has an incidence rate of 972.77 in each 10^5 inhabitants. So in order to soften this disturbing scenario it is necessary to make research advances in the disease of

diabetes (Pereira et al. 2013),(Sousa-uva et al. 2016). Diabetes is treated in several situations by the administration of insulin or other drugs.

The treatment of diabetes entails direct and indirect costs to the bearer. The direct costs relate to all treatment including medication, monitoring equipment, hospitalizations and the treatment of complications that may arise. While indirect costs are associated with reduced productivity and premature death. A study carried out in 2016 revealed that in 2011 in Norway the minimum cost of treating diabetes was 516 million of euros. Of which, 408 million of euros is related to direct costs and 108 million of euros to indirect costs. It should also be noted that the share of the treatment of complications does not represent the greatest cost. The highest cost is related with the prevention of vascular complications (Sørensen et al. 2016),(Bommer et al. 2017).

Another socio-economic study was conducted in 184 countries. These countries were divided into three groups according to the average family income (high, medium, low). Given that the direct costs to the high income are approximately $ 510.70 billion, for the average income are approximately $ 344.69 billion and for a low income is $ 1.57 billion. As for the indirect costs, for the high income represents $ 293.66 billion, for the average income represents $ 160.20 billion and for low income $ 0.95 billion (Bommer et al. 2017).

Another of the pathologies associated with alteration of biomechanical properties of RBCs is malaria. In Portugal, Malaria is an eradicated disease, but it is a very active disease in Africa, especially in the former colonies of Portugal. Although eradicated in Portugal, each year new malaria diagnoses appear in Portuguese hospitals. These diagnoses come from people who have traveled to countries where there is a high incidence of malaria. A study revealed that between 2004 and 2009, 160 cases of malaria were diagnosed at Joaquim Urbano Hospital. Most of the diagnoses were from people who had visited Angola (57.5%), followed by Mozambique (14.4%) and Sao Tome and Principe (4.8%). In several cases it was not possible to identify the parasite that caused malaria. Of the cases where it was possible to diagnose the parasite that caused malaria, Plasmodium falciparum produced the most positive tests, representing 19.3% of the cases followed by Plasmodium vivax with 16.25% of the cases (Anon 2009).

A study in the year 2015 revealed that funding for malaria reduction/elimination was $ 2.9 billion. Investment in prevention is beneficial, saving over $ 49 billion, as it leads to a reduction in the incidence of many diseases and a decrease in the number of deaths (Shretta et al. 2017).

A socio-economic study of the impact of malaria on a total of 1655 families, 828 in Mozambique and 827 in South Africa has revealed that the cost associated with treating a malaria episode can be catastrophic for some families. These two countries are very unequal in the health system. In South Africa, there is 1 doctor per 1300 inhabitants while in

Mozambique there is only 1 in 33,300 inhabitants. As for per capita health expenditure, in 2006 in South Africa was $ 669 and in Mozambique only $ 45. In southern Africa, primary malaria treatment services are free and in Mozambique only children under 5 years are exempt. For the remaining population is charged a fee of 500 meticais (approximately 0.02 $) per consultation and 500 meticais per medical revenue. In the case of secondary and tertiary services the consultation costs 1000 meticais (Castillo-riquelme, Mcintyre, and Barnes 2008). Table 2. 1 shows some of the costs associated with malaria treatment (Castillo-riquelme et al. 2008).

Other studies in different countries of sub-Saharan Africa have been carried out with costs varying from $ 6.40 in Ghana to $ 17.20 in Sudan. In Malawi, in non-governmental facilities, each Malaria episode on average costs $ 17.48. At government facilities this cost is approximately $ 12.70, significantly lower (Hennessee et al. 2017).

Nowadays, many research works have detected changes in the deformability and other biomechanical properties of RBCs during certain states of some diseases (Mohandas et al. 2014; Suresh 2006; Tomaiuolo 2014). However, understanding the role of this biomechanical changes in certain pathologies is far from being fully characterized. It is therefore emerging the development of dynamic models that allow clarifying the implications of certain changes in different pathologies. That is, it is necessary to create a correlation between the pathology identified in a given patient and the biomechanical properties of the RBCs. This is only possible by carrying out a colossal number of experimental studies for the most diverse pathologies (Tomaiuolo 2014).

Table 2. 1- Costs associated with malaria treatment in 2006 for Mozambique and South Africa (Castillo-riquelme et al. 2008)

		Mozambique	South Africa	
		Maputo Province	KwaZulu Natal Province	Mpumalanga Province
Total households		828	436	391
Per capita annual expenditure on health ($) *		45	669	
Average monthly income ($)		36	109	222
% of households where at least one member had been hospitalized for malaria		10	29	26
Hospital costs as % of monthly income		16.6	0.65	1.0
Household with catastrophic impact with		32.6	4.7	4.7
both measures				
Number of deaths		21	19	13
Cost categories ambulatory care ($)	Transport patient	1.82	1.18	0.99
	Transport caregiver	1.79	0.64	0.65
	Cost of medicines	2.53	0.06	0.20
	Consultation fees	0.18	0.01	0.19
	Cost malaria test	0.05	0.00	0.00
	Other costs (while waiting)	0.18	0.40	0.17
	Total mean ambulatory expenditure	6.54	2.28	2.20

2.2- Biology of blood cells/cell level

2.2.1- Structure

The RBCs represent a relatively simple biological structure because they do not have intramembrane organelles or nucleus. The membrane of RBCs acts as a complex of multi-components interconnected with each other, so that the cell maintains its integrity, mechanical properties and biological functions. It is believed that the plasma membrane is responsible for the shape of RBCs and shape changes along the circulatory system.

In the year 1991, it was discovered the evidence that important features functional and structural of red blood cell plasma membrane have been conserved during the evolution. It is also known the red blood cells plasma membrane is constituted by four layers. Two fluid lipid monolayers, the integral membrane proteins and one elastic protein network (underlies the bilayer). The two fluid lipid monolayers and the layer of elastic protein network can slide freely relative to one another (Elgsaeter and Mikkelsen 1991).

The phospholipid bilayer is characterized by a low shear resistance, however, is essential to improve bending resistance and to maintain cell surface area and the elastic protein network is the biggest responsible for the shear elastic properties of the RBC (Elgsaeter and Mikkelsen 1991). The interaction between the membrane skeleton proteins and the phospholipid bilayer through the transmembrane proteins is responsible for the integrity and strength of the red blood cells membrane (Chasis and Shohet 1987).

Over the years many researchers have devoted their studies to understanding the membrane composition of RBCs (Tse and Lux 1999). In performing such studies, osmotic hemolysis using dilute alkaline buffer is used in many situations. In one of these studies it was concluded that 52% of the RBCs membrane is protein, 40% is lipids and 8% carbohydrates (Steck 1974).

The Figure 2.1 represents a diagram of the RBCs membrane where it is possible to visualize the vertical and horizontal interactions, as well as some of its constituents: the band 3, the protein 4.2, the Ankyrin, α and β spectrin, the protein 4.1.

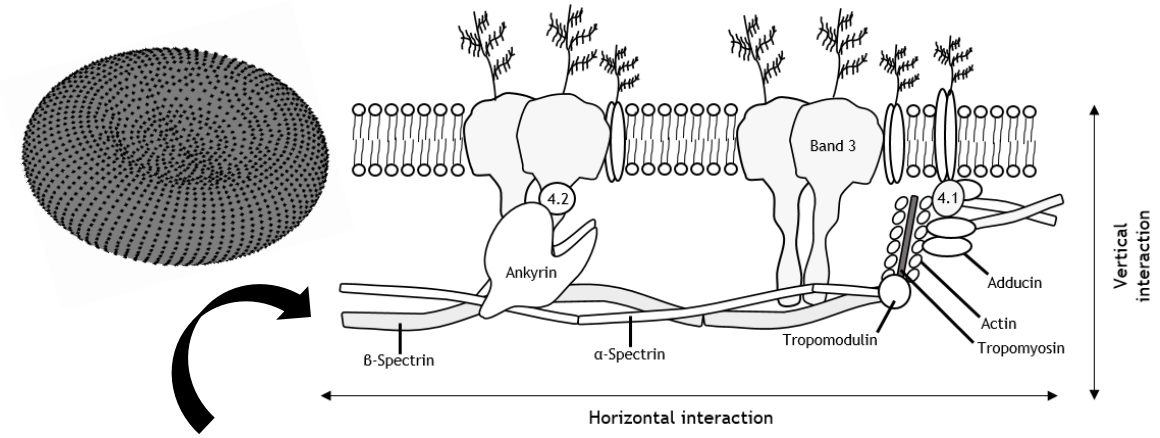

Figure 2.1 - Diagram of the RBCs membrane.

Membrane lipids

The cell membrane possesses one lipid bilayer that is composed of lipids, these structural elements have a hydrophilic/polar head group region and a hydrophobic/non-polar tail. The lipid bilayer is semipermeable, therefore it acts as a barrier between the extracellular medium and the intracellular medium.

In the constitution of the bilayer is formed by four phospholipids: the phosphatidylcholine, the sphingomyelin, the phosphatidylethanolamine and the phosphatidylserine. These four phospholipids are not arranged symmetrically in the two monolayers. In the outer monolayer, it essentially contains sphingomyelin and phosphatidylcholine while the inner monolayer essentially contains phosphatidylserine and phosphatidylethanolamine. The asymmetry of the membrane should be maintained otherwise there may be loss of function. A simple exposure of phosphatidylserine would lead to the cell being destroyed prematurely by macrophages. Nowadays it is known that this asymmetry is maintained by proteins, in particular by flipases and floppases. The flipases are responsible for the movement of the phospholipids from the outer leaflet to the inner leaflet, while the floppases are responsible for the opposite movement. Other proteins can be involved in the movement of the phospholipids in the membrane. It is important to note that lipids are active elements in the cell membrane because they can act directly on intramembrane proteins, altering the structural properties of the bilayer or lipid metabolism (Mohandas et al. 2014).

Membrane proteins

In the cell membrane several proteins with many different functions are present. Among these proteins, transport proteins and adhesion proteins stand out. In order to maintain the integrity of the cell, it is necessary that those proteins perform changes between the outer

medium and the inner medium. Such exchanges are mediated by transport proteins such as aquaporia (involved in the transport of water) or Band 3 (involved in the transport of ions and water). It is also important to note that in various situations the cells need to communicate with other blood cells, with other red cells or with endothelial cells. For such function, the action of adhesion proteins such as laminin and ICAM-4 is crucial (Mohandas et al. 2014),(Apostoli et al. 1988).

Skeletal proteins

The protein skeleton is responsible for plasticity and deformability of the RBCs. The elastic protein network, often referred to as membrane skeleton, is composed of α and β-spectrin, proteins 4.1, actin, aducin, dematin, tropomyosin and tropomodulin.

α and β-spectrin: The largest fraction of the membrane skeleton is occupied by the spectrin. This protein is present in 10^5 tetramers per cell. This protein represents 25% of the membrane proteins of the RBCs and 75% of the skeletal proteins. The spectrin consists of two α and β subunits. The α subunit is composed of 2429 amino acids while the β subunit is composed of 2137 amino acids. Although they have a similar structure the function of the α and β subunits is different. The α and β subunits can bind to form heterodimers, tetramers, or oligomers. The spectrin proteins are mainly responsible for the shape of the cell because they have a high flexibility. The behavior of spectrin can be compared to the behviour of a spring. Their tetramers are coiled in the resting state but may become stretched when subjected to shearing forces. The spectrins can be associated by two different mechanisms. In the first mechanism, there is a head-to-head link, while in the second mechanism there is a side-to-side link. It is possible to visualize head-to-head association in the Figure 2.2.

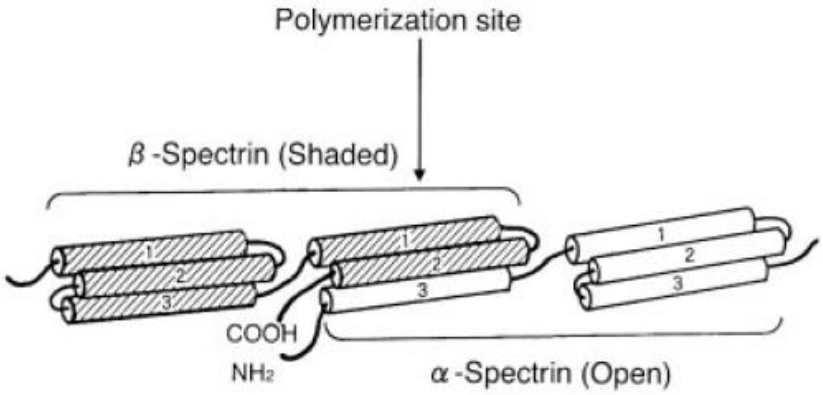

Figure 2.2 - Head-to-head association of spectrin (Yawata 2003).

The spectrin network binds through the ankyrin the particles present in the membrane. The purpose of this connection is to change the density of the cell in case of need (Elgsaeter and Mikkelsen 1991),(Mohandas et al. 2014),(Chasis and Shohet 1987),(Yawata 2003).

Protein 4.1: Protein 4.1 represents a globular protein that is present in 200×10^3 copies per RBCs. In RBCs two forms of this protein can be identified. The 4.1 α protein with a molecular weight of 80 kDa and the protein 4.1 β with a molecular weight of 78 kDa. Several studies have shown that the amount of protein 4.1 α increases as the cell ages. The main function of protein 4.1 is the binding of the elastic protein network to the lipid bilayer (Chasis and Shohet 1987),(Yawata 2003).

Actin: The actin protein accounts for 5.5% of the proteins of the RBCs membranes and the actin monomer has 5 $X10^5$ copies per cell. Actin is present in membrane in the form of F-actin which is a short double helix containing 12 to 13 monomers, with a length of about 35 nm (Chasis and Shohet 1987),(Yawata 2003).

Aducin: Adducin is a protein composed of $\alpha\beta$ adducin heterodimers. The α and β adducin proteins are very similar. However, they are encoded by different genes and have a different theoretical molecular weight (calculated from the genetic sequence). The theoretical molecular weight of α-adducin is 81 kDa, whereas that of β-adducin is 80 kDa. Adducin represents a phosphoprotein that binds to Ca^{2+}/calmodulin. This phosphoprotein strengthens the binding between spectrin and actin (Yawata 2003).

Dematin: Dematin is also known as 4.2 protein consists of two chains with different molecular weights of 48 kDa and another of 52 kDa. The two chains are in the cell in the ratio of 3: 1 respectively. Studies show that Dematin is linked to a lipid membrane protein, since during an extraction of skeletal proteins this remains membrane associated (Yawata 2003).

Tropomyosin: Tropomyosin consists of two subunits of different molecular weights of 27 kDa and 29 kDa. Tropomyosin in RBCs is associated with actin and each tropomyosin is associated with eight actin monomers. Thus, actin stabilization and interactions between spectrin and actin have been seen as one of the functions of tropomyosin (Yawata 2003).

Tropomodulin: The tropomodulin protein has a theoretical molecular weight of 41 kDa and appears to have a membrane binding. This protein binds also actin and tropomyosin. The binding of tropomodulin to tropomyosin occurs in a ratio of 2: 1 (Yawata 2003). In the Figure

2.3 which is possible to observe that in the skeleton, short actin filaments links with tropomyosin and the proteins 4.1.

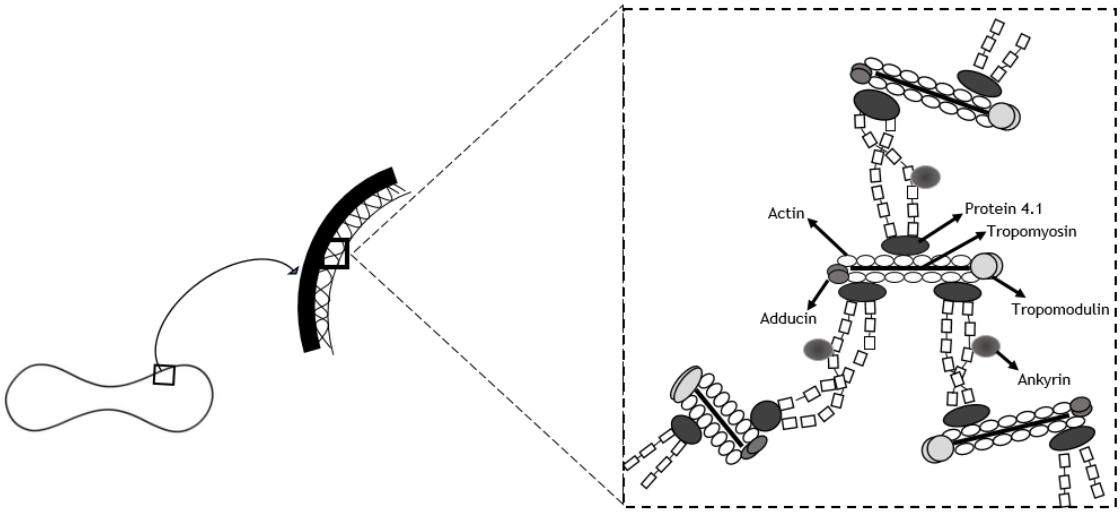

Figure 2.3 - Actin filaments links with tropomyosin and the proteins 4.1 in the skeleton

2.2.2- Membrane deformability and stability

Nowadays it is known that stability and deformability are mostly determined by the membrane skeletal proteins. When a force is applied in a RBC, membrane deformation occurs. The deformability of the membrane measures the amplitude of this deformation. On the other hand, the stability of the membrane concerns the maximum extent (deformation) that the membrane can be submitted to and still be recovering its initial shape (Chasis and Shohet 1987).

The deformability referenced here is determined by several factors such as: (i) ratio between surface and volume is large; (ii) the presence of intracellular fluid viscous due to the presence of hemoglobin; (iii) the viscoelastic properties of the RBCs (Hamasaki and Yamamoto 2000),(Dao, Lim, and Suresh 2003).

All healthy mammalian red blood cells when not subjected to external forces have disc-shaped with volume 90 m^3 and the surface area 140 m^2 , approximately (Yawata 2003). This form allows RBCs to navigate rapidly through capillaries with lower cell dimensions. The high relation between the surface and the volume that is responsible for the reversible elastic deformation of RBCs. RBCs can increase their dimensions linearly by more than twice the original dimensions, however, a 3-4% increase in surface area leads to rupture of these cells (Chasis and Shohet 1987; Evans, Waugh, and Melnik 1976).

When a force is applied to a cell it becomes deformed. The reversible deformation occurs when the cell returns to its initial form after the force removal. It is important to refer that during the reversible deformation the membrane maintains a constant surface area. Through

the Figure 2.4, it is verified that in the undeformed state the spectrin molecules are folded. After applying a shear force some spectrin molecules become more folded while others acquire a more linear form. The maximum reversible deformation occurs when the spectrin molecules reach their maximum linear extent (Chasis and Shohet 1987).

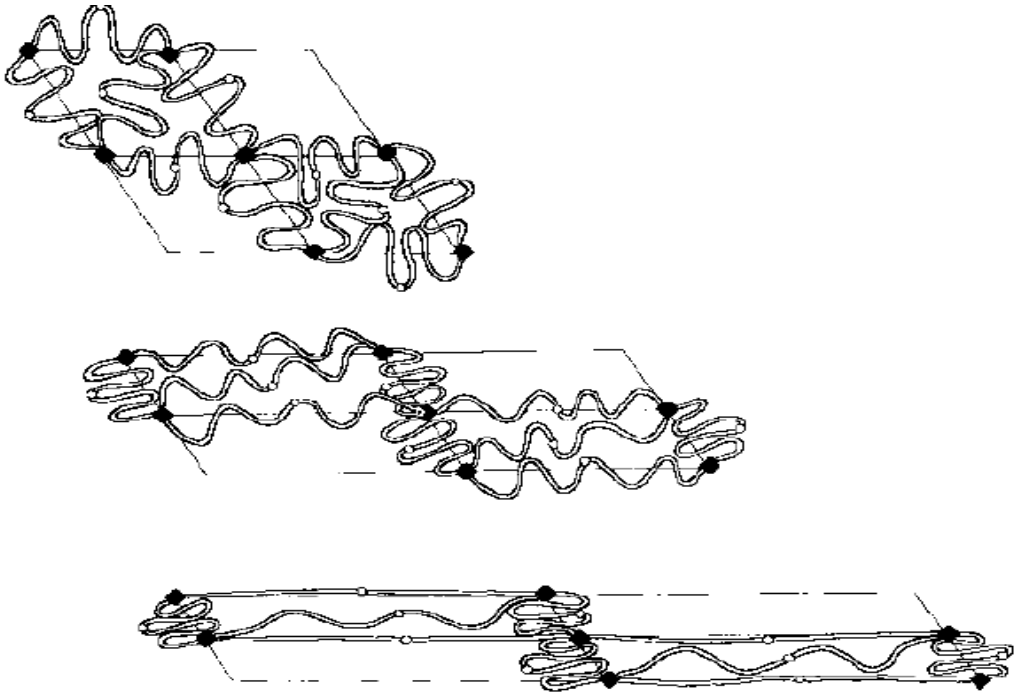

Figure 2.4 - Reversible membrane deformation (Chasis and Shohet 1987)

2.2.3- Function

In humans and other mammals, the erythrocytes are anuclear cells, with a cytoplasm consisting of 95% hemoglobin, protein which permits the transport of oxygen from the lungs to all parts of the body and is responsible for the color of blood. For the erythrocyte to ensure the efficient transport of oxygen to all cells, it must navigate rapidly through the circulatory system, that contains small capillary (where high shear stresses occur) (Buys et al. 2013).

The delivery of oxygen (O_2) to tissue is a complex process. Oxygen is indispensable to keep the most forms of life but oxygen in excess amount is dangerous for the integrity of the tissues and can induce tissues irreversible damage. RBCs enable the adequate transport of O_2 between respiratory surfaces and metabolizing tissues.

On respiratory surfaces, there is a high oxygen pressure (pO_2) which causes blood saturation in oxygen. However, in tissues the pO_2 is lower, and for this reason, when the blood passes through peripheral capillaries the release of oxygen occurs. The release of oxygen occurs because the carbon dioxide (CO_2) produced in the tissues enters the RBCs and

by carbonic anhydrase is hydrated resulting in carbonic acid (H_2CO_3), which then dissociates into H^+ and HCO_3^-. Then, through a process called "Chloride exchange" HCO_3^- is expelled into the plasma and the Cl^- enters into the RBC. This process is mediated by the Band 3 protein and allows to RBCs recognize which cells are metabolically active.

Within the RBC the H_2CO_3 is converted to HCl and thus the intracellular medium becomes more acidic. This acidification process leads to the dissociation of oxyhemoglobin (HbO_2), releasing oxygen (O_2) to the tissues. This way, in order to occur an efficient distribution of oxygen the following components are very important: the synergistic effects of hemoglobin, carbonic anhydrase, and band 3 protein.

Finally, the so-called Bohr effect occurs where the deoxyhemoglobin accepts the protons formed in the red blood cells (HbH^+) because of this the pH inside the cell is restored and the oxygen ceases to be released (Hamasaki and Yamamoto 2000). In Figure 2.5, it is possible to verify the entire oxygen distribution process described above.

The Bohr effect is essential to supply the oxygen required by the metabolizing tissues. The CO_2 produced in these tissues leads to an acidification of the RBCs releasing O_2 in any capillary. For this reason, the Bohr effect should be coupled with other humoral/neural mechanisms that regulate blood flow at the site as a function of O_2 deficiency/excess. In the latter years, it has been studied the participation of RBCs in the detection of the local oxygen conditions (by the degree of deoxidation of Hb). It was proposed that in situations of need for more oxygen (low pO_2), RBCs release the vasodilators.

Three hypotheses have arisen to explain local vasodilation: (1) reduction of nitrite to vasoactive NO by deoxy; (2) release of adenosine 5-tiffosphate (ATP); (3) release of NO from S-nitroso-Hb after deoxygenation (Ellsworth 2000)(Jensen 2004).

The low pH and low oxygen pressure (acidosis and hypoxia) existing inside the RBCs is essential for nitrite reduction. The nitrite enters in the RBCs and by action of deoxyHb is reduced to NO and the amount of NO converted is proportional to the degree of local deoxidation of the blood (Cosby et al. 2003).

Free NO is inactivated due to NO binding to deoxyHb (stable complex). When desoxyHb is oxidized, NO helps in converting hemoglobin into methemoglobin and nitrate.

Also, it was studied the hypothesis of NO binding to desoxyHb when in oxidized blood, subsequently being transferred to Cysβ93 to give S-nitroso-Hb. Then, when the oxygen pressure goes down, this compound would be released along with the NO, which would in turn act as a vasodilator. However, this hypothesis is not yet fully understood (Jensen 2004).

In several studies, it has been found that with decreasing oxygen and denaturation of hemoglobin induces the release of ATP. It has also been found that ATP induces local vasodilation resulting in increased local blood flow (Ellsworth 2000).

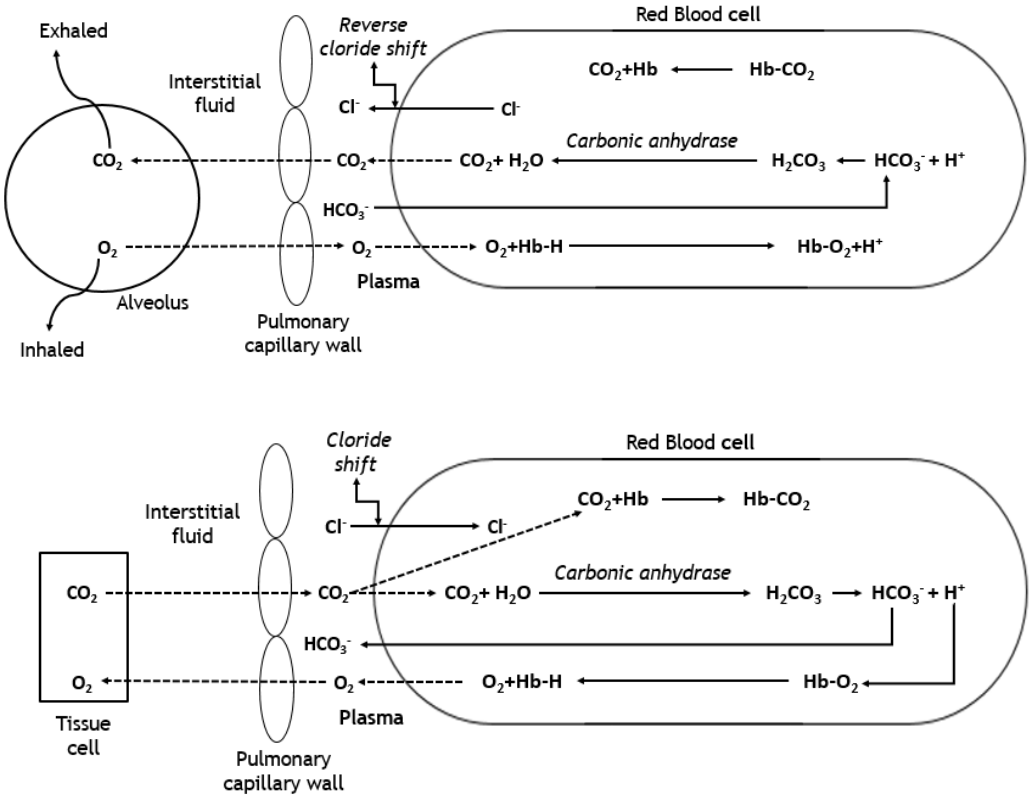

Figure 2.5 - Oxygen distribution process.

2.2.4- Mechanical properties

In recent years, it has emerged a greater interest in knowing the mechanical and electrical properties of RBCs. On the one hand, the RBCs are the major constituent in the blood and therefore are responsible for blood rheology. On the other hand, it is important to know the behavior of the membrane of RBCs to diagnose certain pathologies that lead to changes in the membrane properties of RBCs (Kozlov and Markin 1987).

The transport of oxygen and carbon dioxide is ensured by RBCs. To ensure compliance with this function, RBCs have a biconcave shape with a diameter between 7 and 8.5 μm and a thickness of approximately 2 μm. During the course of blood flow, RBCs often have to cross capillaries with 3 μm in diameter and because of this, they must undergo deformation. To explain the mechanical behavior of RBCs, it is necessary to know their properties, namely the bending elastic modulus, the area compressibility modulus and the shear elastic modulus (Tomaiuolo 2014).

The shear modulus (μ) is changed as a function of temperature or by a change in the chemical composition of the membrane. If the temperature is increased from 5 to 45°, the shear modulus ranges from 8.0×10^{-3} mN / m to 5.2×10^{-3} mN / m (Figure 2.6). The shear modulus is independent of the amount of hemoglobin although it is bound to the membrane. On the other hand, the viscosity of the membrane depends on the amount of hemoglobin in

the cell. Studies also demonstrate that the viscosity of the membrane varies with temperature (Membrane 1987).

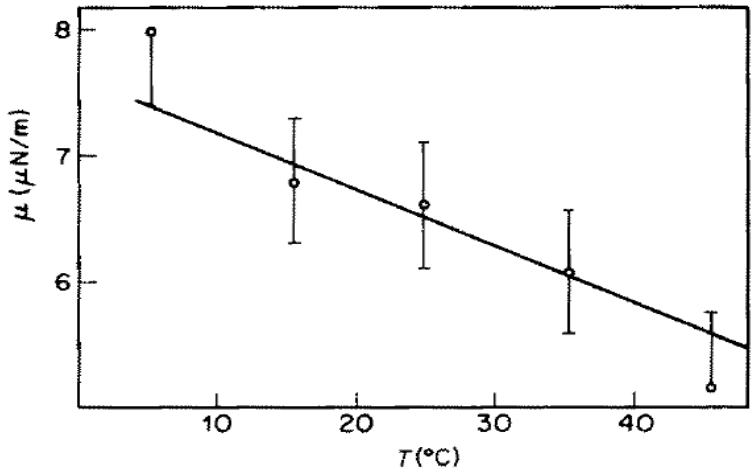

Figure 2.6 - Representation of the theoretical and experimental behavior of the shear modulus. The straight line represents the theoretical behavior of the shear modulus (Kozlov and Markin 1987).

Different mechanical and geometric properties of healthy RBCs are present in Table 2.2.

Table 2.2 - Mechanical and geometric properties of healthy RBCs (Tomaiuolo 2014).

Property	Healthy RBC
Volume (μm^3)	89.4±17.6
Surface area (μm^2)	113.8±27.6
Cytoplasmatic viscosity (mPa/s)	6.07±3.8
Surface viscosity (μN s/m)	0.7±0.2
Shear elastic modulus (μN/m)	5.5±3.3
Bending elastic modulus ($\times 10^{-9}$ Nm)	1.15±0.9
Relaxation time constant (s)	0.17±0.08
Area compressibility modulus (mN/m)	399±110
Young's modulus (KPa)	26±7

2.3 - Pathologies

Alterations in the molecular structure of the cytoskeleton and in the membrane of the RBCs are associated with several hereditary and infectious diseases, such as spherocytosis, elliptocytosis, sickle cell anemia and malaria. All these diseases have common characteristics: alteration of the cell morphology, loss of surface area and a reduction in the

capacity of deformation so they have greater difficulty in crossing capillaries (Suresh 2006). The properties of RBCs are maintained by two forms of interactions: vertical and horizontal. In the vertical the lipid bilayer relates to the spectrin network through the articulation between the components ankyrin, protein 4.2, band 3 and spectrin. On the other hand, the horizontal interactions occur between the constituents of the skeleton, through the articulation between the components α and β spectrins, actin and protein 4.1.

Malaria

In one year, malaria accounts for 2-3 million deaths, covering 8% of the population (Suresh 2006). Malaria is an infectious disease transmitted by female Anopheles mosquitoes that carry parasites of the genus Plasmodium. The most common Plasmodium parasites are Plasmodium falciparum and Plasmodium vivax. The parasite Plasmodium falciparum is responsible for the highest number of deaths. When a female Anophele mosquito (carrier of parasite P. falciparum) bites a human, this injects millions of P. falciparum sporozoites. Through the blood circulation the sporozoites are taken to the liver where they reproduce/multiply for 8 days producing thousands of merozoites. After this time, the liver releases the merozoites into the bloodstream. These infect the RBCs causing changes in their mechanical and rheological properties, as well as their morphology. These changes may cause lysis of the RBCs causing the release of newly nucleated merozoites, available to infect other RBCs (Suresh 2006).

The infection consists of three stages: ring, trophozoite and schizont (Figure 2.7). Approximately 30 minutes after penetration into RBCs, the ring stage begins. At this stage, the central region of the parasites becomes thin and its periphery (containing the nucleus and other organelles) becomes thicker. The shape of a ring with a diameter of 2-3 mm is thus developed. This stage lasts approximately 24 hours. At this stage, characteristics such as the shape and size of RBCs remain almost unchanged.

The trophozoite stage occurs between 24-36 hours after the invasion. At this stage, the parasite has its most active metabolism and its size increases by about 4 mm. There is a change of the shape and size of the surface RBC trophozoite acquiring lumps and becomes rounder. The RBC volume increases by approximately 17% compared to a healthy RBC.

The schizont stage, occurs 36 to 48 hours after the parasite invasion. At this stage RBC schizont acquires a quasi-spherical shape and its surface area relative to a soluble RBC decreases approximately 18%. During this time, the parasite undergoes DNA replications producing between 16 and 20 daughter parasites capable of invading other RBCs. After infection, the RBCs become less deformable and there is a decrease in their ability to recover the original shape. RBCs also become more easily attached to blood vessels may lead to

obstruction of small capillaries (Suresh 2006),(Hanssen, Mcmillan, and Tilley 2010)(Ye et al. 2013).

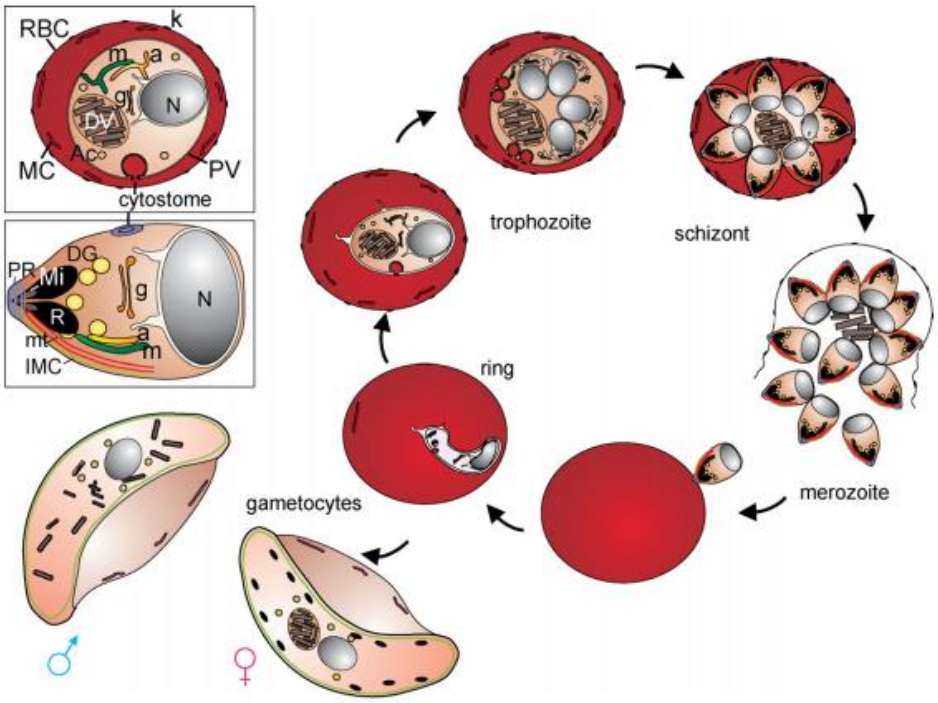

Figure 2.7 - Malaria stages of the infection (Biology et al. 2011).

Over the last few years, many studies have attempted to quantify the mechanical effect of parasites on RBCs. Researchers (Hosseini and Feng 2012) have quantified this mechanical effect using a computational model. They concluded that at the ring stage the effect of the parasite on the deformation of RBC is almost null because the volume of the parasite is still very small. However, in the trophozoite and schizont stages there is a high reduction of the deformation capacity of the RBCs since the membrane of the red blood cells is pressed against the parasite when stretched.

Fedosov and co-workers (Fedosov et al. 2011) studied the influence of temperature on the shear modulus on healthy RBCs and on RBCs invaded by the parasite Plasmodium falciparum. They concluded that there is a high dependence between temperature and rheological properties. For example, the increase in temperature from 37ºC (normal physiological state) to 41ºC (feverish state) leads to a sharp and gradual hardening of RBCs parasitized throughout the three stages as it is possible to be seen in the Table 2.3.

Table 2.3 - Influence of temperature on several parameters in healthy cells and cells infected by the parasite (Fedosov et al. 2011), (Wu et al. 2013).

		T	Healthy	Ring	Early trophozoite	Late trophozoite	Schizont
Property	Shear modulus	23º C	6.3	14.5	-	29 *	60 & 40
		37º C	5.8	14.5	-	35 *	71.8
		41º C	4.9	20.4	-	56.6 *	95
	Surface area (μm^2)	-	132	132	132	132	97
	Volume (μm^3)	-	92	92	105	116	85
	Radius of RBC - $\alpha(\mu m)$	-	2.80	2.80	2.92	3.02	2.72
	$S_e = S/(4\pi\alpha^2)$	-	1.34	1.34	1.23	1.15	1.04
	Dimensions of the parasite – (μm)	-	(none)	Radius=1, thickness=0.5	Radius=1.4	Radius=1.7	Radius=2.4, thickness=3

Hereditary spherocytosis (HS)

HS is the most common form of hemolytic anemia of autosomal dominant inheritance and is most common in northern Europe, with a prevalence of 1 in 2000 individuals (Tse and Lux 1999). The clinical manifestations of HS are highly variable from very mild to severe. The shape of healthy RBCs may be altered due to vertical or lateral movements of the cytoskeleton. The origin of HS is in defects of the proteins present in the vertical interaction between the lipid bilayer and the membrane skeleton. The rupture of the vertical bonds between the phospholipid bilayer and the membrane skeleton leads to a reduction of the surface area in the HS and hence, the smaller and more spherical RBCs. Between 30-45% of patients with HS manifest mutations in ankirin and spectrin, 30% in spectrin alone and approximately 20% in Band 3. RBCs affected by HS have a more fragile membrane, a smaller diameter and a more spherical shape when compared with healthy RBCs. These characteristics lead to RBCs with HS having a reduced life because during the bloodstream they are captured and destroyed in the spleen. Continued destruction of these RBCs may lead

to the production of new RBCs occurring at a lower rate than the destruction of RBCs with HS. Products resulting from hemoglobin degradation may lead to bilirubin formation. When the amount of bilirubin exceeds the capacity of the liver, jaundice develops. The products of degradation of the cells when in excess can penetrate in the bile tree forming of cyclic calculations (Suresh 2006),(Tse and Lux 1999),(Trompeter and King 2015).

The main clinical features of HS are anemia, reticulocytosis, splenomegaly, jaundice and gallstones. After the neonatal period, there are three possible classifications for HS: mild, moderate and severe. In mild HS there is compensated hemolysis and there is no anemia, in moderate and severe HS the hemolysis is incomplete and exist anemia (Iolascon, Avvisati, and Piscopo 2010). The diagnosis and classification of HS (Table 2.4) are performed based on clinical data and laboratory parameters: haematological parameters, percentage of reticulocytes, peripheral blood smear, osmotic fragility and bilirubin assay.

Table 2.4 - Classification of HS are performed based on clinical data and laboratory parameters (Da et al. 2013).

			Minor HS	**Moderate HS**	**Moderate to severe HS**	**Severe HS**
Laboratory parameters	Hemoglobin (g/l)		Normal	>80	60-80	<60
	Bilirubin (µmol/l)		17.1-34.2	>34.2	>34.2-51.3	>51.3
	Reticulocytes (%)		< 6%	6-10%	>10%	>10%
	Red blood smear		Few spherocytes	Spherocytes	Spherocytes	Microspherocytes and poikilocytosis
	Osmotic fragility	Before incubation	Normal or slight increased	Increased	Increased	Increased
		After incubation at 37 ° C	Increased	Increased	Increased	Increased

Diabetes

Type 2 diabetes is a metabolic disorder characterized by high levels of glucose (hyperglycemia) that accumulate in the blood. High glucose levels result from insulin resistance or insufficient insulin production. Diabetes represents a risk factor for cardiovascular disease. In several studies, diabetes is associated with an abnormal form of RBCs, increased blood plasma viscosity, and decreased deformability. In one of these studies,

atomic force microscopy and scanning electron microscopy were used to study the roughness and membrane shape of healthy and diabetic RBCs. It was concluded that the RBCs of type 2 diabetic patients have a smooth membrane, are more elongated and fold around fibrin fibers that spontaneously form (Figure 2.8) (Buys et al. 2013),(Tomaiuolo 2014).

Figure 2.8 - The RBCs of type 2 diabetic patients **(Buys et al. 2013).**

Alzheimer's

Alzheimer's is a progressive neurodegenerative disease that affects about 40 million people worldwide (Szab 2015). There is not yet an early diagnosis method or a cure method. Several studies of Alzheimer's disease report abnormalities in non-neuronal cells including in RBCs. Changes in existing proteins in the cytoskeleton or membrane cause the morphology and shape of RBCs in Alzheimer's individuals to be altered. This implies the modification of the elasticity and or stability of the RBCs (Mohanty et al. 2010). Alzheimer's patients appear to demonstrate early aging of RBC membranes. The aging mentioned here is similar to what occurs in brain tissue, thus opening new avenues for monitoring the progression of the disease (Sabolovic et al. 1997).

Sickle cell anemia

Sickle cell anemia has a heterogeneous clinical phenotype but in several cases causes painful crises as a result of occlusion of small vessels. There is a change in form passing the RBCs to take the form of a sickle. The origin of this disease is in a mutation in the sequence encoding hemoglobin. The hemoglobin leaves the globular form and several molecules of hemoglobin associate to create long fibers (Figure 2.9). There is an increase in the stiffness (greater Young's modulus) of RBCs leading to vaso-occlusion of capillaries and deoxygenation of tissues (Suresh 2006),(Li et al. 2017).

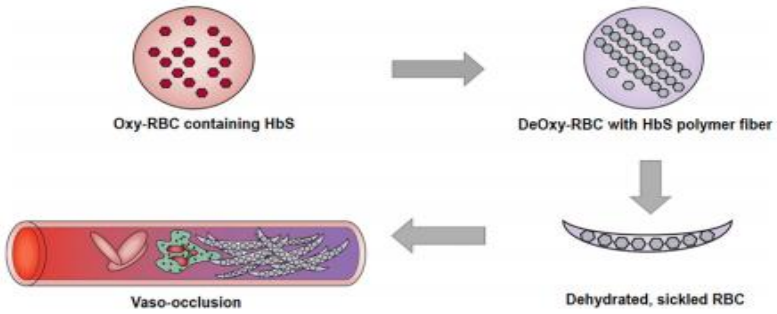

Figure 2.9 - Association of several molecules of hemoglobin to form long fibers (Li et al. 2017).

Ovalocytosis (SAO)

Hereditary ovalocytosis is also known as stomatocyte elliptocytosis. It is a disease with the highest incidence in Southeast Asia. At its origin is a mutation in the protein band 3, nine of the amino acids that make up this protein undergo a deletion. The mutation gives carriers resistance to different parasites that cause malaria, as well as high resistance to cerebral malaria.

RBCs with SAO have a higher stiffness, decrease the transport of anions and have a more oval shape (Paquette et al. 2015; Wong 2004).

Cancer

In many living organisms and in particular in humans, some internal factors lead to a genetic mutation. This mutation leads to new biochemical reactions that are responsible for changing the mechanical properties and internal structure of many cells of the organism. Altering the mechanical properties of cells, particularly the modulus of elasticity, leads to a rapid progression of the disease.

A carcinogenic RBC has a lower modulus of elasticity than healthy cells and is therefore more deformable. During a metastasis process the cancer cells with a lower Young's modulus have the ability to transpose small pores present in the endothelium and basement membrane progressing very rapidly (Hosseini and Feng 2009).

Chapter 3

Numerical Methods

There are innumerable possible phenomena to be described using strong form differential equations. The exact solution using the strong form differential equations is only obtainable in problems with simple and well-behaved geometries. Thus, in order to solve complex problems, it is necessary to resort to weak formulations. In this case, it is not possible to obtain analytical exact solution. It is only possible to obtain approximate solutions (Suli 2012).

Finite element method (FEM): The first steps for the FEM were given by Rayleigh in 1870, Ritz in 1909 and Galerkin in 1915. These investigators solved differential equations using interpolation functions and thus the first problems to be solved using approximate methods appeared. The term FEM, as we know it today, was introduced by Clough in 1960 (Campilho 2012).

Currently the FEM starts from the domain of the problem and divides it into smaller parts that can have different shapes and are named by elements. All these elements form a mesh (Reddy 2005).

To obtain an approximate solution, a considerable number of nodes must be used. The more refined the mesh, the more accurate the solution. However, an increase in the computational cost is observed (Campilho 2012).

The FEM is used to solve numerous engineering problems. However, in some problems this numerical method has some limitations. For example, in problems where there are large deformations the mesh takes a very distorted form, leading to less accurate results (Belytschko et al. 1996).

Meshless methods (MMs): The first mature MMs appeared in 1980 (Belytschko et al. 1996). In the MMs an approximate solution is obtained from a set of arbitrarily distributed nodes (Pierre et al. 2008). Contrary to what is verified in the FEM in the MMs, overlapping domains of influence may occur. In complex problems MMs are preferable to FEM since they obtain more precise solutions (Belinha 2014).

This chapter includes a brief introduction of the finite element method, and discusses in detail meshless methods, more precisely RPIM and NNRPIM.

3.1 - FEM

FEM arose from the difficulty of man to estimate the solution of complex structural problems. Separating the systems in basic components (elements), simplify the solution of the global system.

There are currently many possible application areas for the FEM, which include: structural engineering; civil, mechanics; naval; aeronautics; aerospace; Metallurgy; Mining; Oil exploration; Armed forces; Automobile industry, among others.

A more recent area of application of FEM is in prevention medicine, where optical models are used to construct a model of the human body that is later used to simulate the patient's response to alternative treatments. It is also possible to use this method to plan surgical procedures to optimize for example the number of points to be used in a given intervention. Another possible application of FEM is the prosthesis structural/function optimization. Thus, each prosthesis will be suitable for a particular patient with a specific weight and bone structure and also specific musculature (Campilho 2012).

This method "cuts/decomposes" an element with a complex geometry into several finite-dimensional elements. These elements may have different shapes, such as quadrilaterals or triangles in 2 dimensions or tetrahedrons or hexahedrons in 3 dimensions. The mentioned elements are interconnected by common nodes (Figure 3.1), that allow these elements to remain together (discretization).

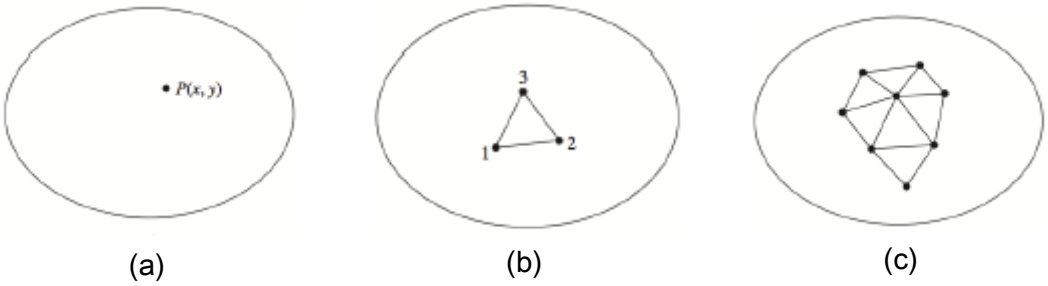

Figure 3.1 - Process of discretization

Analyzing a finite triangular element (Figure 3.1(b)) containing a finite-size subdomain of the domain in question, its vertices are designated by nodes and each node is a point in the domain in which the field variable(s) will be calculated using FEM.

It can be said that the FEM applied to a given element determines the values of the field variables for the nodes and uses them to approximate the variables in the non-nodal points by

means of interpolation functions. The field variable for the case of the triangle described above would be given by:

$$\phi(x,y) = N_1(x,y)\phi_1 + N_2(x,y)\phi_2 + N_3(x,y)\phi_3 \quad \textbf{(3.1)}$$

Where ϕ_1, ϕ_2 and ϕ_3 represent the values of the field variable in the respective nodes and N_1 N_2 and N_3 represent the interpolation functions.

Another important concept to approach is that of degrees of freedom if the domain is a two-dimensional body. The field variables will be displacements according to the orthogonal directions u_i and v_i (i = 1,2, ..., total number of nodes). For example, for the case of the triangle, the number of degrees of freedom would be 6 because it has three nodes and two nodal variables (since there are two degrees of freedom per node).

I. Pre-processing

The accuracy of the method depends on the number of nodes and elements as well as the size and type of elements present in the mesh. It is also known that as the size of finite elements tends to zero, that is, the number of nodes tends to infinity, the solution obtained converges to the exact solution of the problem.

Thus, in the pre-processing step (Table 3.1) it should contain the following steps:

Table 3.1- Pre-processing

Pre-processing	- Definition of the geometric domain of the problem
	- Definition of the type(s) of elements to be used;
	- Definition of the material properties of the elements;
	- Definition of the geometric properties of the elements (length, area);
	- Definition of the connectivity between the elements; (mesh of the model);
	- Definition of the constraints of the field variables (boundary conditions);
	- Definition of loads (forces, etc.).

I. Obtaining the solution

For static structural problems, the finite element method results in a system of equations that can be expressed in the form of (Hooke's Law):

$$\boldsymbol{f} = \boldsymbol{K}\boldsymbol{u} \tag{3.2}$$

where $\boldsymbol{f}$ represents the column of force vectors, $\boldsymbol{u}$ represents the column of the displacement vectors and $\boldsymbol{K}$ represents a square matrix.
The square matrix size $\boldsymbol{K}$ is given by the product of the number of nodes by the number of degrees of freedom per node.

III. Pos-processing

In this FEM stage, different parameters can be analyzed, such as the deformation of RBCs or the temperatures and strain felt through a color scale, among other parameters. A more complete analysis of this method can be found in (Campilho 2012).

3.2 - Meshless Methods

3.2.1 - Meshless Generic Procedure

The MMs have revolutionized the scientific community. These methods have two major advantages. The first is that they permit the study of large distortions, such as those observed for example in muscles. The second relates to the possibility of simulating flows such as blood flow. The MMs procedure, such as other numerical methods, respect an order. Initially the geometry/contour of the object to be simulated (a posteriori) is studied, establishing the discretization of the domain and the contour resulting in a certain number of nodes that can be arbitrarily distributed in a regular or irregular way. The nodes do not have to obey a mesh since for the construction of the field functions no information about the relation established between the different nodes is needed, being only necessary to know the spatial position of each node. The number of nodes employed and their distribution through space will influence the results obtained. A higher number of nodes leads to better results, however, the higher the number of nodes used, the greater the computational cost. It should be noted that for achieving the best results, the node density must be higher in places where greater stress is predicted. The next step of the MMs is the construction of a background integration mesh. Thus, it is possible to apply the interpolation functions that have a certain domain of influence which determines that the interpolation function is not null. For the different MMs the way in which the influence domain is determined undergoes a variation.

MMs are divided into two formulations, the strong formulation and the weak formulation. In the strong formulation, the solution is obtained directly by the application of the partial

differential equations. In the weak formulation, an interpolation function multiplied by a test function replaces the exact solution equation giving a residue. The minimization of this residue is achieved by applying the variational principle. An integration method is applied to integrate the residue. This method can use a background integration mesh that includes the entire domain of the problem or else use the nodal mesh itself where the nodes are assumed to be integration points. The integration weight of each node is obtained using diagrams of Voronoï. The latter method leads to a lower precision, implying the use of a stabilization method which leads to a higher computational load (Belinha 2014).

Briefly, MMs require the application of three phases. The functions of interpolation, formulation and integration. Next, the differences for RPIM and NNRPIM with regard to nodal connectivity and numerical integration will be analyzed.

3.2.2 – RPIM

3.2.2.1 - Nodal connectivity

After the distribution of the nodes along the domain and the contour it is necessary to impose nodal connectivity. Connectivity is only determined at this stage because there is no nodal interdependence as in the FEM.

In MMs in RPIM the weak formulation is applied and the domains of influence undergo an overlap to obtain the connectivity. In other words, concentric areas and volumes are defined around the points of interest (in the majority of meshless methods, the interest points are the integration points) and the nodes belonging to the interior of these areas/volumes are classified as belonging to the influence domain. This domain can vary in shape and size (Figure 3.2) by affecting the final solution of the method. It is important that the number of nodes belonging to different domains of influence is similar. In each domain of influence there must be between 9 and 16 nodes. In MMs, regular forms are often analyzed where it is sometimes possible to find groups of clusters of nodes. It is therefore important that domains also assume irregular forms (Belinha 2014).

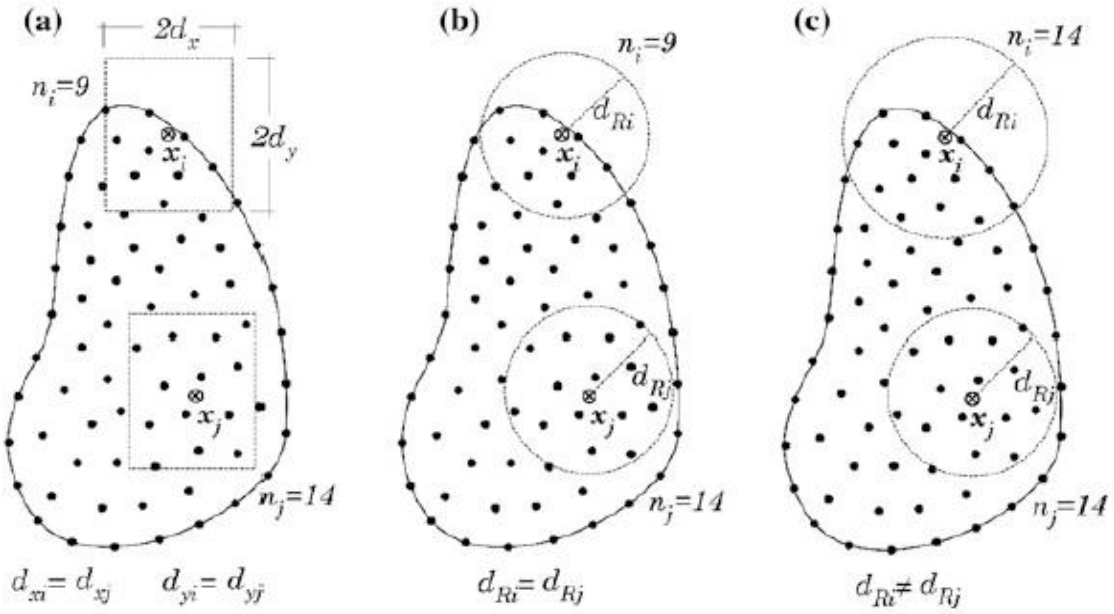

Figure 3.2 - Different types and shape of influence-domains: (a) rectangular shaped, (b) circular shaped and (c) flexible circular shaped.

3.2.2.2 - Integration points

After determining the nodal connectivity, it is necessary to determine the integration points. In RPIM, the Gauss-Legendre quadrature rule is used. The first step is to divide the domain by creating a background mesh. The mesh may contain triangular or quadrangular cells that join the different nodes of the domain (Figure 3.3 (a) and (b)). On the other hand, it is possible to create a regular mesh with a dimension larger than the domain of the problem, and it should later be eliminated from the integration points located outside the domain (Figure 3.3 (c)) (Belinha 2014).

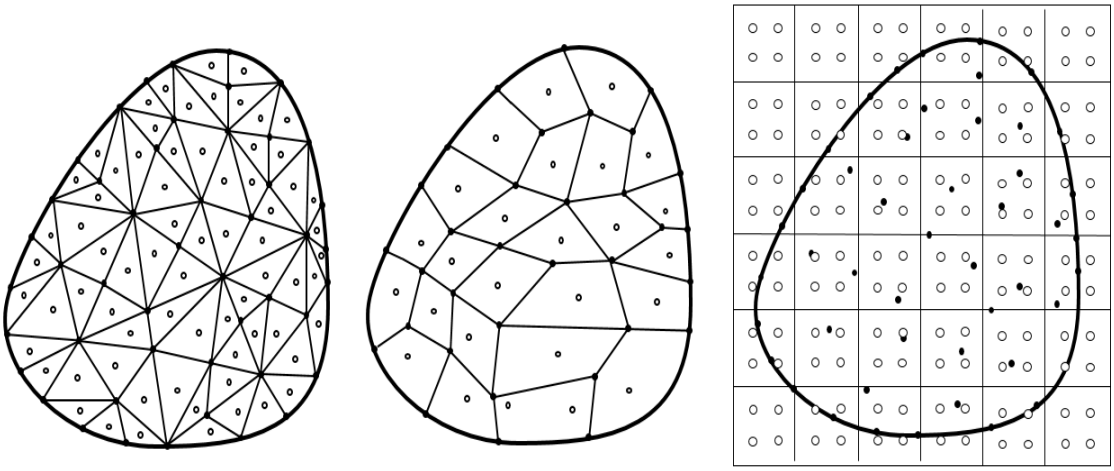

Figure 3.3 - (a) Background mesh with triangular cells (b) Background mesh with quadrangular cells (c) Background mesh with dimensions greater than the domain.

As can be seen in Figure 3.4, the integration points are distributed within each cell according to the Gauss-Legendre rule. The location and weights of each integration point vary depending on the shape chosen for the cells (triangular or quadrangular).

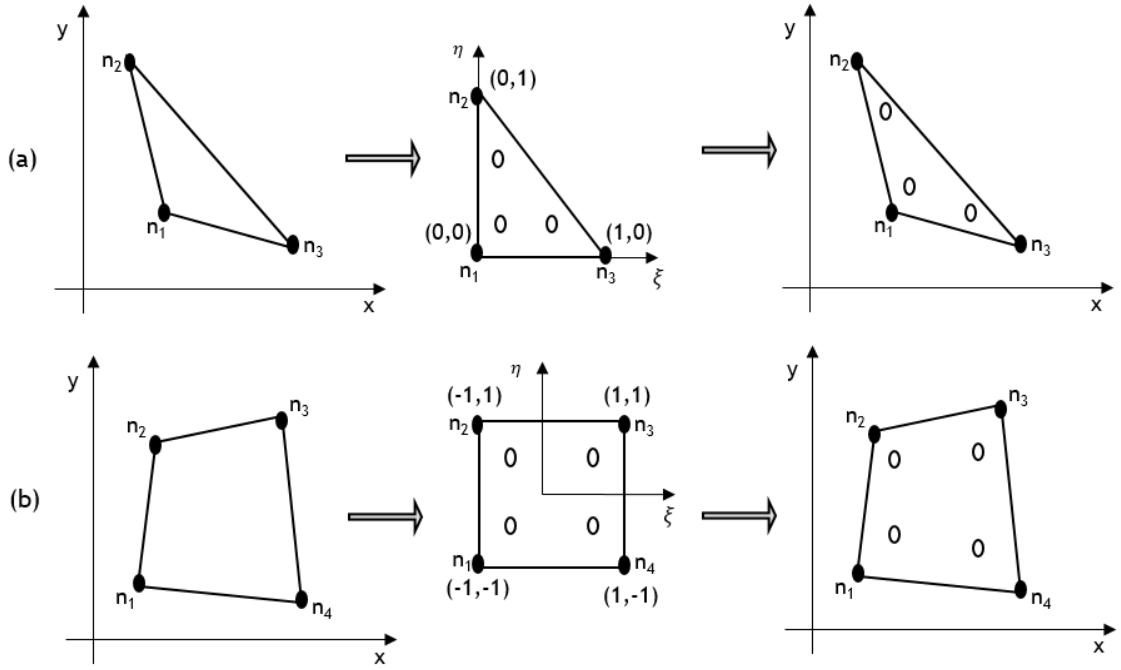

Figure 3.4 - Distribution of the integration points by cells with different shapes.
In

Table 3.2 are present the different distributions of the integration points and the respective integration weight assigned to triangular and quadrangular cells respectively (Wriggers 2006).

Table 3.2 - Different distributions of the integration points and the respective integration weight assigned to triangular and quadrangular cells respectively (Wriggers 2006).

Point	ξ_p	η_p	W_p	Position of points
a	$\frac{1}{3}$	$\frac{1}{3}$	$\frac{1}{2}$	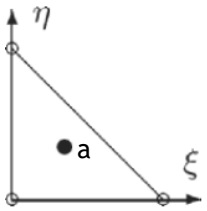
a	$\frac{1}{2}$	$\frac{1}{2}$	$\frac{1}{6}$	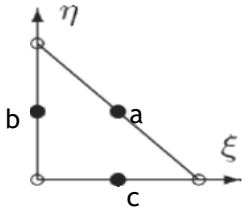
b	0	$\frac{1}{2}$	$\frac{1}{6}$	
c	$\frac{1}{2}$	0	$\frac{1}{6}$	
a	$\frac{1}{6}$	$\frac{1}{6}$	$\frac{1}{6}$	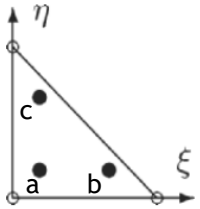
b	$\frac{2}{3}$	$\frac{1}{6}$	$\frac{1}{6}$	
c	$\frac{1}{6}$	$\frac{2}{3}$	$\frac{1}{6}$	
a	$\frac{1}{3}$	$\frac{1}{3}$	$-\frac{27}{96}$	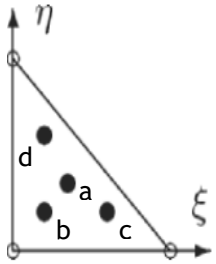
b	$\frac{1}{5}$	$\frac{1}{5}$	$\frac{25}{96}$	
c	$\frac{3}{5}$	$\frac{1}{5}$	$\frac{25}{96}$	
d	$\frac{1}{5}$	$\frac{3}{5}$	$\frac{25}{96}$	
a	0	0	4	
a	$-\frac{1}{\sqrt{3}}$	$-\frac{1}{\sqrt{3}}$	1	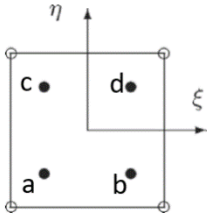
b	$\frac{1}{\sqrt{3}}$	$-\frac{1}{\sqrt{3}}$	1	
c	$-\frac{1}{\sqrt{3}}$	$\frac{1}{\sqrt{3}}$	1	

d	$\frac{1}{\sqrt{3}}$	$\frac{1}{\sqrt{3}}$	1
a	$-\sqrt{\frac{3}{5}}$	$-\sqrt{\frac{3}{5}}$	$\frac{25}{81}$
b	0	$-\sqrt{\frac{3}{5}}$	$\frac{40}{81}$
c	$\sqrt{\frac{3}{5}}$	$-\sqrt{\frac{3}{5}}$	$\frac{25}{81}$
d	$-\sqrt{\frac{3}{5}}$	0	$\frac{40}{81}$
e	0	0	$\frac{64}{81}$
f	$\sqrt{\frac{3}{5}}$	0	$\frac{40}{81}$
g	$-\sqrt{\frac{3}{5}}$	$+\sqrt{\frac{3}{5}}$	$\frac{25}{81}$
h	0	$\sqrt{\frac{3}{5}}$	$\frac{40}{81}$
i	$\sqrt{\frac{3}{5}}$	$\sqrt{\frac{3}{5}}$	$\frac{25}{81}$

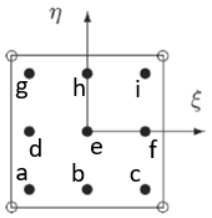

Distributed integration points by the cells the Cartesian coordinates (x_i, y_i) of the Gaussian points are given by:

$$x = \sum_{i=1}^{m} N_i(\xi, \eta).x_i \tag{3.3}$$

$$y = \sum_{i=1}^{m} N_i(\xi, \eta).y_i \tag{3.4}$$

Where m represents the number of nodes within each cell and N_i represents the isoparametric interpolation functions that differ for the triangular and quadrangular elements.

For triangular elements:

$$N_1(\xi,\eta) = 1-\xi-\eta$$
$$N_2(\xi,\eta) = \eta \tag{3.5}$$
$$N_3(\xi,\eta) = \xi$$

For quadrangular elements:

$$N_1(\xi,\eta) = \frac{1}{4}(1-\xi)(1-\eta)$$
$$N_2(\xi,\eta) = \frac{1}{4}(1-\xi)(1+\eta) \tag{3.6}$$
$$N_3(\xi,\eta) = \frac{1}{4}(1+\xi)(1+\eta)$$
$$N_4(\xi,\eta) = \frac{1}{4}(1+\xi)(1-\eta)$$

The Jacobian matrix given by,

$$\boldsymbol{J} = \begin{pmatrix} \frac{\partial x}{\partial \xi} & \frac{\partial x}{\partial \eta} \\ \frac{\partial y}{\partial \xi} & \frac{\partial y}{\partial \eta} \end{pmatrix} \tag{3.7}$$

Multiplying the isoparametric weight by the determinant of the Jacobian matrix it is possible to obtain the integration weight for a certain point of integration. Finally, the integration of the differential equation is calculated as follows,

$$I = \int_{-1}^{1}\int_{-1}^{1} f(\boldsymbol{x}_i).\det(\boldsymbol{J})\, d\xi d\eta = \int_{-1}^{1}\int_{-1}^{1} f(\boldsymbol{x}_i) dxdy$$
$$= \sum_{i=1}^{m}\sum_{j=1}^{n} \omega_i \omega_j f(\boldsymbol{x}_i) \tag{3.8}$$

being that for a given point of integration x_i the variables ω_i and ω_j represent the weight in the two possible directions.

3.2.3 – NNRPIM

The NNRPIM is described with detail in the literature (Belinha 2014). In this section, only the NNRPIM basic fundamentals are presented.

3.2.3.1 - Nodal connectivity

In NNRPIM, unlike RPIM, nodal connectivity is not obtained by the overlapping of influence domains but by influence cells. To obtain the cells of influence, the Voronoï diagrams and the Delaunay triangulation method can be applied. After the discretization for each node n_I is determined a Voronoï cell V_I defined by a polygon with P_{Ii}vertices. Each Voronoï cell in the case of an irregular mesh can be further divided into n smaller quadrilaterals S_{Ii}. The midpoint between node n_I and node n_i is designated M_{Ii}. In the case of a regular mesh the

midpoints M_{Ii} coincide with the midpoints of the edges giving rise to triangles instead of quadrilaterals (Figure 3.5).

This method is advantageous because for the elaboration of the background integration scheme it is only necessary to know the position in the space of the nodes belonging to the domain (Belinha 2014).

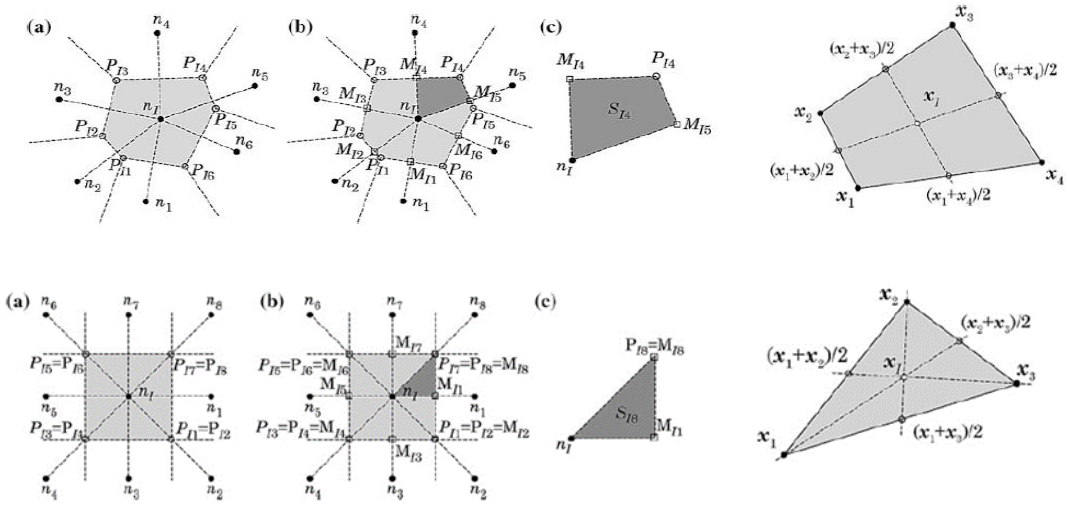

Figure 3.5 - (a) Irregular Voronoï cells (b) regular Voronoï cells.

Influence cells can be divided into two types of first and second degree. The first degree contain the first natural neighbors only. The second-degree on the other hand also contain the natural neighbors of the first natural neighbors, as it is possible to verify in the Figure 3.6.

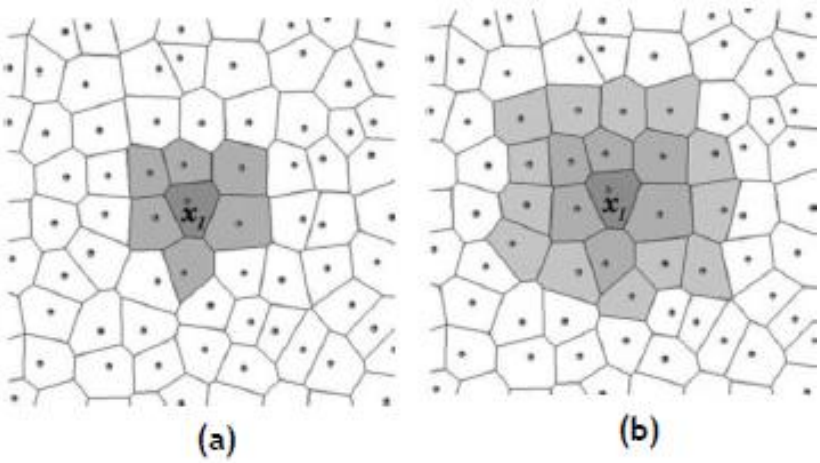

Figure 3.6 - (a) First degree influence- cell (b) Second degree influence-cell.

3.2.3.2 - Integration points

After the determination of the nodal connectivity, it is necessary to determine the integration points. After the construction of the Voronoï diagram the Delaunay rule is applied, obtaining smaller areas inside the Voronoï cells. In the two-dimensional case and for the node $\boldsymbol{x}_i$ the size (A_{VI}) of a Voronoï cell (Belinha 2014),

$$A_{VI} = \sum_{i=1}^{n} A_{S_{Ii}}, \quad \forall\, A_{S_{Ii}} \geq 0 \tag{3.9}$$

is the sum of the size of all S_{Ii} sub-cells. For the two-dimensional and three-dimensional case A represents an area and a volume respectively. It is assumed that in NNRPIM the weight assigned to any integration point is calculated by the sum of the areas S_{Ii}. The sub-cells alternate essentially between the form of squares and triangles. From these forms, it is possible to apply different methods of integration methods.

3.2.4 - Shape functions

In RPIM and NNRPIM the applied form function is the same and respects the property of delta Kronecker, that is, $\varphi_i(\boldsymbol{x}_j) = \delta_{ij}$ with $\delta_{ij} = 1$ for $i = j$ and $\delta_{ij} = 0$ for $i \neq j$.

The function of form $u(\boldsymbol{x}_\mathrm{I})$ consists of a radial basis function ($R_i(\boldsymbol{x}_\mathrm{I})$) combined with a polynomial function ($p_j(\boldsymbol{x}_\mathrm{I})$) (Belinha 2014; Dai and Liu 2006),

$$\begin{aligned} u(\boldsymbol{x}_\mathrm{I}) &= \sum_{i=1}^{n} R_i(\boldsymbol{x}_\mathrm{I}) a_i(\boldsymbol{x}_\mathrm{I}) + \sum_{j=1}^{m} p_j(\boldsymbol{x}_\mathrm{I}) b_j(\boldsymbol{x}_\mathrm{I}) = \boldsymbol{R}^T(\boldsymbol{x}_\mathrm{I})\boldsymbol{a} + \boldsymbol{p}^T(\boldsymbol{x}_\mathrm{I})\boldsymbol{b} \\ &= \{\boldsymbol{R}^T(\boldsymbol{x}_\mathrm{I}), \boldsymbol{p}^T(\boldsymbol{x}_\mathrm{I})\} \begin{Bmatrix} \boldsymbol{a} \\ \boldsymbol{b} \end{Bmatrix} \end{aligned} \tag{3.10}$$

For a discrete Ω domain in N points, $\boldsymbol{x}_\mathrm{I}$ represents a point of interest and n the number of nodes in the domain of influence of that same point. The coefficients $a_i(\boldsymbol{x}_\mathrm{I})$ and $b_j(\boldsymbol{x}_\mathrm{I})$ are not constants, assuming different values according to the point of interest $(\boldsymbol{x}_\mathrm{I})$. The values assigned to n and m vary according to the requirements of the problem. In the one-dimensional case $m = 3$ and $\boldsymbol{p}^T = \{1, x, x^2\}$, in two-dimensional problems $m = 6$ e $\boldsymbol{p}^T = \{1, x, y, x^2, xy, y^2\}$ in three-dimensional cases $m = 10$ and $\boldsymbol{p}^T = \{1, x, y, x^2, xy, y^2, yz, z^2, zx\}$. The polynomial function must obey the condition $\sum_{i=1}^{n} p_j(\boldsymbol{x}_\mathrm{I}) a_i = 0$, with $j = 1,2,\ldots,m$. Finally, the radial base function ($R_i(\boldsymbol{x}_\mathrm{I})$) can take many forms. Generally, for two-dimensional problems the most used form is the following,

$$R_{ij} = ({r_{ij}}^2 + c^2)^p \tag{3.11}$$

Where c and p are parameters such that their modification changes the accuracy of the radial basis functions according to the literature these parameters should assume values of approximately 0 and 1 (Dinis, Jorge, and Belinha 2009) respectively. The parameter r_{ij} represents the Euclidean norm between the integration point (x_I) and the other point of the domain to be considered (x_i) and is therefore determined by:

$$r_{ij} = \sqrt{(x_I - x_i)^2} \tag{3.12}$$

Proceeding by substituting in the equation (3.10),

$$\begin{bmatrix} \boldsymbol{R} & \boldsymbol{p} \\ \boldsymbol{p^T} & \boldsymbol{0} \end{bmatrix} \begin{Bmatrix} \boldsymbol{a} \\ \boldsymbol{b} \end{Bmatrix} = \begin{Bmatrix} \boldsymbol{u_s} \\ \boldsymbol{0} \end{Bmatrix} \Rightarrow \begin{Bmatrix} \boldsymbol{a} \\ \boldsymbol{b} \end{Bmatrix} = \begin{bmatrix} \boldsymbol{R} & \boldsymbol{p} \\ \boldsymbol{p^T} & \boldsymbol{0} \end{bmatrix}^{-1} \begin{Bmatrix} \boldsymbol{u_s} \\ \boldsymbol{0} \end{Bmatrix} \Rightarrow \begin{Bmatrix} \boldsymbol{a} \\ \boldsymbol{b} \end{Bmatrix} = \boldsymbol{G}^{-1} \begin{Bmatrix} \boldsymbol{u_s} \\ \boldsymbol{0} \end{Bmatrix} \tag{3.13}$$

Finally, it is possible to represent the shape function in the following way,

$$u(\boldsymbol{x}_\mathrm{I}) = \{\boldsymbol{R}^T(\boldsymbol{x}_\mathbf{I}), \boldsymbol{p}^T(\boldsymbol{x}_\mathrm{I})\}\boldsymbol{G}^{-1} \begin{Bmatrix} \boldsymbol{u_s} \\ \boldsymbol{0} \end{Bmatrix} = \varphi(\boldsymbol{x}_\mathbf{I}) \begin{Bmatrix} \boldsymbol{u_s} \\ \boldsymbol{0} \end{Bmatrix} \tag{3.14}$$

For a two-dimensional analysis:

$$\begin{aligned} \varphi_{,x}(\boldsymbol{x}_\mathrm{I}) &= \{\boldsymbol{R}^T(\boldsymbol{x}_\mathrm{I}), \boldsymbol{p}^T(\boldsymbol{x}_\mathrm{I})\}_{,x}\boldsymbol{G}^{-1} \\ \varphi_{,y}(\boldsymbol{x}_\mathrm{I}) &= \{\boldsymbol{R}^T(\boldsymbol{x}_\mathrm{I}), \boldsymbol{p}^T(\boldsymbol{x}_\mathrm{I})\}_{,y}\boldsymbol{G}^{-1} \end{aligned} \tag{3.15}$$

Chapter 4

Solid mechanics

4.1 - Fundamentals

Different materials behave differently when exposed to loads or forces as they have different stress-strain curves. The application of a load leads to stresses, which can be analyzed by the occurrence of deformations/displacements. In elastic materials after the application of a force, the body deforms. If the force ceases, the deformation disappears and the object acquires the previous form the application of the force. In plastic materials, this behavior is not observed and after the force ceases a residual deformation remains. In addition to the elastic or plastic properties, the materials can still have the same properties in all directions (isotropic) or vary their properties along different directions (anisotropic).

Next, some important concepts will be presented for the analysis of the behavior of certain materials exposed to different conditions. The first concept to be presented is the Cauchy stress tensor ($\boldsymbol{\Lambda}$) in the two-dimensional case is given by,

$$\boldsymbol{\Lambda} = \begin{bmatrix} \sigma_{xx} & \sigma_{xy} \\ \sigma_{xy} & \sigma_{yy} \end{bmatrix} \tag{4.1}$$

Using the vector notation of Voigt the stress tensor is represented by vector $\boldsymbol{\sigma}$,

$$\boldsymbol{\sigma} = \{\sigma_{xx} \quad \sigma_{yy} \quad \sigma_{xy}\}^T \tag{4.2}$$

Similarly, the strain tensor can also be represented in its vector form ($\boldsymbol{\varepsilon}$),

$$\boldsymbol{\varepsilon} = \{\varepsilon_{xx} \quad \varepsilon_{yy} \quad \varepsilon_{xy}\}^T \tag{4.3}$$

being,

$$\varepsilon_{xx} = \frac{\partial u}{\partial x}$$

$$\varepsilon_{yy} = \frac{\partial v}{\partial y} \tag{4.4}$$

$$\varepsilon_{xy} = \frac{\partial u}{\partial x} + \frac{\partial v}{\partial y}$$

Thus, the strain can also be represented by,

$$\boldsymbol{\varepsilon} = \boldsymbol{L}\boldsymbol{u} \tag{4.5}$$

Where $\boldsymbol{L}$ is the matrix given by:

$$\boldsymbol{L} = \begin{bmatrix} \frac{\partial}{\partial x} & 0 & \frac{\partial}{\partial y} \\ 0 & \frac{\partial}{\partial y} & \frac{\partial}{\partial x} \end{bmatrix}^T \tag{4.6}$$

Linear elastic isotropic materials are completely defined by the Young's modulus and the Poisson's coefficient. In these materials it is possible to apply the Hooke's law, correlating the stress with the strain,

$$\boldsymbol{\sigma} = \boldsymbol{c}\boldsymbol{\varepsilon} \tag{4.7}$$

$\boldsymbol{c}$ represents the material constitutive matrix. The above equation can be expressed in terms of the strain,

$$\boldsymbol{\varepsilon} = \boldsymbol{s}\boldsymbol{\sigma} \tag{4.8}$$

With the matrix $\boldsymbol{s} = \boldsymbol{c}^{-1}$ and considering an anisotropic material the $\boldsymbol{s}$ matrix for stress in the plane is expressed by,

$$\boldsymbol{s} = \begin{bmatrix} \frac{1}{E_x} & -\frac{v_{yx}}{E_y} & 0 \\ -\frac{v_{yx}}{E_x} & \frac{1}{E_y} & 0 \\ 0 & 0 & \frac{1}{G_{xy}} \end{bmatrix} \tag{4.9}$$

and v_{ij} is the Poisson coefficient in the direction j and characterizes the deformation in that direction for a force applied in the i direction. E_{ii} represents the modulus of elasticity in the i direction and for the angle between the directions i and j, finally, G_{ij} represents the shear modulus.

Also for an anisotropic material if the plane strain assumption is considered, the matrix $\boldsymbol{s}$ is represented by,

$$\boldsymbol{s} = \begin{bmatrix} \frac{1 - v_{31}v_{13}}{E_{11}} & -\frac{v_{12} + v_{31}v_{23}}{E_{22}} & 0 \\ -\frac{v_{12} + v_{32}v_{13}}{E_{11}} & \frac{1 - v_{32}v_{23}}{E_{22}} & 0 \\ 0 & 0 & \frac{1}{G_{12}} \end{bmatrix} \tag{4.10}$$

Given the constitutive matrix or matrix $\boldsymbol{c}$ it is possible to apply a rotation on it, resulting in an alignment with a new $O_{x'y'}$ axis system. The new constitutive matrix $\boldsymbol{c}'$ can be calculated by the following relation:

$$\boldsymbol{c}' = \boldsymbol{T}^{\boldsymbol{T}}\boldsymbol{c}\,\boldsymbol{T} \tag{4.11}$$

Where the transformation matrix $\boldsymbol{T}$ is given by,

$$\boldsymbol{T} = \begin{bmatrix} \cos^2\alpha & \sin^2\alpha & -\sin 2\alpha \\ \sin^2\alpha & \cos^2\alpha & \sin 2\alpha \\ \sin\alpha.\cos\alpha & -\sin\alpha.\cos\alpha & \cos^2\alpha\,.\sin^2\alpha \end{bmatrix} \tag{4.12}$$

whith $\alpha = \cos^{-1}(i, i')$.

4.2 - Galerkin weak formulation

The strong formulation allows to obtain the exact solution of a given problem. The major disadvantage of this formulation is the high degree of difficulty imposed by complex problems. An approximate solution in turn is obtained by the weak formulation. A detailed description of Galerkin's weak formulation will be presented below.

Considering an external force $\boldsymbol{t}$ applied to a solid whose domain is $\boldsymbol{\Omega}$ and is delimited by the boundary condition $\boldsymbol{\Gamma}$. The boundary condition mentioned here can be of two types or natural boundary conditions $\boldsymbol{\Gamma_t}$ or essential boundary conditions $\boldsymbol{\Gamma_u}$ border (Figure 4. 1). The first type is related to the forces, binary or imposed loads, the second type is related to the impediments/impositions of certain displacements (Belinha 2004).

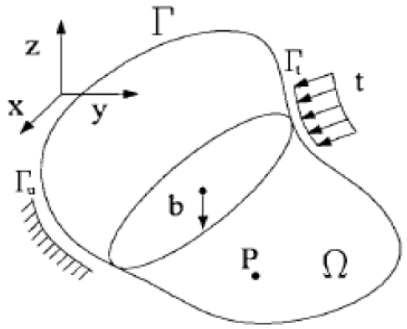

Figure 4. 1- Domain of problem.

The principle of energy minimization represents the basis of the variational method that constitutes Galerkin's weak formulation.

Given a problem the configuration of displacements more precise (in relation to the real configuration) is the one that minimizes the Lagrangian (L),

$$L = T - \pi_s + W_f \tag{4.13}$$

Where L represents the elastic potential energy that depends on the kinetic energy T the strain energy π_s and the work performed by the external forces W_f. The parameters referred previously are determined by the following integrals,

$$T = \frac{1}{2}\int_{\Omega} \rho \dot{\boldsymbol{u}}^T \dot{\boldsymbol{u}}\, d\Omega \tag{4.14}$$

$$\pi_s = \frac{1}{2}\int_{\Omega} \boldsymbol{\varepsilon}^T \boldsymbol{\sigma}\, d\Omega \tag{4.15}$$

$$W_f = \int_{\Omega} \boldsymbol{u}^T \boldsymbol{b}\, d\Omega + \int_{S_t} \boldsymbol{u}^T\, \boldsymbol{t}\, dS_t \tag{4.16}$$

Where $\dot{\boldsymbol{u}}$ represents the velocity, ρ the density of the material, $\boldsymbol{\varepsilon}$ and $\boldsymbol{\sigma}$ the stress and deformation imposed on the body. On the other hand, $\boldsymbol{b}$ represents the force of the body, $\boldsymbol{t}$ the external forces applied to the body at the boundary S_t.

Thus, the equation (4**.13** can be written as follows,

$$L = \frac{1}{2}\int_{\Omega} \rho \dot{\boldsymbol{u}}^T \dot{\boldsymbol{u}}\, d\Omega - \frac{1}{2}\int_{\Omega} \boldsymbol{\varepsilon}^T \boldsymbol{\sigma}\, d\Omega + \int_{\Omega} \boldsymbol{u}^T \boldsymbol{b}\, d\Omega + \int_{S_t} \boldsymbol{u}^T\, \boldsymbol{t}\; dS_t \tag{4.17}$$

Determining the kinetic energy, the deformation and the work done by the external forces, the principle of energy minimization must be applied, i.e.:

$$\delta \int_{t_1}^{t_2} L \; dt = 0 \tag{4.18}$$

Thus, the weak form of Galerkin is represented as follows,

$$\int_{\Omega} \delta(\boldsymbol{Lu})^T \boldsymbol{cLu} d\Omega - \int_{\Omega} \delta \boldsymbol{u}^T \boldsymbol{b} d\Omega - \int_{S_t} \delta \boldsymbol{u}^T \boldsymbol{t} dS_t = 0 \tag{4.19}$$

With $\boldsymbol{\varepsilon} = \boldsymbol{Lu}$ and $\boldsymbol{\sigma} = \boldsymbol{c\varepsilon} = \boldsymbol{cLu}$.

The principle of virtual work gives a system of discrete equations, using shape functions. According to this principle for an infinitesimal set of equilibrium displacements the total virtual work is zero (Wang and Liu 2002). The shape functions or virtual displacements are defined by,

$$u(\boldsymbol{x_I}) = \sum_{i=1}^{n} \varphi_i(\boldsymbol{x_I}) u_i \tag{4.20}$$

being n the number of nodes that constitute the domain of influence of the node of interest $(\boldsymbol{x_I})$, $\varphi_i(\boldsymbol{x_I})$ is the interpolation function of the method without mesh and u_i the nodal displacements. The virtual displacement (test function) can be written by:

$$\delta u(\boldsymbol{x_I}) = \sum_{i=1}^{n} \varphi_i(\boldsymbol{x_I}) \delta u_i \tag{4.21}$$

Considering NNRPIM and the equation (**4.19** making the respective substitution by (**4.21**,

$$\int_{\Omega} \left(\sum_{i=1}^{n} \varphi_i(\boldsymbol{x_I}) \delta u_i\right)^T \boldsymbol{L}^T \boldsymbol{cL} \sum_{j=1}^{n} \varphi_j(\boldsymbol{x_I}) u_j \; d\Omega - \int_{\Omega} \left(\sum_{i=1}^{n} \varphi_i(\boldsymbol{x_I}) \delta u_i\right)^T \boldsymbol{b} \; d\Omega - \int_{S_t} \left(\sum_{i=1}^{n} \varphi_i(\boldsymbol{x_I}) \delta u_i\right)^T \boldsymbol{t} \; dS_t = 0 \tag{4.22}$$

The equation above can also be written as follows:

$$\sum_{i=1}^{n}\sum_{j=1}^{n}\delta u_i^T \int_\Omega \boldsymbol{B}^T \boldsymbol{c}\boldsymbol{B}\, d\Omega \boldsymbol{u} - \sum_{i=1}^{n}\delta u_i^T \int_\Omega \varphi_i^T(\boldsymbol{x_I})\boldsymbol{b}\, d\Omega - \sum_{i=1}^{n}\delta u_i^T \int_\Omega \varphi_i^T(\boldsymbol{x_I})\boldsymbol{t}\, d\Omega = 0 \tag{4.23}$$

Being the deformation matrix $\boldsymbol{B}$ determined by,

$$\boldsymbol{B} = \begin{bmatrix} \frac{\partial \varphi_i}{\partial x} & 0 & 0 & \frac{\partial \varphi_i}{\partial y} & 0 & \frac{\partial \varphi_i}{\partial z} \\ 0 & \frac{\partial \varphi_i}{\partial y} & 0 & \frac{\partial \varphi_i}{\partial x} & \frac{\partial \varphi_i}{\partial z} & 0 \\ 0 & 0 & \frac{\partial \varphi_i}{\partial z} & 0 & \frac{\partial \varphi_i}{\partial y} & \frac{\partial \varphi_i}{\partial x} \end{bmatrix}^T \tag{4.24}$$

Where for the domain of influence, i represents the order of the node.

The equation (4.**23** can be written as follows,

$$\delta U^T(\boldsymbol{K}\boldsymbol{u} - \boldsymbol{F}) = 0 \tag{4.25}$$

Being,

$$\int_\Omega \boldsymbol{B}^T \boldsymbol{c}\boldsymbol{B}\, d\Omega \boldsymbol{u} = \boldsymbol{K}\boldsymbol{u} \tag{4.26}$$

and

$$\int_\Omega \varphi_i^T(\boldsymbol{x}_I)\boldsymbol{b}\, d\Omega + \int_{S_t} \varphi_i^T(\boldsymbol{x}_I)\boldsymbol{t}\, dS_t = \boldsymbol{F} \tag{4.27}$$

Chapter 5

State of the art review

5.1 - Geometry

Different constitutive models, different geometries, or different numerical methods can be used to simulate RBCs. Studies also vary in the number of cells used in the simulation. It is possible to use models with one cell, some cells, or many cells.

As for geometry, previous studies are divided between two-dimensional models and three-dimensional models.

Two-dimensional models are used to determine the deformation of a RBC under different flow conditions (Hosseini and Feng 2009), to simulate the RBCs inside a blood vessel (Hosseini and Feng 2009),(Nayanajith, Saha, and Gu 2013) or even to study the deformation of two aggregated RBCs (Li, Ye, and K.Y. 2014). In other two-dimensional studies, blood flow is analyzed to determine the trajectory, velocity and fluctuations of RBCs within a microvessel (Bagchi 2007),(Ahmadian, Firoozbakhsh, and Hasanian 2012).

Two-dimensional models (2D) are simple models that in many situations allow an approximation to reality. However, three-dimensional models (3D) represent more faithfully the behavior of cells in the body. It should be noted that the transition from a two-dimensional model to a three-dimensional model implies an increase in complexity and computational cost.

Scientists around the world have focused on the study of pathologies such as malaria. Malaria affects a significant portion of the population and the costs of treating it are very high. Thus, to study the behavior of RBCs infected with malaria, 3D models have been implemented to simulate the progression of RBCs in a channel and to study the evolution of infection during the three malaria infection states (Wu et al. 2013). Also on the study of malaria a simulation was developed comparing the cellular behavior of the infected RBCs with the non-infected RBCs (Ye et al. 2013),(Hosseini and Feng 2012).

Through a 3D model it is possible to study the behavior of a RBC or multiple RBCs in different forms of bifurcations (Hyakutake and Nagai 2015).

5.2 - Type of numerical method

For the study of RBCs, the use of numerical simulations is essential. In the simulations, essentially three methods are applied: mesh based methods, meshless methods based on particles and hybrid methods. Meshless methods or particle-based methods can be used in models with very distinct length scales. Generally, the literature defines the following scales: macroscopic, mesoscopic, and microscopic. As the dimensions of the RBCs are very small, in the simulation of these cells the macroscopic and mesoscopic methods are employed (Ye, Phan-thien, and Teck 2016). In cell simulations, and in particular RBCs, the most commonly used numerical methods are the finite element method (FEM) (Dao et al. 2003; Kam et al. 2006), the dissipative particle dynamics (DPD) method (Fedosov et al. 2011; Peng et al. 2013), the smoothed particle hydrodynamics (SPH) method (Hosseini and Feng 2009, 2012; Wu et al. 2013) and the lattice Boltzmann method (LBM) combined with immersed boundary method (IBM) (Crowl and Fogelson 2010; Hyakutake and Nagai 2015; Krüger et al. 2014). In addition to these methods other methods can be used (Fedosov and Noguchi 2013; Xu et al. 2013). A detailed description of each of these methods can be found below.

DISSIPATIVE PARTICLE DYNAMICS

In a model of the dissipative particle dynamics (DPD), the RBCs and the surrounding environment (fluid) are discretized in 4 types of particles that interact with each other. These particles represent a set of atoms or molecules and simulate four types of components, the fluid circulating in the vessel, the walls of the vessel, the membrane of the RBCs, and the fluid inside the cell (Ye et al. 2014). The fundamental law of dynamics rules the movement of all the particles of the model (Ye et al. 2014, 2016),

$$m_i \frac{d^2 r_i}{dt^2} = \sum_{j \neq i} f_{ij}^{DPD} \qquad i \in P_{D\setminus M} \tag{5.1}$$

$$m_i \frac{d^2 r_i}{dt^2} = \sum_{j \neq i} f_{ij}^{DPD} + F_i^M \qquad i \in P_M, \tag{5.2}$$

Where for a given particle i, m_i represents its mass and $\frac{d^2 r_i}{dt^2}$ its acceleration which depends on the position r_i and time t. $P_{D\setminus M}$ represents the set containing all particles except those belonging to the membrane. In turn P_M represents the set of particles belonging to the

membrane. f_{ij}^{DPD} and F_i^M are the established force between two particles and the force of the membrane respectively. The force f_{ij}^{DPD},

$$f_{ij}^{DPD} = f_{ij}^C + f_{ij}^D + f_{ij}^R \tag{5.3}$$

It decomposes into the forces: conservative f_{ij}^C, dissipative f_{ij}^D, and random f_{ij}^R. f_{ij}^C determined the compressibility of the fluid, f_{ij}^D the viscosity of the fluid, f_{ij}^R the maintenance of the temperature of the system.

SMOOTHED PARTICLE HYDRODYNAMICS

For a given fluid its flow behavior can be studied using the smoothed particle hydrodynamics (SPH) method. In this method the membrane of the RBC adopts an elastic behavior and includes in its interior a viscous and Newtonian cytosol. Initially, the RBC is discretized in three-dimensional distributed particles that interact with each other and move according to Newton's second law. In simulations using SPH, a smoothing length parameter is used, corresponding to the spatial distance of each particle. This parameter allows to obtain any physical property (speed, density or pressure) as a function of the Kernel function (Hosseini and Feng 2012; Wu et al. 2013; Ye et al. 2016).

In the SPH method the incompressibility is replaced by a low compressibility, in order to simplify the method. Thus, the motion of particles is governed by the following equations,

$$\frac{D\rho}{Dt} = -\rho \nabla . v \tag{5.4}$$

$$\frac{Dv}{Dt} = g + \frac{1}{\rho}\nabla . T_{vis} - \frac{1}{\rho}\nabla p \tag{5.5}$$

$$\frac{p}{p_0} = \left(\frac{\rho}{\rho_0}\right)^7 - 1 \Leftrightarrow p = p_0\left[\left(\frac{\rho}{\rho_0}\right)^7 - 1\right] \tag{5.6}$$

$\frac{D}{Dt}$ is the derivative of the material, g is the gravitational acceleration, ρ and ρ_0 is the density and the reference density respectively, t the time, p and p_0 respectively the pressure and the reference pressure, v the velocity and T_{vis} the tensor of the viscous stress. A more detailed description of this method can be found in (Hosseini and Feng 2009).

LATTICE BOLTZMANN METHOD

The lattice Boltzmann method (LBM) is a method that locally studies the evolution of certain fictitious neighboring particles in a network in order to gauge the behavior of a Newtonian fluid. In this method a rectangular two-dimensional domain is considered, on

which a network is used to form square cells with length h. The interest of this method resides in the calculation of the function of density of particles. For a given point in the network x, a given discrete velocity vector v_i in a direction i and a time t the particle density function $f(x, v_i, t)$ is given by (Crowl and Fogelson 2010; Shi et al. 2013),

$$f_i(x + v_i\Delta t, t + \Delta t) = f_i(x, v_i, t) - \frac{1}{t_r} f_i(x, t) - f_i^{eq}(\rho(x, t), v(x, t)) \quad (5.7)$$

With Δt a represents the integration step of the method, t_r is the relaxation time, f_i^{eq} is the equilibrium distribution function.

Using the particle density function, it is possible to calculate the density ρ and the momentum of the fluid ρv through the following relations:

$$\rho = \sum_i f_i \quad (5.8)$$

$$\rho v = \sum_i v_i f_i + \frac{1}{2} f \Delta t \quad (5.9)$$

f represents for the boundary and the field of flow considered the force of the body (Ye et al. 2016).

IMMERSED BOUNDARY METHOD

In simulations involving the interaction of fluids with membranes, the immersed boundary method (IBM) is often used. Simulations of aggregation of RBCs or deformation of RBCs in blood flow are examples of simulations where one can turn to IBM.

In IBM, it is assumed that the membrane of each RBC has a negligible mass and has an elastic behavior in its interior and exterior are a viscous incompressible and Newtonian fluids. The description of the behavior of the incompressible fluids at each point x of the space is described by the Navier Stokes equations (Crowl and Fogelson 2010; Navidbakhsh and Rezazadeh 2012),

$$\rho\left[\frac{\partial}{\partial t}\boldsymbol{v}(\boldsymbol{x}, t) + \boldsymbol{v}(\boldsymbol{x}, t).\nabla\boldsymbol{v}(\boldsymbol{x}, t)\right] = -\nabla p(\boldsymbol{x}, t) + \mu\nabla^2\boldsymbol{v}(\boldsymbol{x}, t) + F_f(\boldsymbol{x}, t) \quad (5.10)$$

$$\nabla.\boldsymbol{v}(\boldsymbol{x}, t) = 0 \quad (5.11)$$

In this equation, the density ρ and the viscosity μ are constant. The variable $v(\boldsymbol{x}, t)$ represents the velocity of the fluid and the variable $p(\boldsymbol{x}, t)$ is its pressure. The elastic deformation of the RBCs induces a force F_f to the surrounding fluid. In this method it is also

possible to measure the elastic force per unit reference length of the arc l at a given time t and at a point $\boldsymbol{X}$ of the membrane,

$$F_{IB}(l,t) = \frac{\partial}{\partial q}(Tt) = S\frac{\partial}{\partial l}\left[\left(\| \frac{\partial X}{\partial l} \| - 1\right)\frac{\frac{\partial X}{\partial l}}{\| \frac{\partial X}{\partial l} \|}\right] \tag{5.12}$$

Considering that the membrane has a stiffness S and is subjected to a stress T. With said previously the deformation (elastic force) of the membrane induces a force F_f to the surrounding fluid. Mathematically the force F_f is given by:

$$F_f(x,t) = \int F_{IB}(l,t)\delta(x - X(l,t)dl \tag{5.13}$$

Where $\delta(x)$ represents the Dirac delta function.
In IBM, it is still required that all points of the membrane move with the same velocity of the surrounding fluid,

$$\frac{\partial X}{\partial t}(l,t) = v(X(l,t),t) = \int v(x,t)\delta\big(x - X(l,t)\big)dx \tag{5.14}$$

5.3 - Explicit formulations

Shell-based models

There are many models developed to express the deformability of the membrane. The shell models describe the cell continuously in two dimensions in the form of a curve with finite thickness (Hartmann 2010; Li et al. 2014; Taylor et al. 2013), as described in the following text.

The membrane stress can be decomposed in terms of stress in the plane (c) and in terms of transverse stress (q) (Figure 5.1). The tangential and normal directions to the surface of the RBC are represented by the respective vectors $\boldsymbol{t}$ and $\boldsymbol{n}$:

$$T(l) = \mathrm{c}(l)\mathbf{t}(l) + \mathrm{q}(l)\boldsymbol{n}(l) \tag{5.15}$$

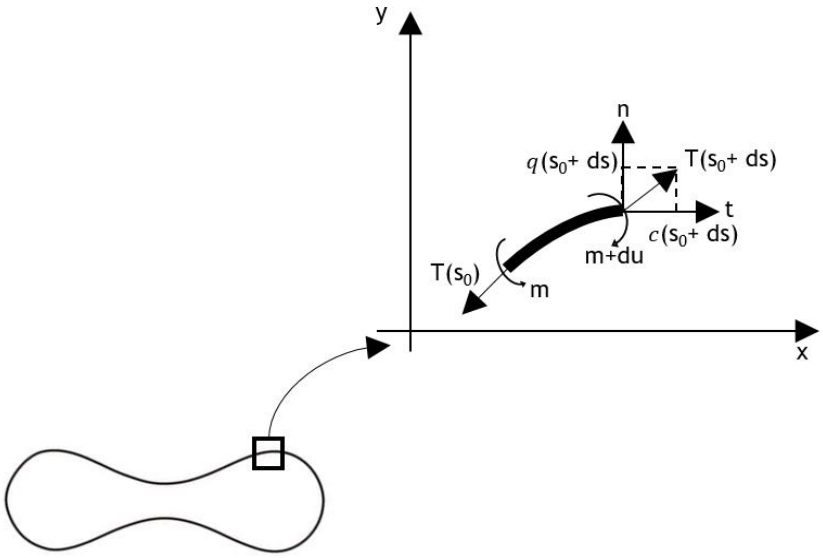

Figure 5.1 - Decomposition of membrane stress.

The transverse stress q is given by:

$$q = \frac{d_m}{dl} \tag{5.16}$$

Where l represents the length of the curved section to be considered. To this the section is associated with a curvature k and a force per unit area of the membrane (F_a) is given by:

$$F_a = \frac{\mathrm{dT}}{dl} = -\frac{d}{d_l}(\mathrm{c}\mathbf{t} + \mathrm{q}\mathbf{n}) = \left(\frac{dc}{dl} + k\frac{dm}{dl}\right)t + \left(\frac{d^2m}{dl^2} - kc\right)n \tag{5.17}$$

The bending moment (m) is represented by bending stiffness (E_B) and curvature at rest (k_0) by:

$$m = E_B(k - k_0) \tag{5.18}$$

And the stress in the plane (c) is given as a function of the elastic modulus of shear (G) and the strain at rest (ε) by:

$$c = G\varepsilon \tag{5.19}$$

Spring-based models

The membrane of the RBCs can also be represented by means of spring models, which allow to model the cell as a two-dimensional and three-dimensional solid. These models are based on a simple mathematical description where the membrane is discretized in a network that can take various forms (Imai et al. 2016). The most frequently used form is a triangular network. At the base of this model is the implementation of a network of springs where the

nodal points take the form of friction-free hinges. The elastic resistance assigned to each of the springs is proportional to the size of the springs.

The RBC membrane is a system whose deformation depends on the free energy,(Discher, Boal, and Boey 1998; Li et al. 2005; Taylor et al. 2013) as described in the following text. The free energy (ψ) is given by,

$$\psi = E_N + E_B + E_A + E_V \tag{5.20}$$

Where E_N represents the energy obtained at the time of a reversible deformation of the membrane skeleton or Spectrin's network. Being mathematically expressed by:

$$E_N = \sum_j \frac{k_b T l_m (3x_j^2 - 2x_j^3)}{4l_p(1 - x_j)} + \sum_a \frac{C}{A_a} \tag{5.21}$$

Where C represents a constant, k_b represents the bending constant, l_p represents a persistence length and the energy unit is given by $k_b T$. Each spring (j) corresponds to a maximum length (l_m) and a length (l_j) which are related by a ratio of length x_j (l_j / l_m). Each triangle belonging to the triangular network has an area A_a.

The number of phospholipids constituting the membrane is always maintained constant throughout the life of the cell so it is necessary to preserve the surface area,

$$E_A = \frac{k_a (A - A_0^t)^2}{2A_0^t} + \sum_j \frac{k_d (A_j - A_0)^2}{2A_0} \tag{5.22}$$

For the calculation of the free energy it is still important to consider the imposed volume constraints due to the cytosol of the cell once its cytosol is incompressible E_V.

$$E_V = \frac{k_v (V - V_0^t)^2}{2V_0^t} \tag{5.23}$$

where k_a represents the coefficient of total surface area k_d the coefficient of the study area or local area and k_v in turn represents the coefficient of restriction of the volume. In turn, A represents the total area and V the total volume. While A_0^t and V_0^t represents the area and volume to be analyzed in detail.

The bilayer of phospholipids confers resistance to flexion the RBCs and the energy of flexion (E_B) is given by,

$$E_B = \sum_j k_b [1 - \cos(\theta_j - \theta_0)] \tag{5.24}$$

For two adjacent triangles that share a side and the angle formed between the triangles is the θ_j also called the instantaneous angle while θ_0 represents the spontaneous angle angle.

5.4 - Constitutive model

Hyperelastic model

In several studies the membrane of RBCs is represented using shell models. This membrane when exposed to stresses undergoes an elastic deformation with a non-linear behavior. Hyperelastic models are predictive models of cell deformation. The most commonly used hyperelastic model is neo-Hookean (Dao et al. 2003; Lim and Dao 2004; Yoon and You 2016). The neo-Hookean formulation takes into account cell volume conservation (incompressibility). In this formulation, the potential energy of deformation,

$$\psi = \frac{G}{2}(\lambda_1^2 + \lambda_2^2 + \lambda_3^2 - 3) = C_1(\lambda_1^2 + \lambda_2^2 + \lambda_3^2 - 3) \tag{5.25}$$

depends on the initial shear modulus G and the principal extension parameters λ_i, in each direction i with $i = 1,2,3$. Assuming that the RBC membrane is incompressible it can be stated that $\lambda_1\lambda_2\lambda_3 = 1$.

If the RBC membrane is exposed to a uniaxial elongation, the stress T_2 is zero and the stress T_1 is obtained by the derivative of ψ,

$$T_1 = S\lambda_1 \frac{\partial \psi}{\partial \lambda_1} = \frac{S_0}{\lambda_1\lambda_2}\lambda_1 \frac{\partial \psi}{\partial \lambda_1} \tag{5.26}$$

With S representing the final thickness of RBC and S_0 the initial thickness. The shear stress of the membrane (τ) subjected to a uniaxial stress is expressed by,

$$\tau = \frac{1}{2}(T_1 - T_2) = \frac{1}{2}\mu(\lambda_1^2 - \lambda_2^2) \tag{5.27}$$

where G represents the shear modulus,

$$G = 2S_0C_1 \tag{5.28}$$

Another important parameter in the characterization of the deformation is the energy of bending,

$$E_B = \frac{2}{3}C_1S_0^3 \tag{5.29}$$

Viscoelastic model

The membrane of RBCs can also be represented using spring models. The membrane of the RBCs demonstrates an anisotropic behavior yet according to the plane of the membrane behaves as an isotropic material. Any tension applied according to the plane of the membrane does not lead to a change in thickness but rather to a change in shape of a given element belonging to the surface. Since the cell thickness is invariant any applied force on the surface is applied per unit length. In a viscoelastic model, we consider the internal energy dissipated and the free elastic energy, as can be seen in (Hochmuth 1976; Yoon and You 2016). According to the viscoelastic model proposed by Maxwell the free elastic energy (ψ),

$$\psi = \psi_{elasticity} + \sum_{i=1}^{n} G \parallel \varepsilon' - \alpha_i \parallel^2 \tag{5.30}$$

is dependent on the shear modulus G of each spring, the internal stress α_i of each arm and ε' representing the deviation of the strain tensor ε. The internal energy dissipated (ϕ) in turn is given by,

$$\phi = \sum_{i=1}^{n} \frac{1}{2\mu} \parallel F_i \parallel^2 \tag{5.31}$$

E depends on the viscosity (μ) and the force applied on each of the arms F_i.

5.5 - Solid fluid interaction

In recent years many hemodynamic studies have examined the behavior of blood flow in capillaries, venules, and arterioles. Some of these studies particularly examine the behavior of RBCs in the course of blood flow. This approach attempts to understand the existence (or not) of a relation between the blood flow and determined pathologies, such as, infarcts (cerebral and cardiac) atherosclerosis, arterial hypertension and determined inflammations (Chedlishvili and Aeda 2001; Lanotte et al. 2016; Melchionna 2011).

Blood is composed mostly of RBCs. The diameter of these cells when undeformed is greater than the diameter of a microvessel. Because of this, the flow regime varies according to the diameter of the vessel where the flow is inserted. Behaving as a suspension in vessels with a diameter greater than 0.2 mm and structured in smaller vessels. In capillaries and during a blood flow the membranes of the RBCs interact with the membranes of the endothelial cells present in the inner part of a blood vessel, but the structure of both cells remains unchanged throughout the several blood circulations. The flow resistance is directly related to the number of RBCs present in the flow (Chedlishvili and Aeda 2001). The pressure-

dependent flow study for two samples with a percentage by volume of RBCs of 0% and 23% respectively was done in (Stauber et al. 2017).

5.6 - Aggregation of RBCs

The phenomenon of aggregation of RBCs has already been the subject of many studies, which indicate the aggregation of RBCs is directly related to some properties of these cells, such as their geometry, deformation capacity and biochemical constitution (Chedlishvili and Aeda 2001; Liu and Liu 2006; Xu et al. 2013; Yoon and You 2016).

The RBCs subjected to small shear rates are aggregated, forming structures called "rouleaux". Under certain conditions a further increase in shear rates leads to complete rouleaux fragmentation or dispersion of RBCs. However, when the rouleaux form inside a small diameter blood vessel, such as a microvessel, the shear forces may not cause aggregate fragmentation (Fedosov and Noguchi 2013). Under these conditions within the microvessel there is an increase in entropy, reduction of the flow velocity or its suppression (Chedlishvili and Aeda 2001).

The aggregation of the RBCs occurs due to an adhesion force that acts when these cells are very close. For the aggregation to occur, the macromolecular adhesion force must overcome the electrostatic repulsion force between negatively charged cells. As shown in equation 5.32, the adhesion force (F) is described as a function of the work (W) that is necessary to dissociate two aggregated cells (Xu et al. 2013),

$$F = \frac{Ka^3}{R} - \sqrt{6\pi WKA^3} \tag{5.32}$$

being that A represents the area of contact, K the modulus of elasticity and R the radius of the tip.

Chapter 6

Red blood cells – static analysis

In a first approach, before performing the two-dimensional and three-dimensional simulations of RBCs, a convergence study was carried out. Different meshes were created (**Figure 6. 2**), increasing successively the number of nodes used a given model. This convergence study was performed for numerical methods: FEM; RPIM and NNRPIM.
The constructed models follow realistic geometries documented in the literature (Tomaiuolo 2014). Thus, in Figure 6. 1, there is a schematic of the dimensions of healthy RBCs.

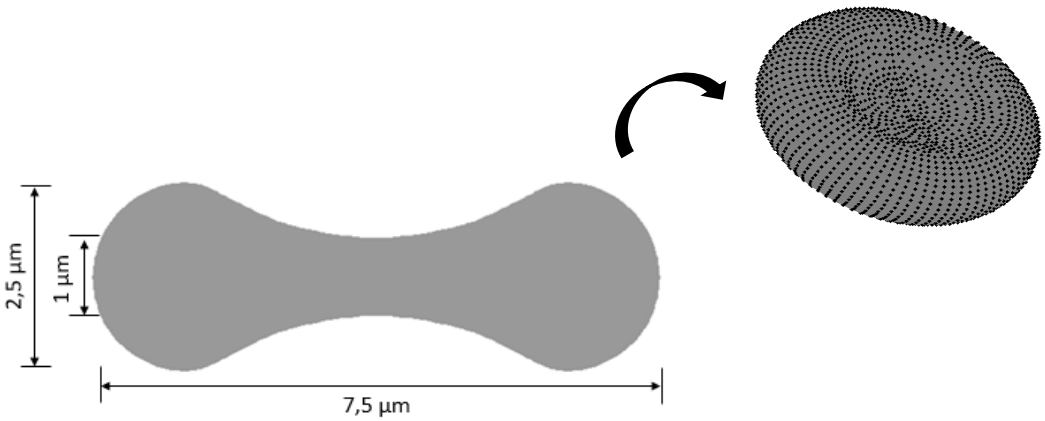

Figure 6. 1- Schematic of the dimensions of healthy RBCs.

In the studies performed in the present thesis, three types of cells were simulated: Healthy cells (H), cells with sickle cell anemia (SC) and cells with ovalocytosis (O) (Figure 6. 2). The mechanical properties used for these three cell types are described in Table 6. 1:

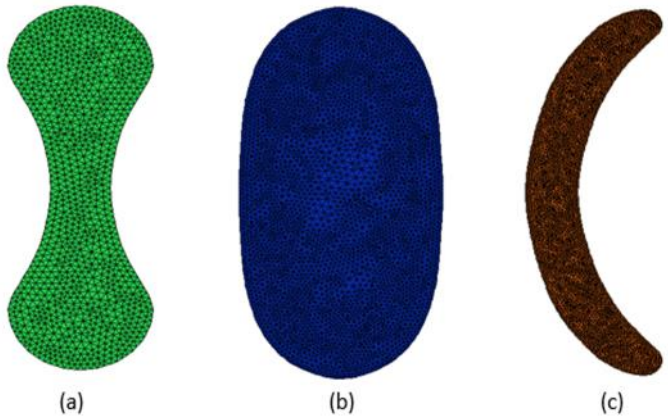

Figure 6. 2 - (a) Mesh for the healthy cell (H) (b) Mesh for the cell with ovalocytosis (O) (c) Mesh for the cell with sickle cell anemia (SC).

RBC	Young's modulus (N/μm)	Poisson coefficient
H	$2{,}6\times10^{-8}$	0,499
SC	$3{,}7143\times10^{-8}$	0,45
O	$8{,}423\times10^{-8}$	O,45

Table 6. 1 - The mechanical properties considered for the three types of cells.

A pressure of 1.6×10^{-8} μPa was applied to each of the cells studied. This pressure represents the blood pressure to which the RBCs are subjected during the blood circulation.

In Figure 6. 3, it is represented the healthy RBC, the cells with sickle cell anemia and cells with ovalocytosis subjected to blood pressure ($p(x)$), and a representative boundary condition of the restrictions to which a cell is subjected when it is forced to pass through blood vessels having dimensions less than the dimension of cell (capilaries). The displacement is constrained normal to the cell surface and a distributed pressure is applied in the top of the cell.

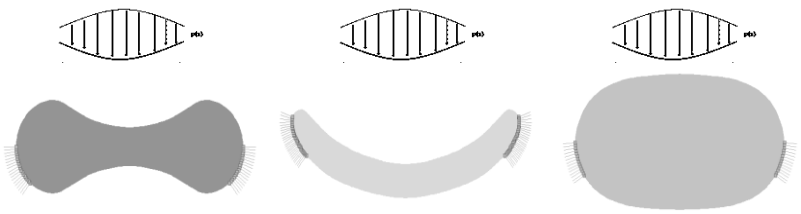

Figure 6. 3- Boundary conditions and a distributed force applied in a healthy cell, cells with sickle cell anemia (SC) and cells with ovalocytosis (O) respectively .

6.1 - Convergence study

Considering the mechanical properties of the health red blood cell and the blood pressure, it is possible to study the influence of the number of the nodes considered in the model and the final results.

In the frist step of the convergence study was created diferents mehs, as it possible visualize in Figure 6. 4.

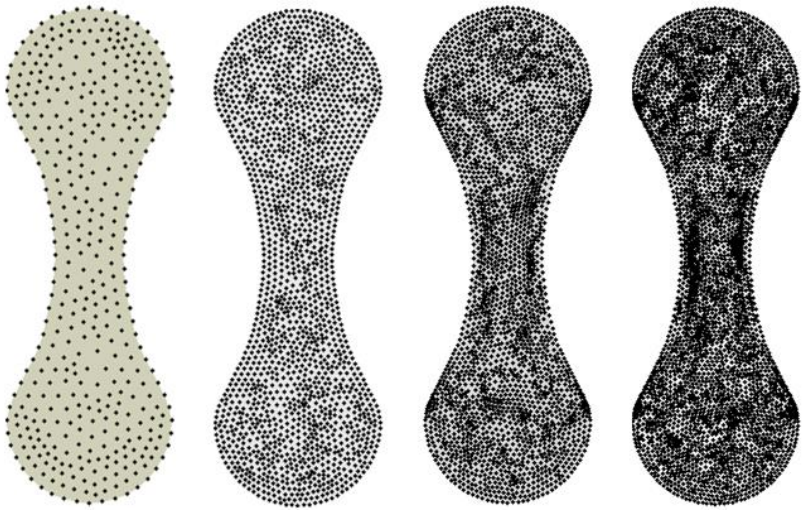

Figure 6. 4 - Gradual increase in the number of nodes used to describe the healthy cell to study mesh convergence.

Through FEMAS academic software, maximum displacements (obtained in the centre point of the cell) were documented for each nodal mesh. The results obtained for the convergence study are shown in the graph of the Figure 6. 5.

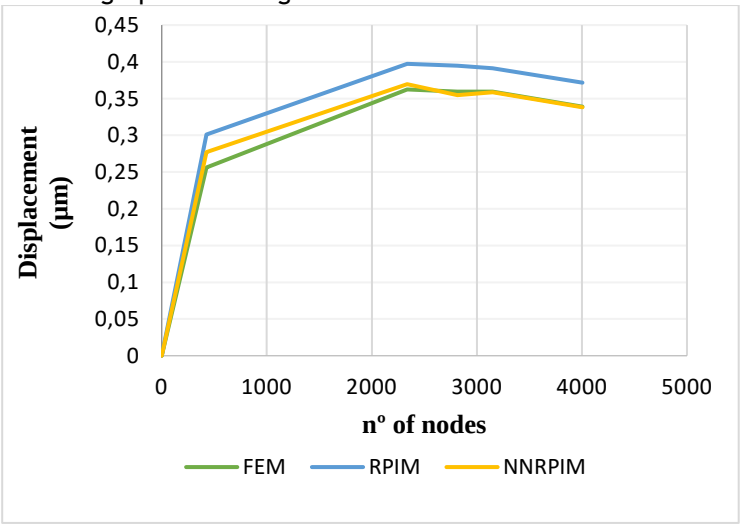

Figure 6. 5 -Displacement in function of the number of nodes that constitute the mesh.

It is known that the increase in the number of nodes leads to better results, however, as can be observed in Figure 6. 5 for a number of nodes above 3500, changes in results are not significant. Thus, it appears that the convervence as already has been achieved.
In this way, the models created must comprise between 3500 and 4000 nodes. In order to obtain good results without leading to an excessive increase of computational cost.

6.2 - Static studies

Considering all the mechanical properties and the blood pressure to which the cells are exposed, several studies have been carried out, some static and others dynamic. These studies were performed for 2D and 3D models. In the two-dimensional studies, it was considered cellular models with five different forms (M1-M5), varying from the healthy to the pathological form. The 3D studies only considered the cells: healthy; with sickle cell anemia and ovalocytosis.
For the static 2D studies, it were analysed the implications of the cell shape in the produced effective stress of Von Mises (σ_{ef}); Equivalent effective strain (ε_{ef}) and displacement (δ).
In order to accomplish the objective of this study, it was assumed that all models studied had a Young's modulus of 2.6×10^{-8} N/μm, that corresponds to Young's modulus of healthy cells.
The results obtained refer to the node (A) located at the bottom of the axis that divides the cell into two equal parts (figure 6.6).
The results for sickle cell anemia are represent in table 6.2 and figures 6.7-6.9 while the results for ovalocytosis are present in table 6.3 and figures 6.10-6.11.

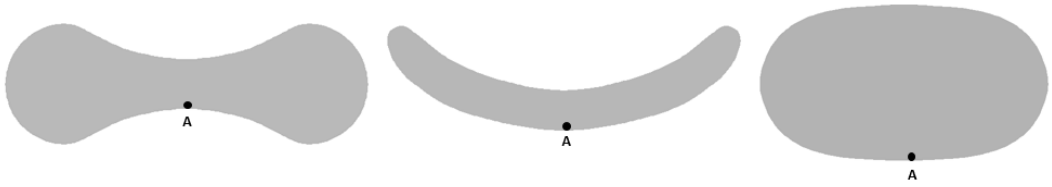

Figure 6. 6- Node considered in the 2D studies.

	Model	E $N/\mu m$	σ_{ef} $N/\mu m^2$	ε_{ef}	δ μm
FEM	M1	2.6×10^{-8}	$2{,}17\times10^{-7}$	4,05	27,29
	M2	2.6×10^{-8}	$5{,}76\times10^{-8}$	1,86	14,22
	M3	2.6×10^{-8}	$5{,}15\times10^{-8}$	1,65	13,19
	M4	2.6×10^{-8}	$6{,}97\times10^{-8}$	2,25	22,71
	M5	2.6×10^{-8}	$1{,}42\times10^{-7}$	4,60	33,39
RPIM	M1	2.6×10^{-8}	$2{,}87\times10^{-7}$	5,58	32,70
	M2	2.6×10^{-8}	$6{,}03\times10^{-8}$	1,94	15,60
	M3	2.6×10^{-8}	$5{,}55\times10^{-8}$	1,80	14,47
	M4	2.6×10^{-8}	$7{,}41\times10^{-8}$	2,43	24,91
	M5	2.6×10^{-8}	$1{,}53\times10^{-7}$	4,98	36,55
NNRPIM	M1	2.6×10^{-8}	$2{,}93\times10^{-7}$	5,05	29,85
	M2	2.6×10^{-8}	$4{,}77\times10^{-8}$	1,59	14,35
	M3	2.6×10^{-8}	$5{,}12\times10^{-8}$	1,67	13.29
	M4	2.6×10^{-8}	$6{,}64\times10^{-8}$	2,20	22,87
	M5	2.6×10^{-8}	$1{,}39\times10^{-8}$	4,55	33,73

Table 6. 2- The effective stress of Von Mises, equivalent effective strain, and displacement predicted by the simulation for sickle cell anemia at the node considered for different numerical methods applied and the boundary conditions present in figure 6.3.

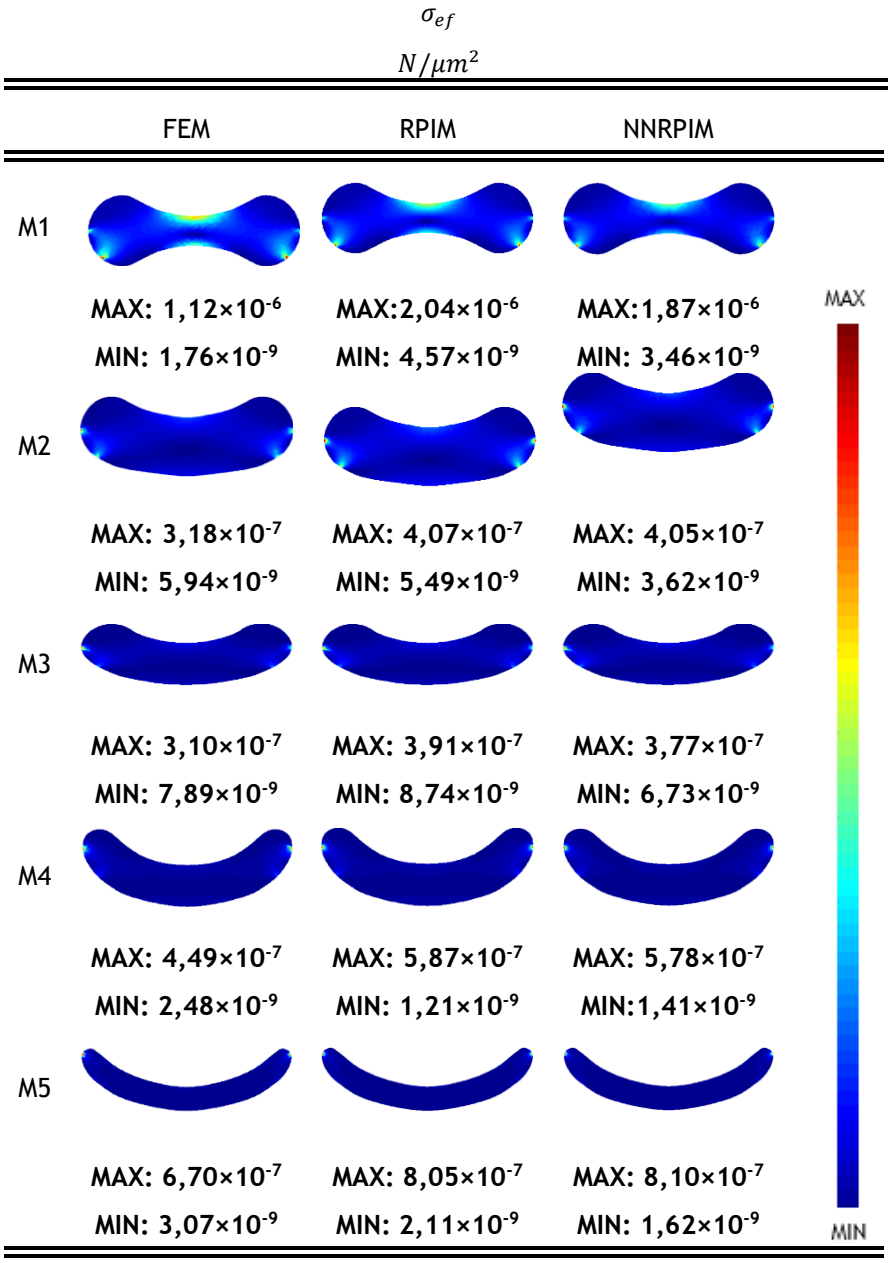

Figure 6. 7- The effective stress of Von Mises that was predicted by the simulation for the five models applying the numerical methods FEM, RPIM and NNRPIM. It was consided that all cells had a Young's modulus of 2.6×10^{-8} N/μm and the boundary conditions present in figure 6.3.

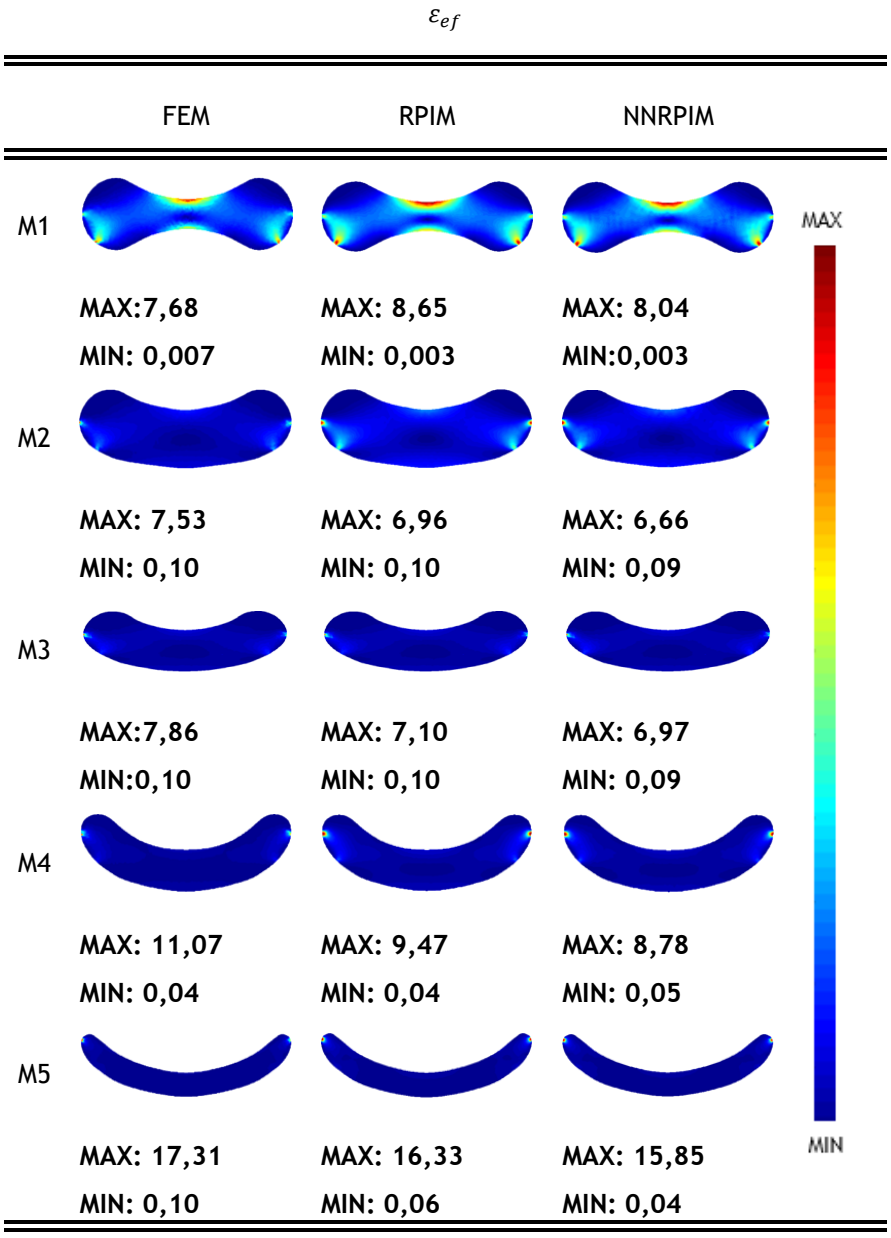

Figure 6. 8 - The equivalent effective strain that was predicted by the simulation for the five models applying the numerical methods FEM, RPIM and NNRPIM. It was consided that all cells had a Young's modulus of 2.6×10^{-8} N/μm and the boundary conditions present in figure 6.3.

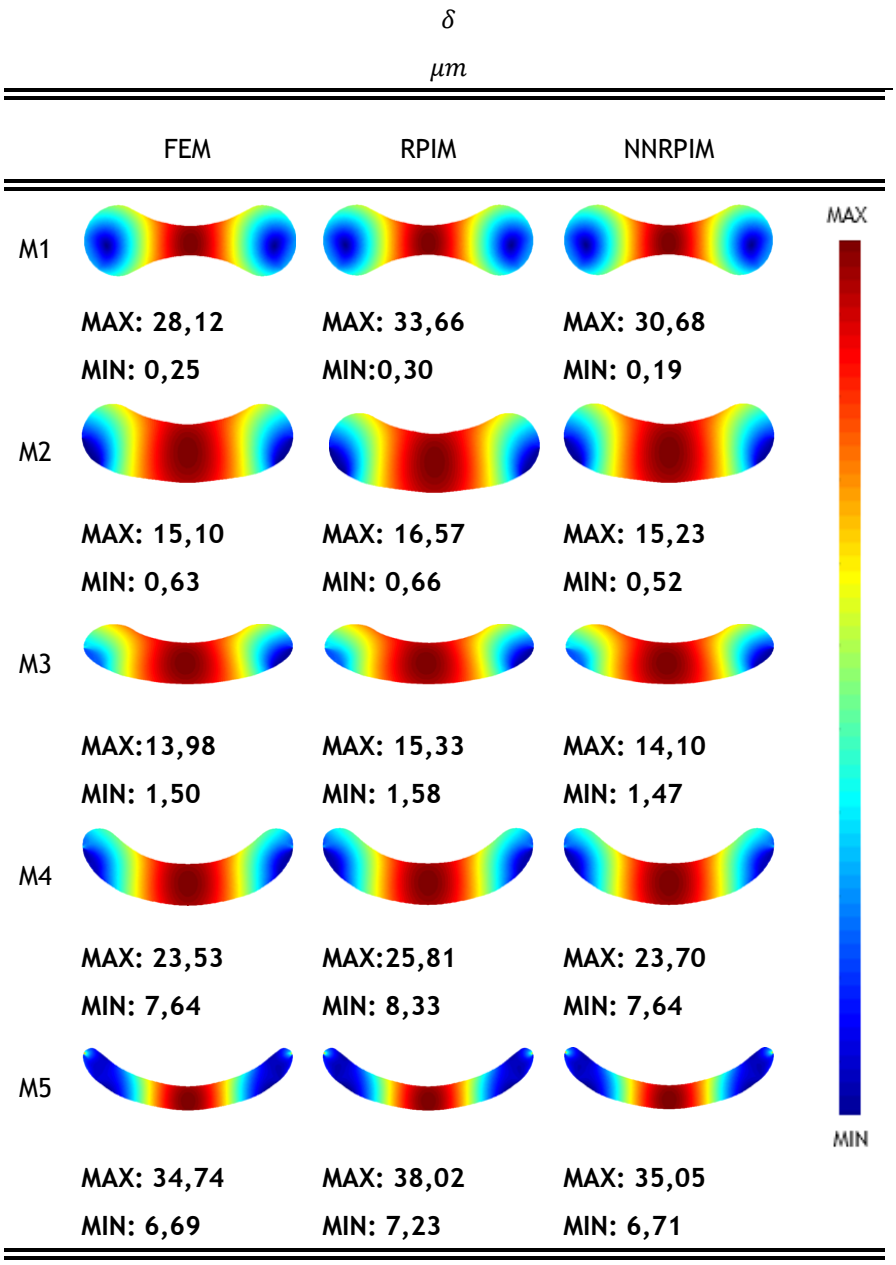

Figure 6. 9 - The displacement that was predicted by the simulation for the five models applying the numerical methods FEM, RPIM and NNRPIM. It was consided that all cells had a Young's modulus of 2.6×10^{-8} N/μm and the boundary conditions present in figure 6.3.

	Model	E $N/\mu m$	σ_{ef} $N/\mu m^2$	ε_{ef}	δ μm
FEM	M1	2.6×10^{-8}	$2{,}17\times10^{-7}$	4,05	27,29
	M2	2.6×10^{-8}	$1{,}02\times10^{-7}$	2,92	18,18
	M3	2.6×10^{-8}	$2{,}29\times10^{-8}$	0,38	9,26
	M4	2.6×10^{-8}	$9{,}53\times10^{-9}$	0,26	11,78
	M5	2.6×10^{-8}	$1{,}09\times10^{-8}$	0,37	16,78
RPIM	M1	2.6×10^{-8}	$2{,}87\times10^{-7}$	5,58	32,70
	M2	2.6×10^{-8}	$9{,}82\times10^{-8}$	3,15	19,99
	M3	2.6×10^{-8}	$2{,}51\times10^{-8}$	0,78	14,66
	M4	2.6×10^{-8}	$8{,}69\times10^{-9}$	0,28	12,92
	M5	2.6×10^{-8}	$1{,}24\times10^{-7}$	0,41	18,52
NNRPIM	M1	2.6×10^{-8}	$2{,}93\times10^{-7}$	5,05	29,85
	M2	2.6×10^{-8}	$9{,}66\times10^{-8}$	3,05	18,43
	M3	2.6×10^{-8}	$2{,}43\times10^{-8}$	0,76	13,48
	M4	2.6×10^{-8}	$7{,}90\times10^{-9}$	0,25	11,89
	M5	2.6×10^{-8}	$1{,}16\times10^{-8}$	0,38	17,05

Table 6. 3 - The effective stress of Von Mises, equivalent effective strain and displacement predicted by the simulation for ovalocytosis at the node considered, for different numerical methods applied and the boundary conditions present in figure 6.3.

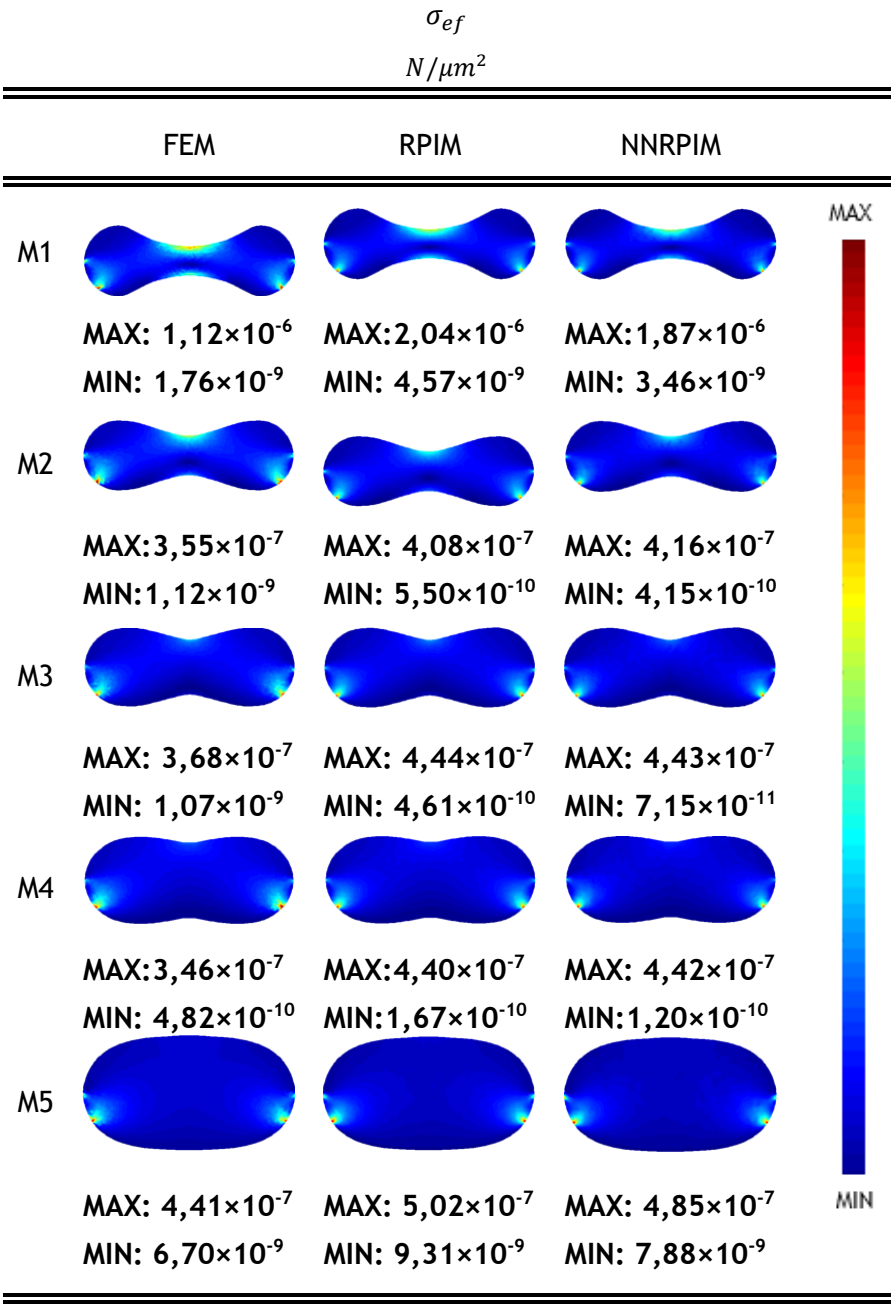

Figure 6. 10 - The effective stress of Von Mises that was predicted by the simulation for the five models applying the numerical methods FEM, RPIM and NNRPIM. It was consided that all cells had a Young's modulus of 2.6×10^{-8} N/μm and the boundary conditions present in figure 6.3.

ε_{ef}

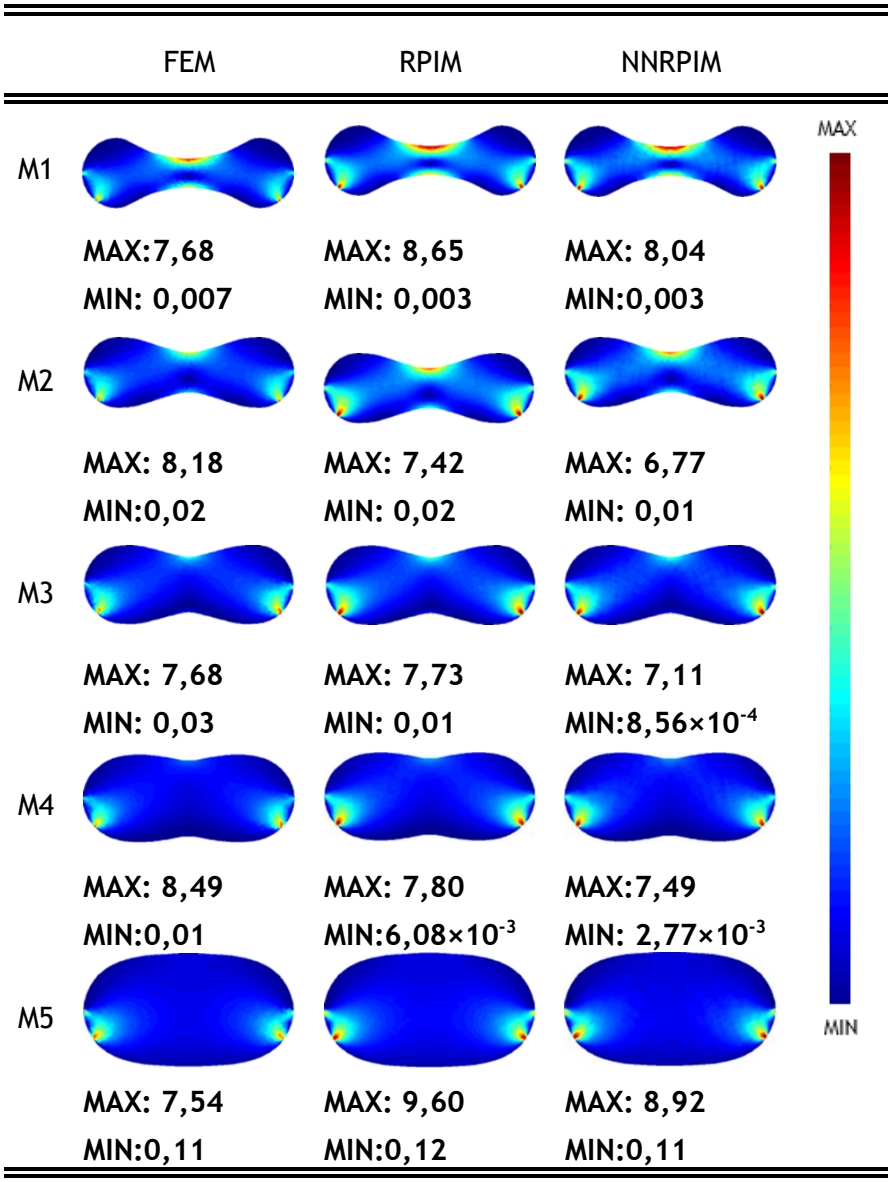

Figure 6. 11 - The equivalent effective strain that was predicted by the simulation for the five models applying the numerical methods FEM, RPIM and NNRPIM. It was consided that all cells had a Young's modulus of 2.6×10-8 N/μm and the boundary conditions present in figure 6.3.

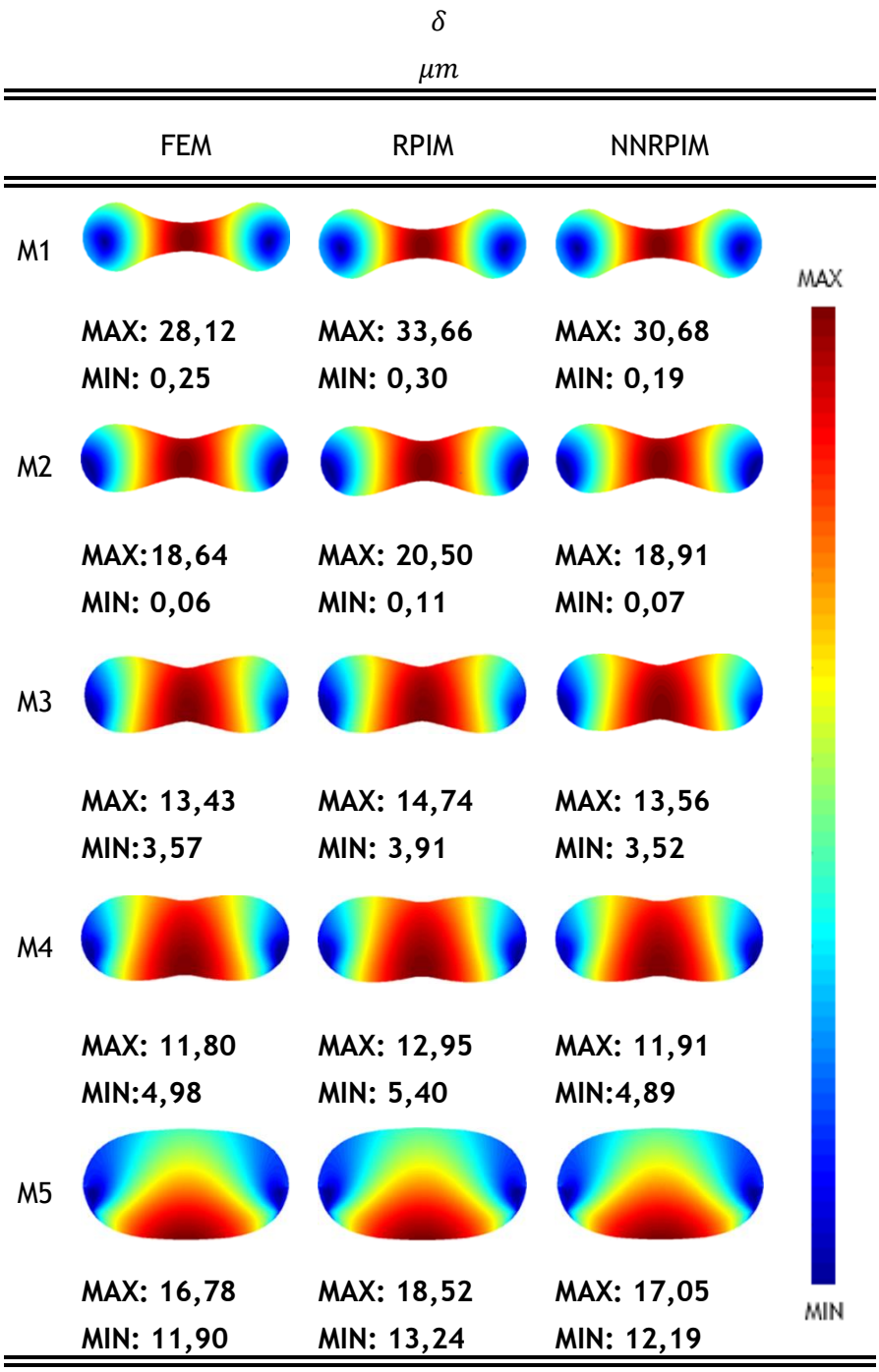

Figure 6. 12 - The displacementthat was predicted by the simulation for the five models applying the numerical methods FEM, RPIM and NNRPIM. It was consided that all cells had a Young's modulus of 2.6×10^{-8} N/μm and the boundary conditions present in figure 6.3.

Still within the static 2D studies, the effective tension of von Mises; equivalent effective strain and displacement were also analysed for all models, considering the different Young's modulus (Table 6. 1) of each cell. This study allows to assess the relevance of the variation of the Young's modulus with the variation of the shape. The results obtained for the case of

sickle-cell anemia are shown in table 6.4 and figure 6.13-6.15, whereas the results obtained for ovalocytosis are in table 6.5 and in the figure 6.16-6.18 . The data in table 6.4 and table 6.5 refer to the node A (Figure 6. 6).

	Model	E $N/\mu m$	σ_{ef} $N/\mu m^2$	ε_{ef}	δ μm
FEM	M1	2.6×10^{-8}	$2{,}17\times10^{-7}$	4,05	27,29
	M2	$3{,}7143\times10^{-8}$	$5{,}76\times10^{-8}$	1,30	9,95
	M3	$3{,}7143\times10^{-8}$	$5{,}15\times10^{-8}$	1,16	9,23
	M4	$3{,}7143\times10^{-8}$	$6{,}97\times10^{-8}$	1,58	15,90
	M5	$3{,}7143\times10^{-8}$	$1{,}42\times10^{-7}$	3,22	23,37
RPIM	M1	2.6×10^{-8}	$2{,}87\times10^{-7}$	5,58	32,70
	M2	$3{,}7143\times10^{-8}$	$6{,}03\times10^{-8}$	1,36	10,92
	M3	$3{,}7143\times10^{-8}$	$5{,}54\times10^{-8}$	1,26	10,13
	M4	$3{,}7143\times10^{-8}$	$7{,}41\times10^{-8}$	1,70	17,44
	M5	$3{,}7143\times10^{-8}$	$1{,}53\times10^{-7}$	3,49	25,58
NNRPIM	M1	2.6×10^{-8}	$2{,}93\times10^{-7}$	5,05	29,85
	M2	$3{,}7143\times10^{-8}$	$4{,}77\times10^{-8}$	1,12	10,05
	M3	$3{,}7143\times10^{-8}$	$5{,}12\times10^{-8}$	1,17	9,30
	M4	$3{,}7143\times10^{-8}$	$6{,}64\times10^{-8}$	1,54	16,01
	M5	$3{,}7143\times10^{-8}$	$1{,}40\times10^{-7}$	3,18	23,61

Table 6. 4 - The effective stress of Von Mises, equivalent effective strain, and displacement predicted by the simulation for sickle cell anemia at the node considered, for different numerical methods applied and the boundary conditions present in figure 6.3.

σ_{ef}

$N/\mu m^2$

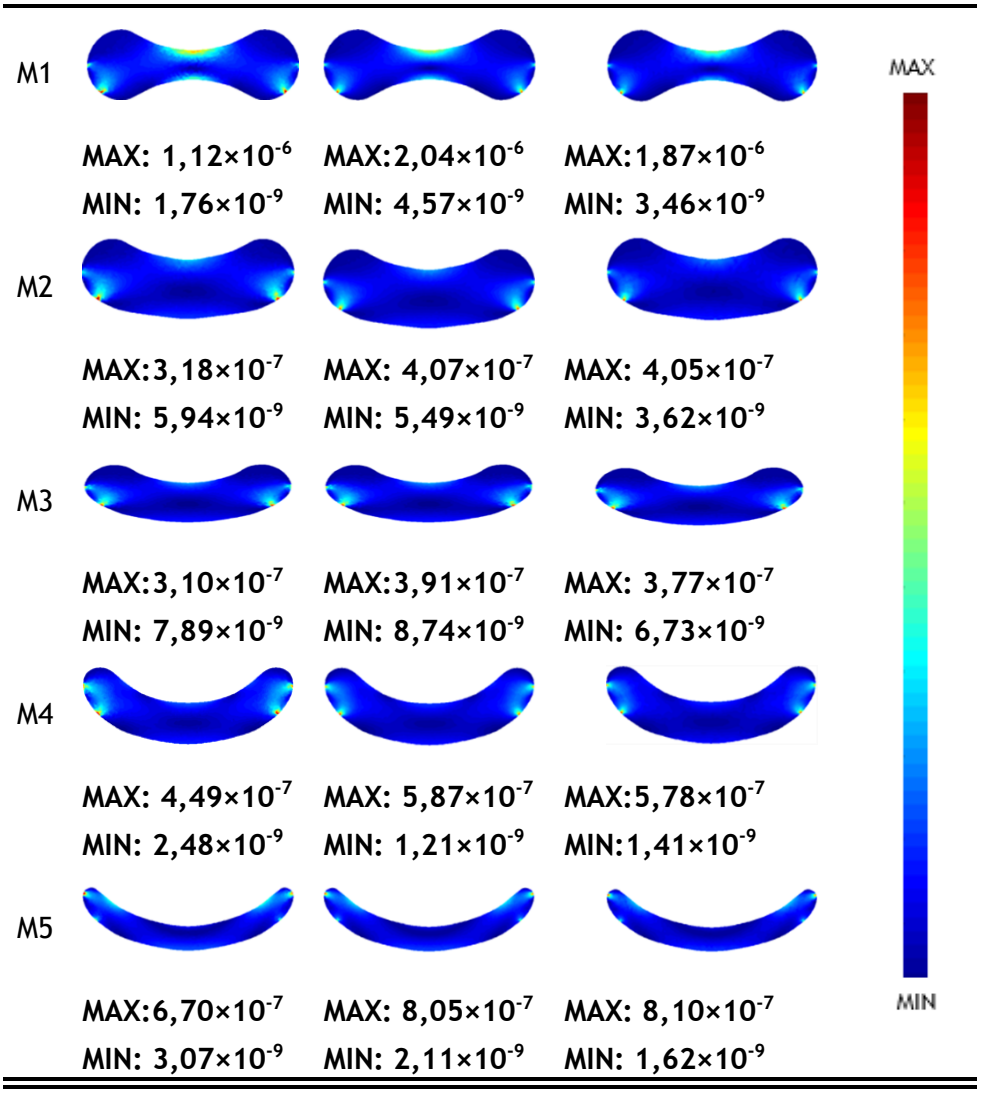

Figure 6. 13 - The effective stress of Von Mises that was predicted by the simulation for the five models applying the numerical methods FEM, RPIM and NNRPIM and the boundary conditions present in figure 6.3. For models M2, M3,M4 and M5 it was consided the Young's modulus of sickle cell anemia ($3{,}7143\times10^{-8}$ N/μm)

ε_{ef}

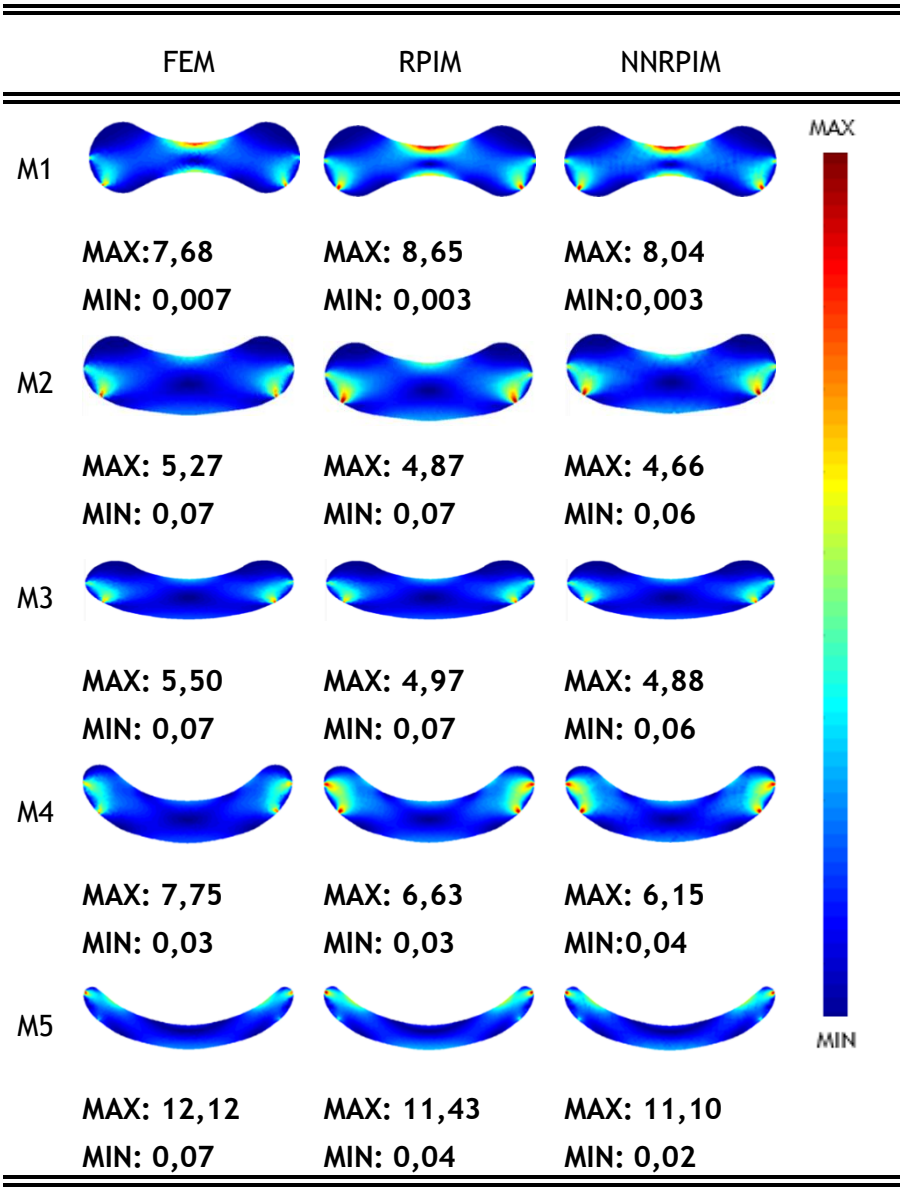

Figure 6. 14 - The equivalent effective strain that was predicted by the simulation for the five models applying the numerical methods FEM, RPIM and NNRPIM and NNRPIM and the boundary conditions present in figure 6.3. For models M2, M3,M4 and M5 it was consided the Young's modulus of sickle cell anemia ($3{,}7143\times10^{-8}$ N/μm).

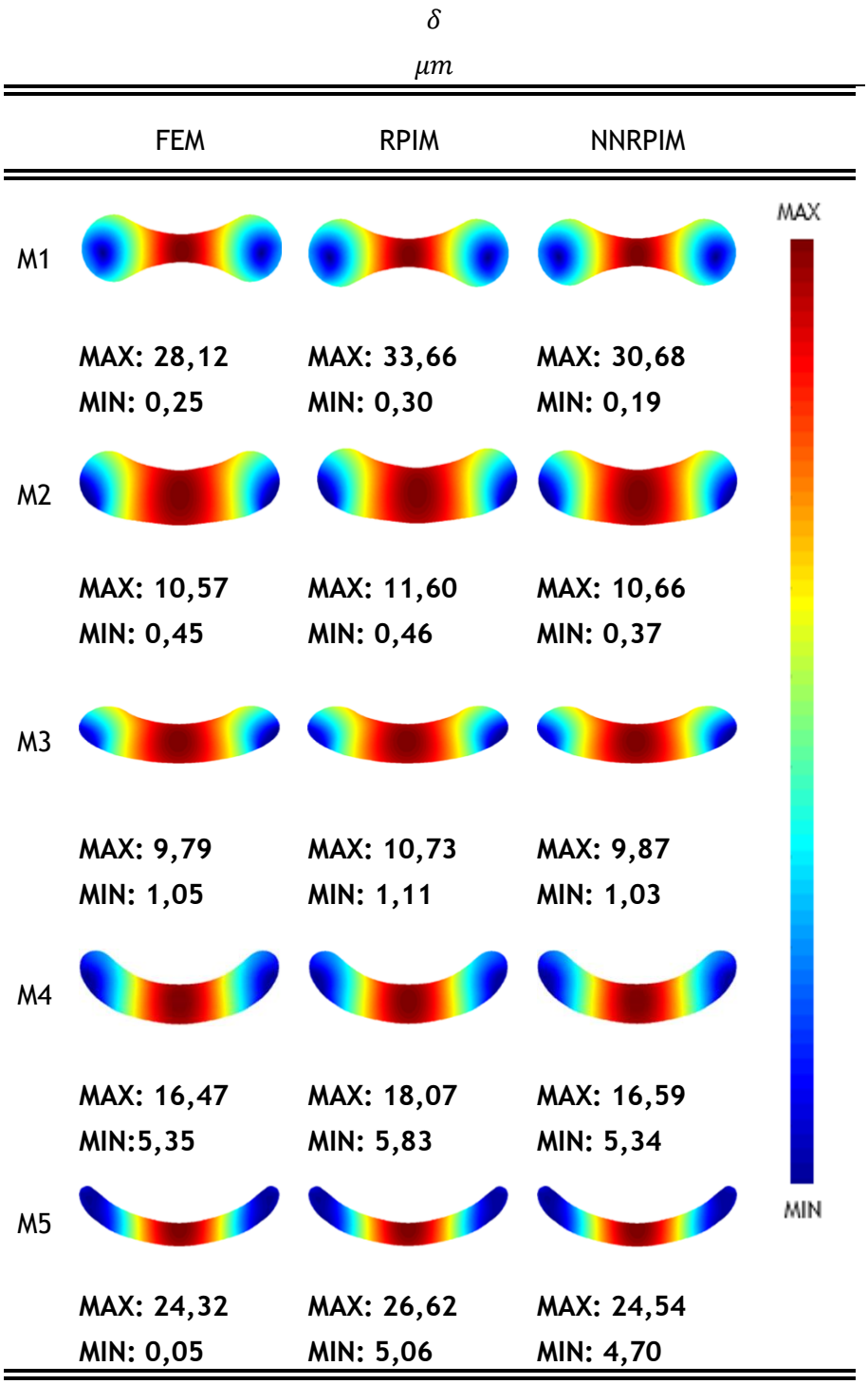

Figure 6.15 - The displacement that that was predicted by the simulation for the five models applying the numerical methods FEM, RPIM and NNRPIM and NNRPIM and the boundary conditions present in figure 6.3. For models M2, M3,M4 and M5 it was consided the Young's modulus of sickle cell anemia ($3{,}7143\times10^{-8}$ N/μm).

	Model	E $N/\mu m$	σ_{ef} $N/\mu m^2$	ε_{ef}	δ μm
FEM	M1	$2{,}6\times10^{-8}$	$2{,}17\times10^{-7}$	4,05	27,29
	M2	$8{,}423\times10^{-8}$	$1{,}03\times10^{-7}$	0,91	5,63
	M3	$8{,}423\times10^{-8}$	$2{,}74\times10^{-8}$	0,23	4,12
	M4	$8{,}423\times10^{-8}$	$9{,}53\times10^{-9}$	0,08	3,63
	M5	$8{,}423\times10^{-8}$	$1{,}09\times10^{-8}$	0,11	5,18
RPIM	M1	$2{,}6\times10^{-8}$	$2{,}87\times10^{-7}$	5,58	32,70
	M2	$8{,}423\times10^{-8}$	$2{,}43\times10^{-8}$	0,10	3,46
	M3	$8{,}423\times10^{-8}$	$2{,}51\times10^{-8}$	0,24	4,52
	M4	$8{,}423\times10^{-8}$	$8{,}69\times10^{-9}$	0,09	3,99
	M5	$8{,}423\times10^{-8}$	$1{,}24\times10^{-8}$	0,13	5,72
NNRPIM	M1	$2{,}6\times10^{-8}$	$2{,}93\times10^{-7}$	5,05	29,84
	M2	$8{,}423\times10^{-8}$	$9{,}79\times10^{-8}$	0,96	5,71
	M3	$8{,}423\times10^{-8}$	$2{,}42\times10^{-8}$	0,23	4,16
	M4	$8{,}423\times10^{-8}$	$7{,}9\times10^{-9}$	0,08	3,67
	M5	$8{,}423\times10^{-8}$	$1{,}16\times10^{-8}$	0,12	5,26

Table 6. 5 - The effective stress of Von Mises, equivalent effective strain, and displacement predicted by the simulation for ovalocytosis at the node considered, for different numerical methods applied and the boundary conditions present in figure 6.3.

σ_{ef}
$N/\mu m^2$

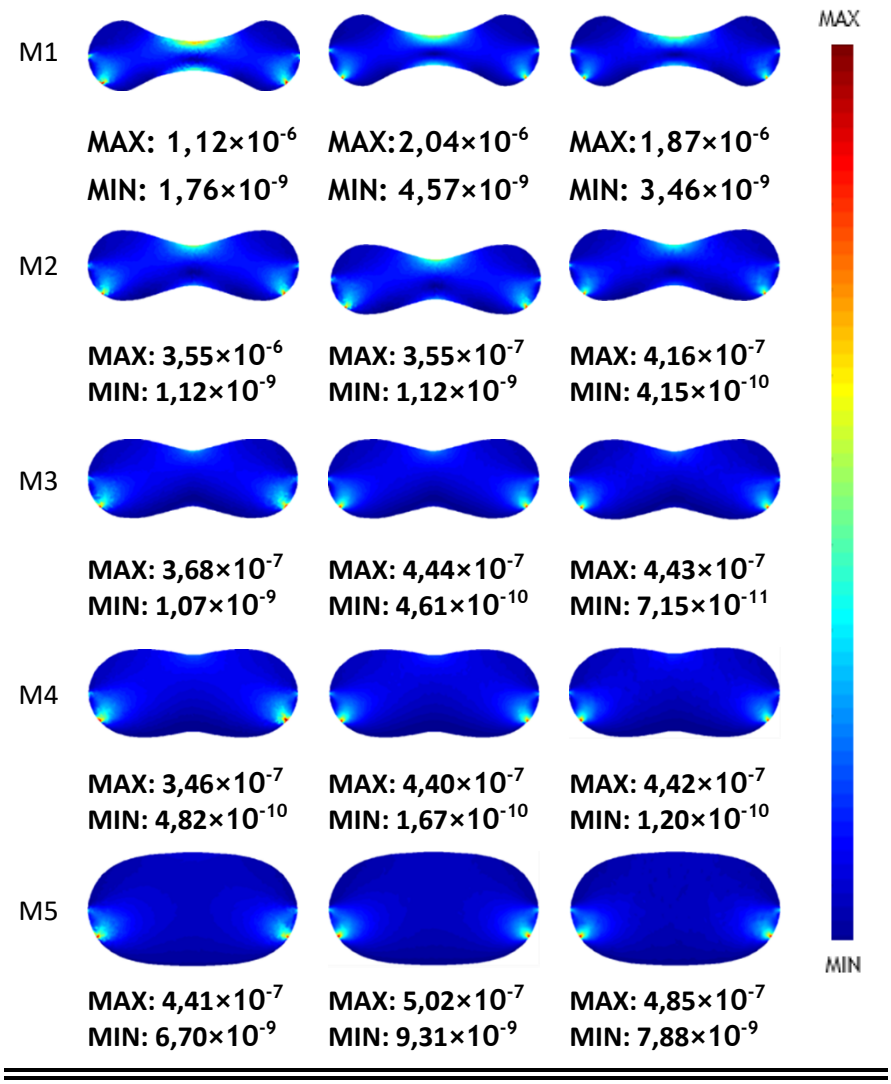

Figure 6. 16 - The effective stress of Von Mises that was predicted by the simulation for the five models applying the numerical methods FEM, RPIM and NNRPIM and NNRPIM and the boundary conditions present in figure 6.3. For models M2, M3,M4 and M5 it was consided the Young's modulus of ovalocytosis ($8{,}423\times10^{-8}$ N/μm).

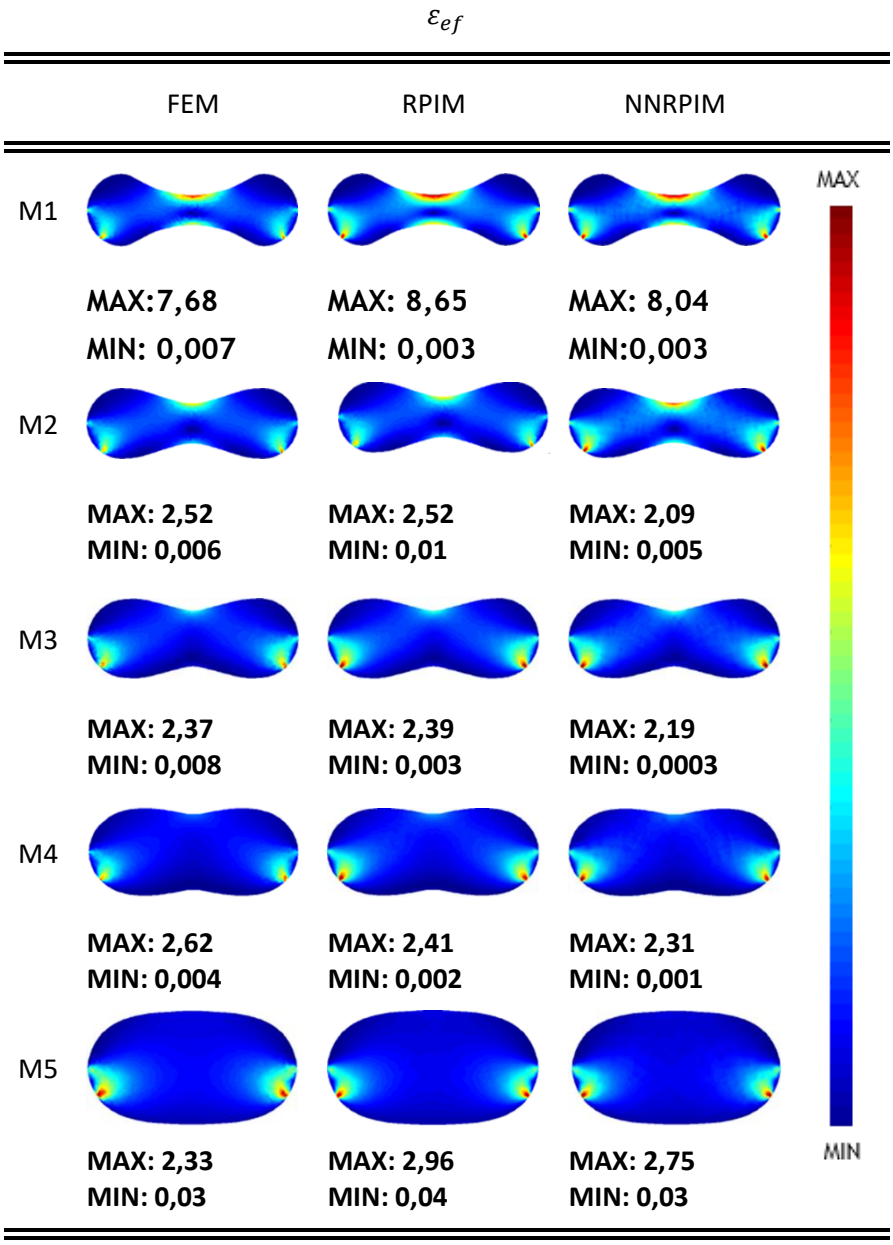

Figure 6. 17 - The equivalent effective strain that was predicted by the simulation for the five models applying the numerical methods FEM, RPIM and NNRPIM and NNRPIM and the boundary conditions present in figure 6.3. For models M2, M3,M4 and M5 it was consided the Young's modulus of ovalocytosis ($8{,}423\times10^{-8}$ N/μm)

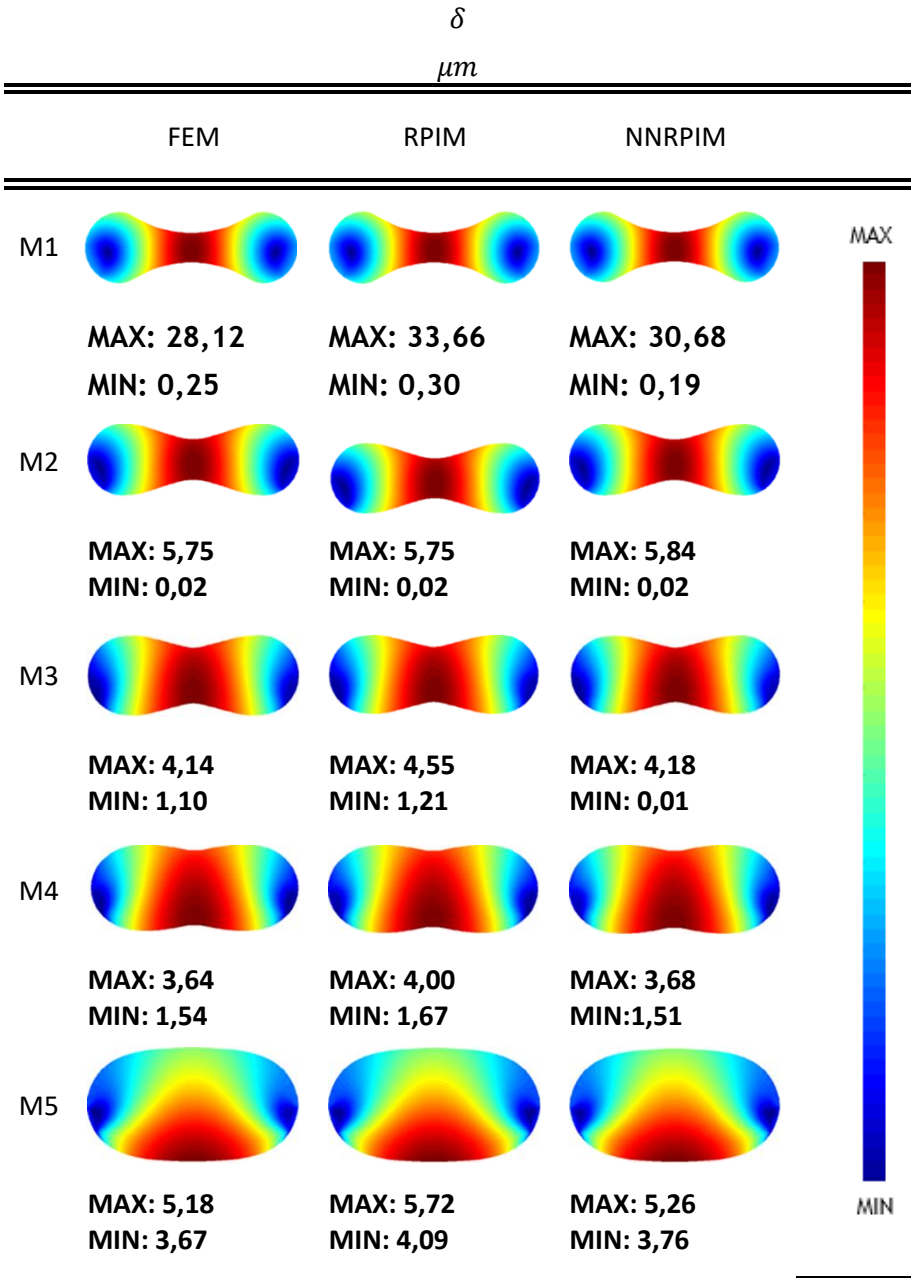

Figure 6.18 - The displacement that that was predicted by the simulation for the five models applying the numerical methods FEM, RPIM and NNRPIM and NNRPIM and the boundary conditions present in figure 6.3. For models M2, M3,M4 and M5 it was consided the Young's modulus of ovalocytosis ($8{,}423\times10^{-8}$ N/μm).

Since real cells are 3D, in order to obtain results closer to reality, it was also studied the effective stress of Von Mises, equivalent effective strain and the displacement for the 3D models in the node A (figure 6.19) for the cells: healthy (H), with sickle cell anemia (SC) and with ovalocytosis (O).

First, as for the 2D models, the influence of the shape change was studied for the variable fields: effective stress of Von Mises, equivalent effective strain and the displacement. The results are shown in table 6.6 and in figures 6.19-6.21.

For healthy cell, it was also studied the influence of application of two different boundary conditions (figure 6.19) (BS-1 and BS-2) for cells with sickle cell anemia and ovalócitose give the boundary conditions given by (SC and OV). The boundary conditions referred to above represent the constraints to which the cells are exposed when forced to pass through a blood vessel with dimensions smaller than the dimensions of the cell itself. The displacement is constrained in a orthogonal direction to the cell surface and a distributed pressure is applied in the top of the cell..

Figure 6.19 - Node considered in the 3D studies.

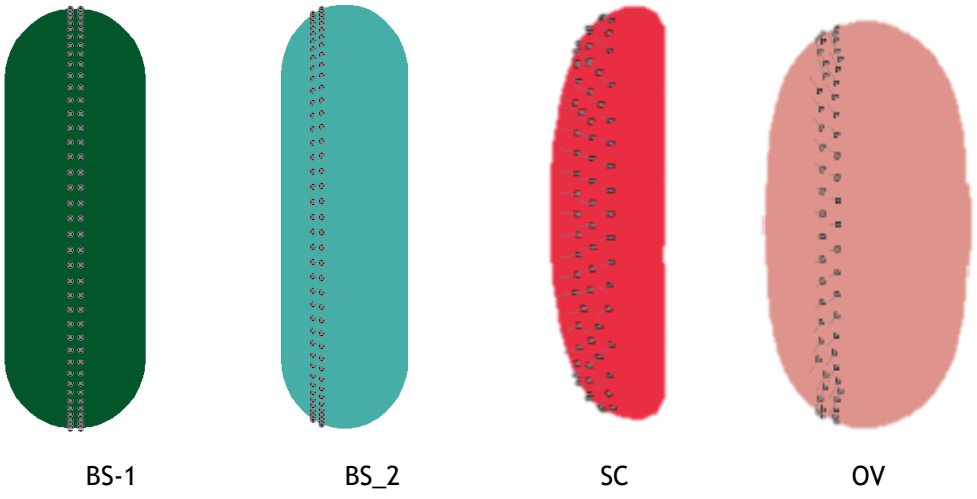

Figure 6.20 - Different boundary conditions

	Model	E $N/\mu m$	σ_{ef} $N/\mu m^2$	ε_{ef}	δ μm
FEM	**H-BS-1**	$2{,}6\times10^{-8}$	$1{,}50\times10^{-9}$	0,06	1,70
	H-BS-2	$2{,}6\times10^{-8}$	$1{,}99\times10^{-8}$	0,75	11,67
	SC	$2{,}6\times10^{-8}$	$2{,}64\times10^{-8}$	0,99	1,01
	O	$2{,}6\times10^{-8}$	$1{,}14\times10^{-8}$	0,43	3,36
RPIM	**H-BS-1**	$2{,}6\times10^{-8}$	$1{,}94\times10^{-9}$	0,07	2,96
	H-BS-2	$2{,}6\times10^{-8}$	$3{,}11\times10^{-8}$	1,17	14,69
	SC	$2{,}6\times10^{-8}$	$2{,}77\times10^{-8}$	1,04	1,16
	O	$2{,}6\times10^{-8}$	$1{,}24\times10^{-8}$	0,47	3,66
NNRPIM	**H-BS-1**	$2{,}6\times10^{-8}$	$1{,}56\times10^{-9}$	0,06	3,13
	H-BS-2	$2{,}6\times10^{-8}$	$3{,}34\times10^{-8}$	1,26	14,69
	SC	$2{,}6\times10^{-8}$	$2{,}79\times10^{-8}$	1,04	1,13
	O	$2{,}6\times10^{-8}$	$1{,}29\times10^{-8}$	0,49	3,63

Table 6. 6 - The effective stress of Von Mises, equivalent effective strain, and displacement predicted by the simulation for the cells healthy, with sickle cell anemia and with ovalocytosis at the node considered and for different numerical methods applied considering E =$2{,}6\times10^{-8}$ N/μm.

σ_{ef}
$N/\mu m^2$

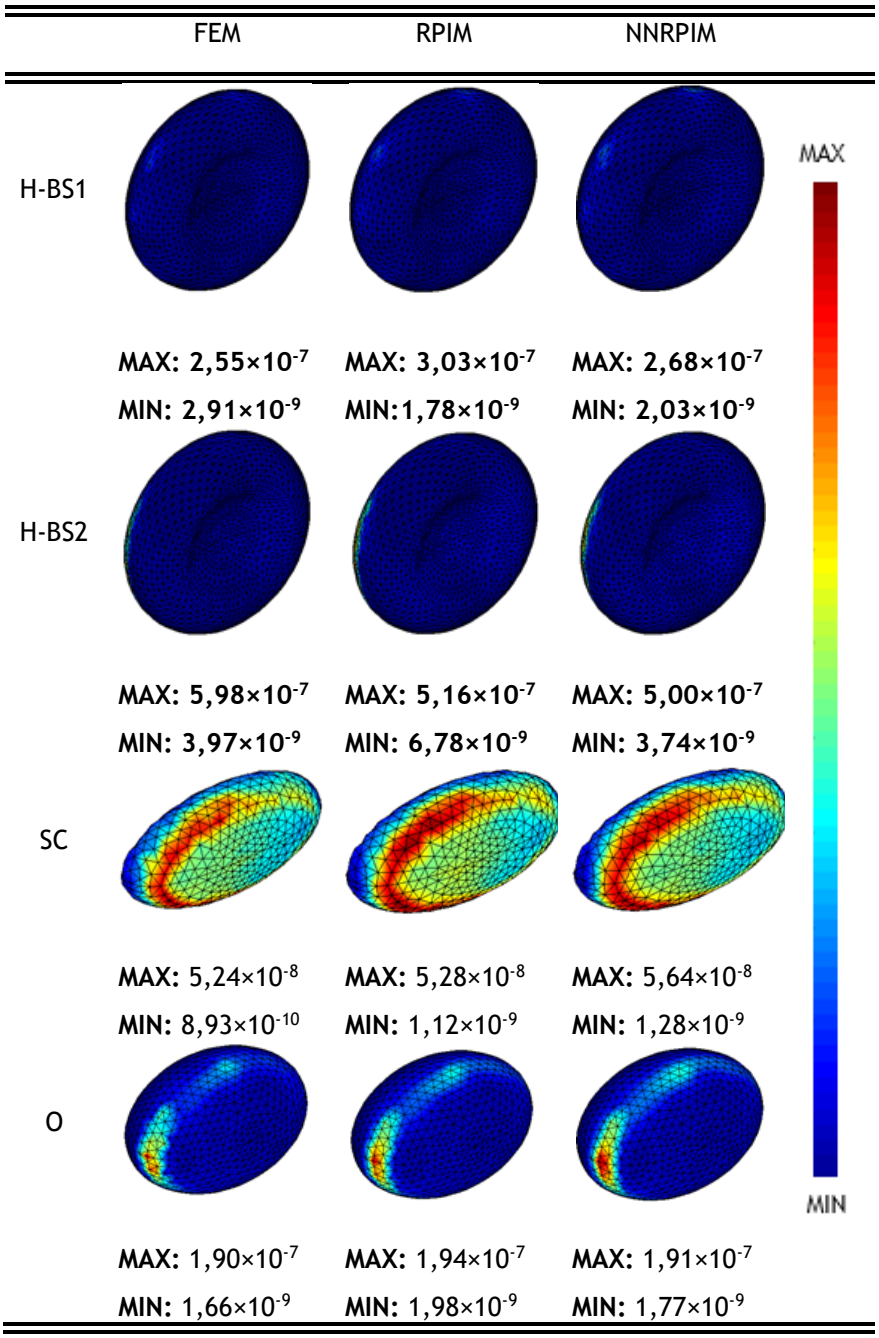

Figure 6. 21 - The effective stress of Von Mises that was predicted by the 3D simulation applying the numerical methods FEM, RPIM and NNRPIM and the boundary conditions present in figure 6.20. It was consided the Young's modulus of all cells are iqual to $2{,}6\times10^{-8}$ N/μm.

ε_{ef}

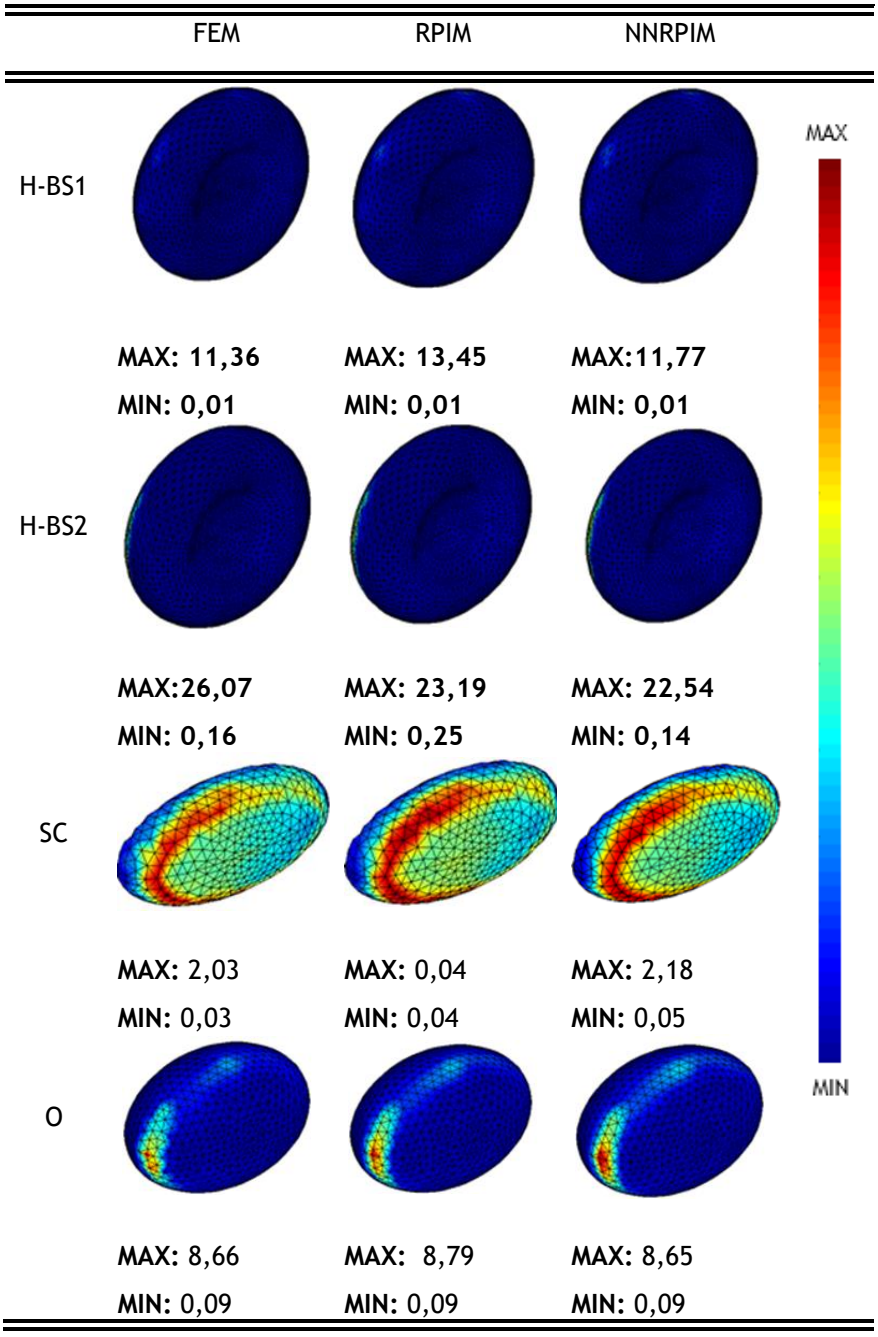

Figure 6.22- The equivalent effective strain that was predicted by the 3D simulation applying the numerical methods FEM, RPIM and NNRPIM and the boundary conditions present in figure 6.20. It was consided the Young's modulus of all cells are iqual to $2{,}6\times10^{-8}$ N/μm.

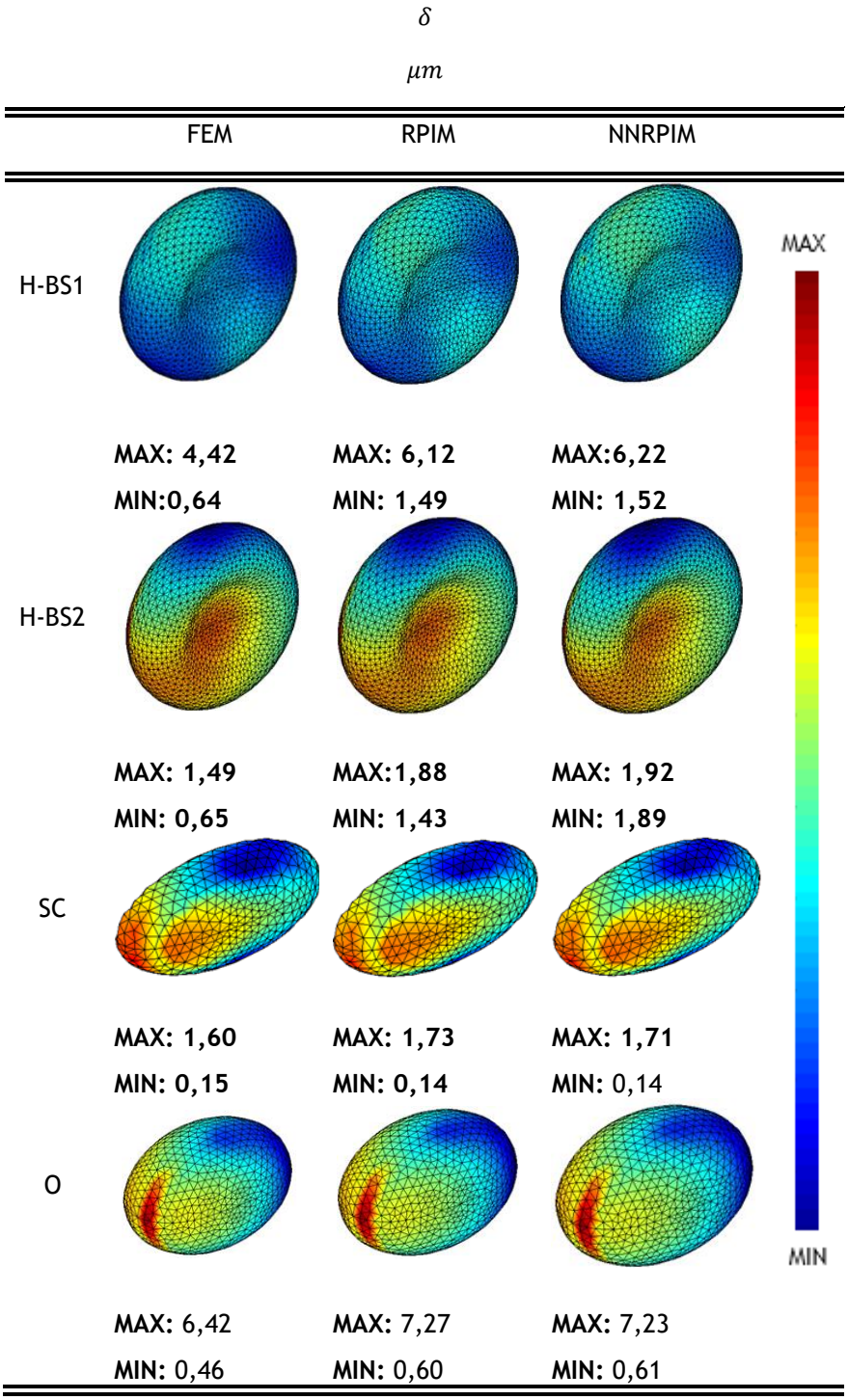

Figure 6.23- The displacement that was predicted by the 3D simulation applying the numerical methods FEM, RPIM and NNRPIM and the boundary conditions present in figure 6.20. It was consided the Young's modulus of all cells are iqual to $2{,}6\times10^{-8}$ N/μm.

Regarding the static 3D studies, the effective tension of von Mises; equivalent effective strain and displacement (considering the different Young's modulus) are presented in (Table 6. 1) for each cell.

This analysis allowed to assess the behavior of healthy and pathological cells in the bloodstream. The results obtained are present in table 6.7 and figure 6.24-6.26.

	Model	E $N/\mu m$	σ_{ef} $N/\mu m^2$	ε_{ef}	δ μm
FEM	**H-BS-1**	$2{,}6\times10^{-8}$	$1{,}50\times10^{-9}$	0,06	1,70
	H-BS-2	$2{,}6\times10^{-8}$	$1{,}99\times10^{-8}$	0,75	11,67
	SC	$3{,}7143\times10^{-8}$	$2{,}64\times10^{-8}$	0,69	0,70
	O	$8{,}423\times10^{-8}$	$1{,}14\times10^{-8}$	0,13	1,04
RPIM	**H-BS-1**	$2{,}6\times10^{-8}$	$1{,}94\times10^{-9}$	0,07	2,96
	H-BS-2	$2{,}6\times10^{-8}$	$3{,}11\times10^{-8}$	1,17	14,69
	SC	$3{,}7143\times10^{-8}$	$2{,}77\times10^{-8}$	0,72	0,81
	O	$8{,}423\times10^{-8}$	$1{,}24\times10^{-8}$	0,15	1,13
NNRPIM	**H-BS-1**	$2{,}6\times10^{-8}$	$1{,}56\times10^{-9}$	0,06	3,13
	H-BS-2	$2{,}6\times10^{-8}$	$3{,}34\times10^{-8}$	1,26	14,69
	SC	$3{,}7143\times10^{-8}$	$2{,}79\times10^{-8}$	0,73	0,79
	O	$8{,}423\times10^{-8}$	$1{,}29\times10^{-8}$	0,15	1,12

Table 6.7 - The effective stress of Von Mises, equivalent effective strain, and displacement predicted by the simulation for the cells healthy, with sickle cell anemia and with ovalocytosis at the node considered and for different numerical methods applied.

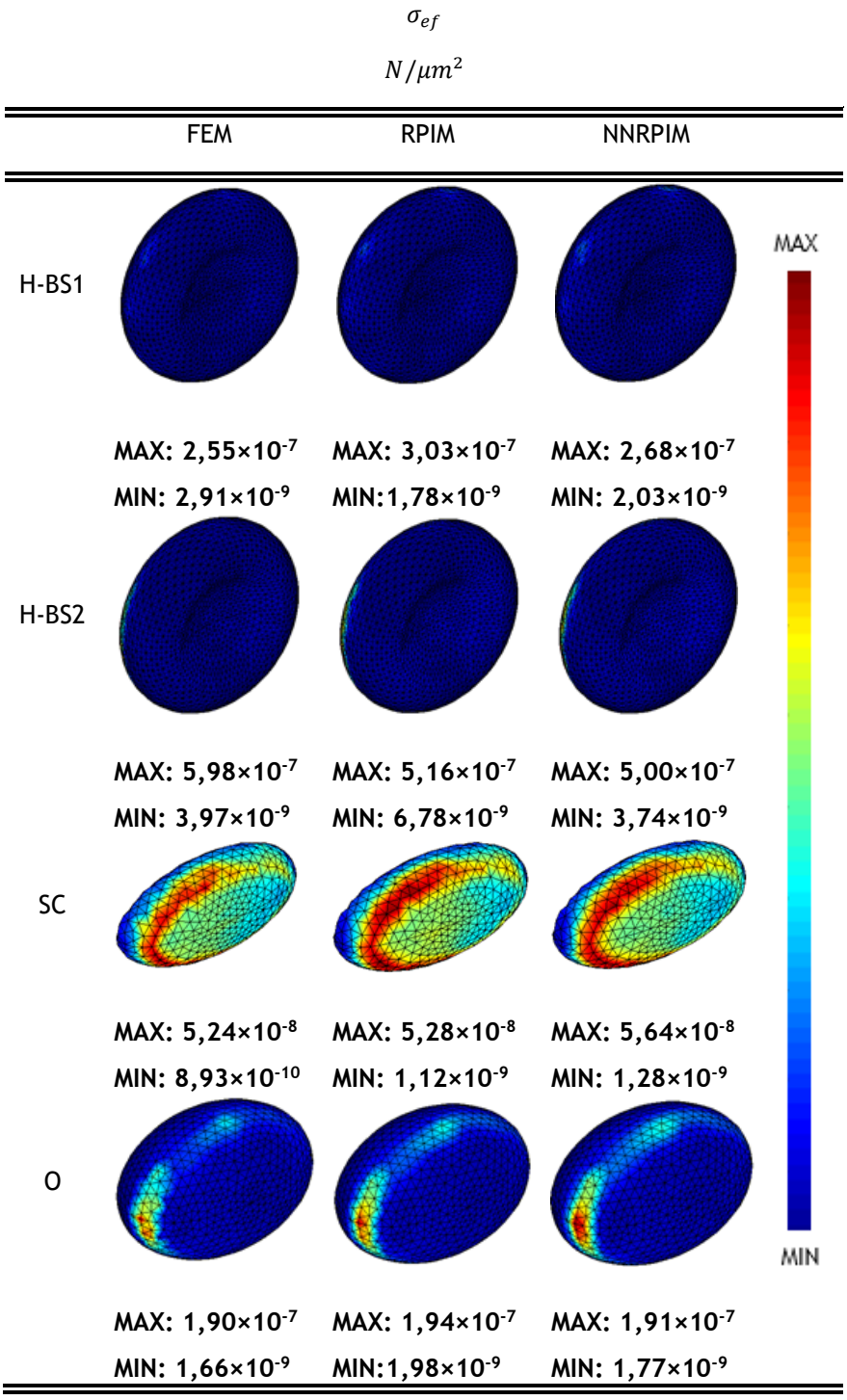

Figure 6. 24 - The effective stress of Von Mises that was predicted by the 3D simulation applying the numerical methods FEM, RPIM and NNRPIM and the boundary conditions present in figure 6.20.

ε_{ef}

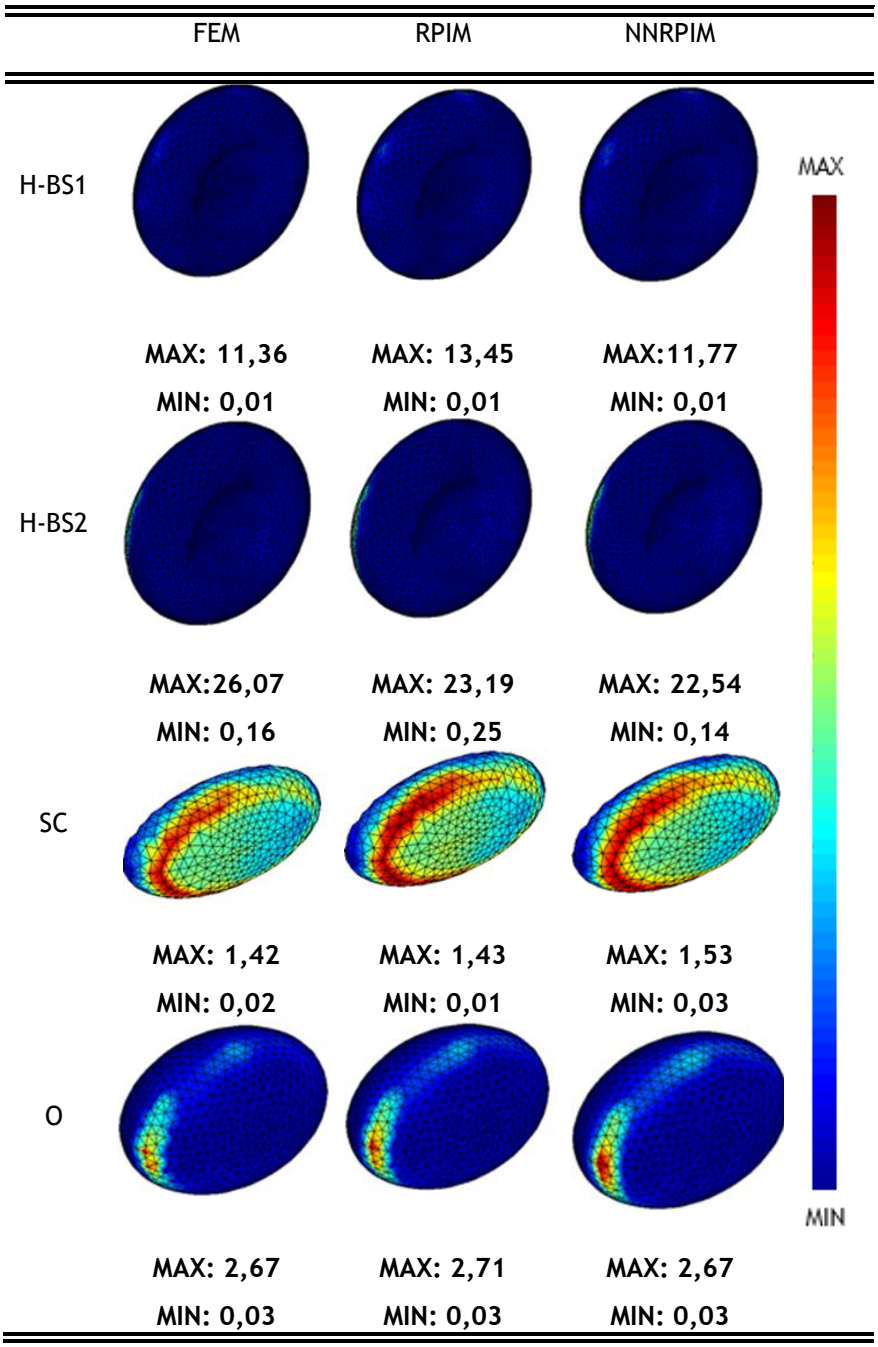

Figure 6. 25 - The equivalent effective strain that was predicted by the 3D simulation applying the numerical methods FEM, RPIM and NNRPIM and the boundary conditions present in figure 6.20.

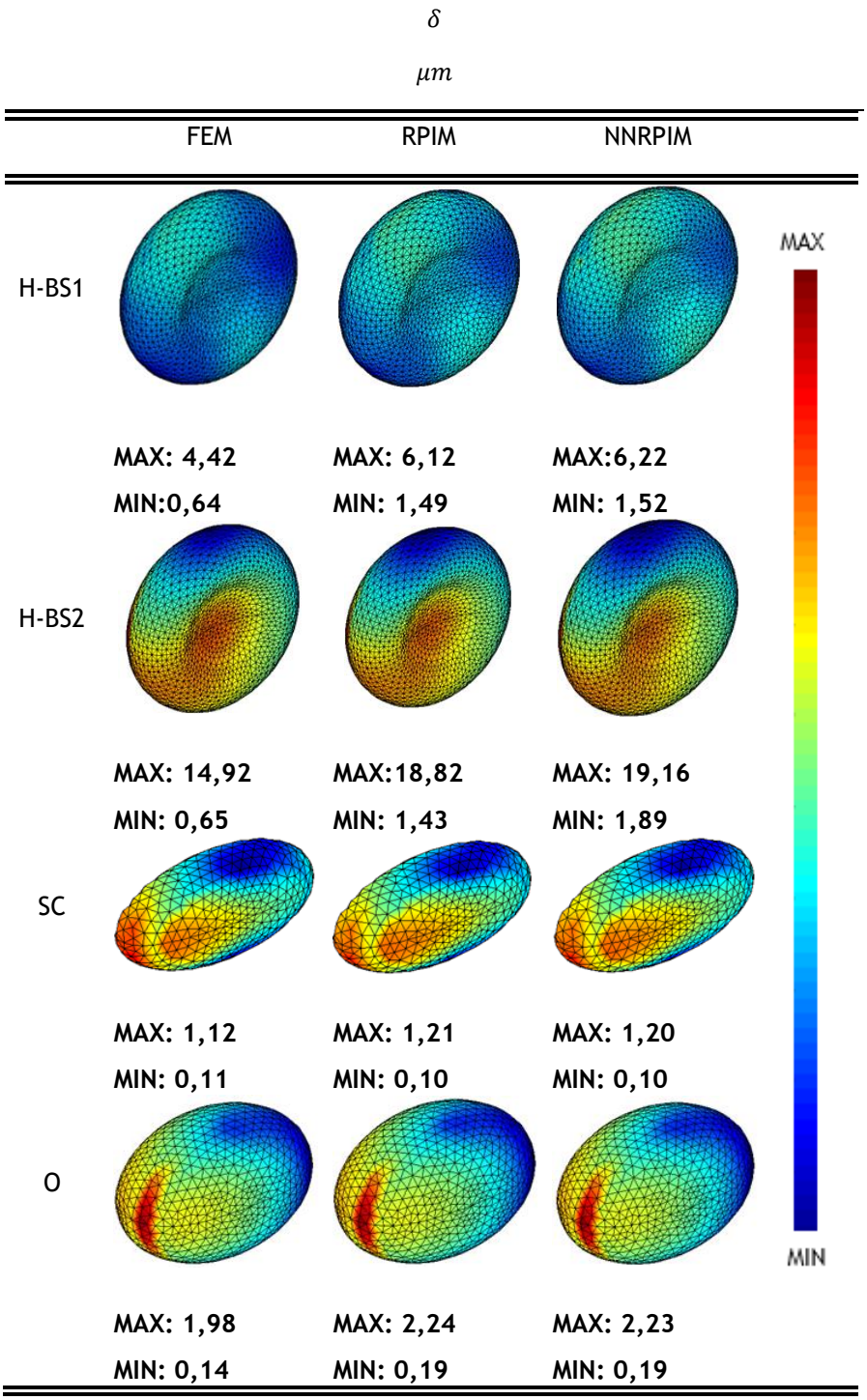

Figure 6.26 - The displacement that was predicted by the 3D simulation applying the numerical methods FEM, RPIM and NNRPIM and the boundary conditions present in figure 6.20.

Chapter 7

Red blood cells – free vibrations

7.1 - Dynamic studies

In the previous chapter, static studies were carried out, namely convergence studies. In this chapter, the 2D and 3D models of healthy and pathological cells will be used to determine their free vibration modes. The objective of this stage of the work is the determination of the first three modes of vibration for the different cellular forms. In order to achieve the aimed results, the cells were placed to vibrate freely (no degree of freedom was constrained).

The 2D results for sickle cell anemia are present in Figure 7.1-7.9, while results for ovalocytosis are present in Figure 7.10- 7.18. The 3D results are shown in Table 7.3 and Figure 7.19- 7.27.

	Model	E $N/\mu m$	$\hat{\omega}_1$	$\hat{\omega}_2$ ×10^4	$\hat{\omega}_3$
FEM	**M1**	2.6×10^{-8}	2,23	6,09	6,49
	M2	$3{,}7143\times10^{-8}$	4,19	9,03	9,38
	M3	$3{,}7143\times10^{-8}$	4,01	8,64	9,60
	M4	$3{,}7143\times10^{-8}$	2,69	6,45	9,54
	M5	$3{,}7143\times10^{-8}$	1,66	4,41	7,95
RPIM	**M1**	2.6×10^{-8}	2,06	6,43	6,01
	M2	$3{,}7143\times10^{-8}$	4,19	9,01	9,37
	M3	$3{,}7143\times10^{-8}$	4,00	8,62	9,59
	M4	$3{,}7143\times10^{-8}$	2,68	6,43	9,53
	M5	$3{,}7143\times10^{-8}$	1,65	4,40	7,92
NNRPIM	**M1**	2.6×10^{-8}	2,04	5,99	6,43
	M2	$3{,}7143\times10^{-8}$	4,18	9,02	9,39
	M3	$3{,}7143\times10^{-8}$	3,99	8,62	9,59
	M4	$3{,}7143\times10^{-8}$	2,67	6,41	9,53
	M5	$3{,}7143\times10^{-8}$	1,64	4,37	7,89

Table 7. 1 - The 1st ($\hat{\omega}_1$) , 2nd ($\hat{\omega}_2$) and 3rd ($\hat{\omega}_3$) free vibration modes for FEM, RPIM and NNRPIM numerical methods and to the 2D sickle cell anemia model.

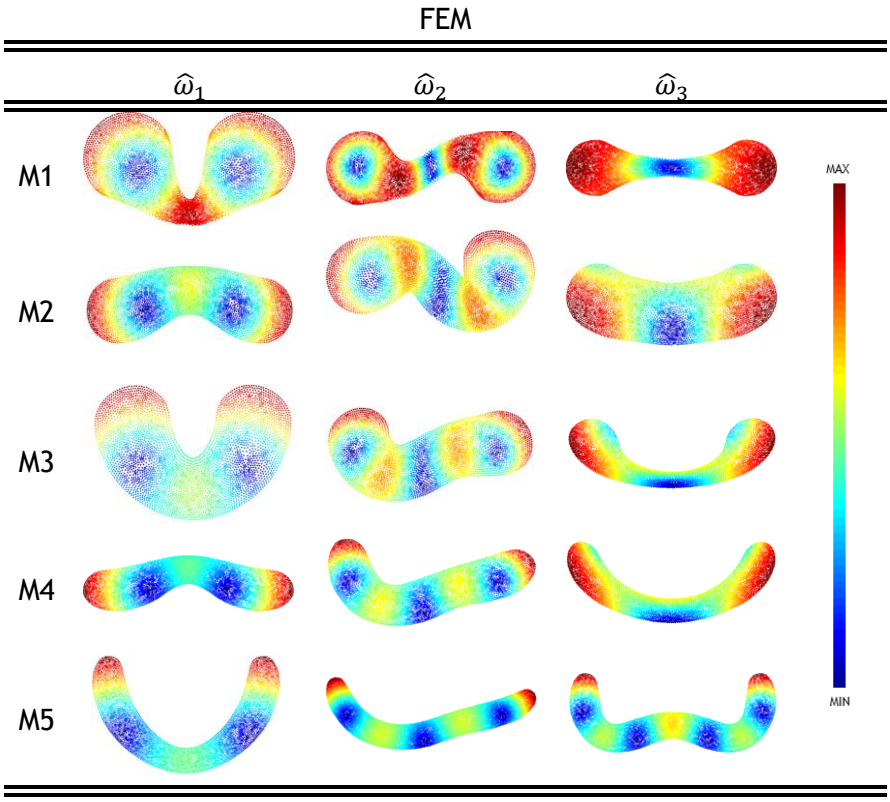

Figure 7. 1 - The 1st $(\widehat{\omega}_1)$, 2nd $(\widehat{\omega}_2)$ and 3rd $(\widehat{\omega}_3)$ free vibration modes for numerical method FEM and to the 2D sickle cell anemia model.

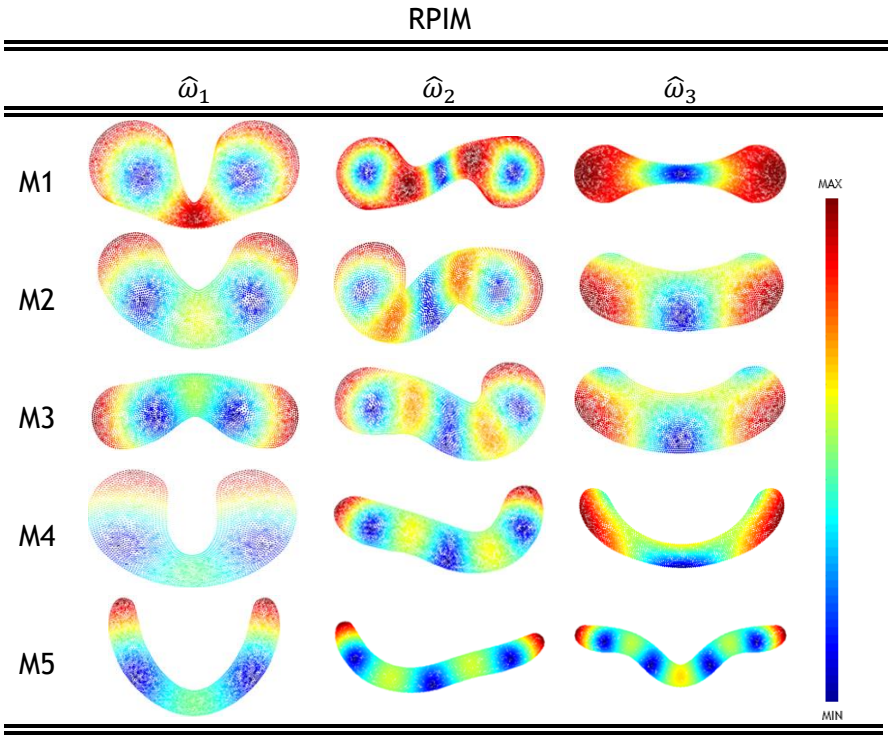

Figure 7. 2 - 1st $(\widehat{\omega}_1)$, 2nd $(\widehat{\omega}_2)$ and 3rd $(\widehat{\omega}_3)$ free vibration modes for numerical method RPIM and to the 2D sickle cell anemia model.

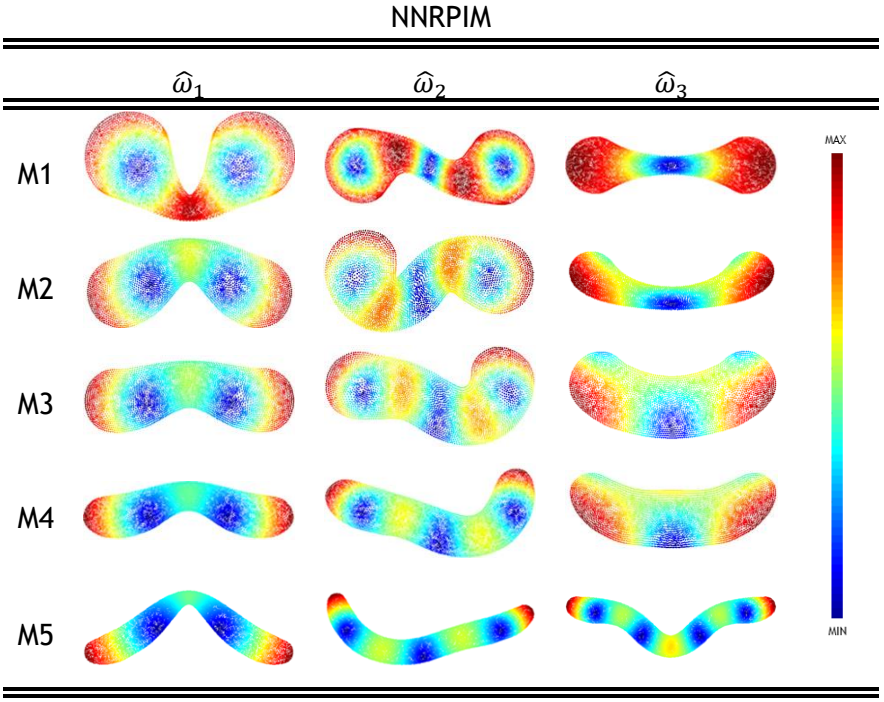

Figure 7. 3 - The 1st $(\widehat{\omega}_1)$, 2nd $(\widehat{\omega}_2)$ and 3rd $(\widehat{\omega}_3)$ free vibration modes for numerical method NNRPIM and to the 2D sickle cell anemia model.

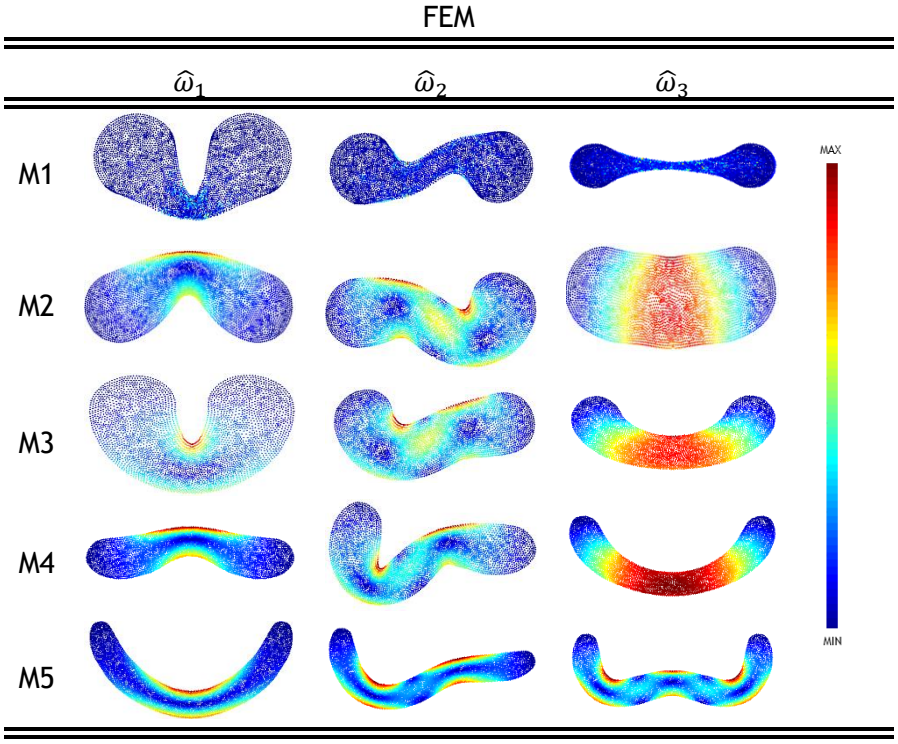

Figure 7. 4 - The potential field of the effective stress of Von Mises 1st $(\widehat{\omega}_1)$, 2nd $(\widehat{\omega}_2)$ and 3rd $(\widehat{\omega}_3)$ free vibration modes for numerical method FEM and to the 2D sickle cell anemia model.

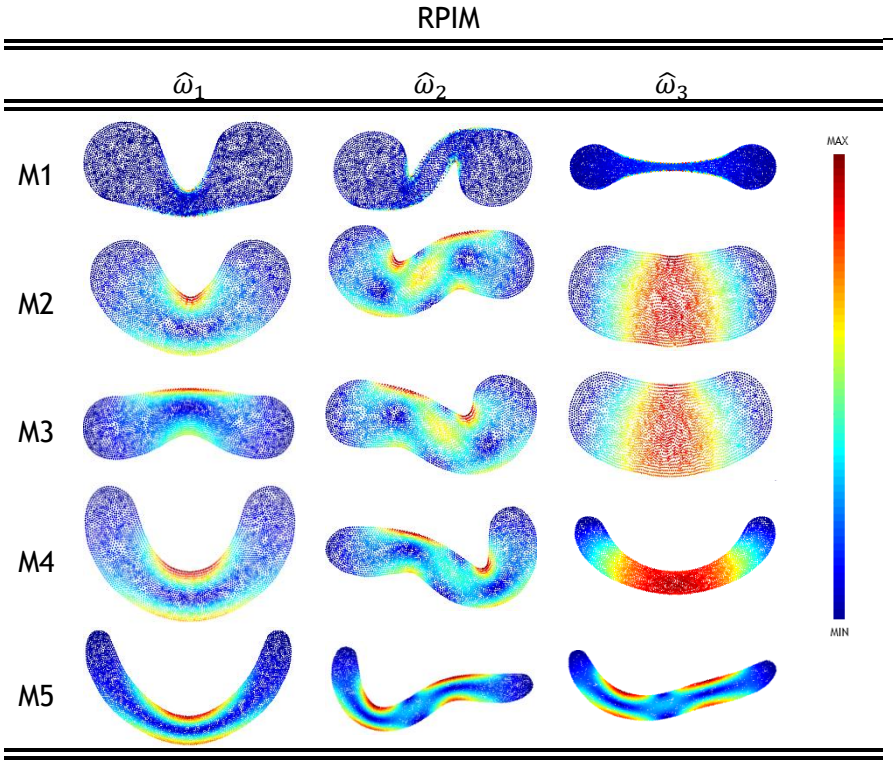

Figure 7. 5 - The potential field of the effective stress of Von Mises of 1st ($\widehat{\boldsymbol{\omega}}_1$) , 2nd ($\widehat{\boldsymbol{\omega}}_2$) and 3rd ($\widehat{\boldsymbol{\omega}}_3$) free vibration modes for numerical method RPIM and to the 2D sickle cell anemia model.

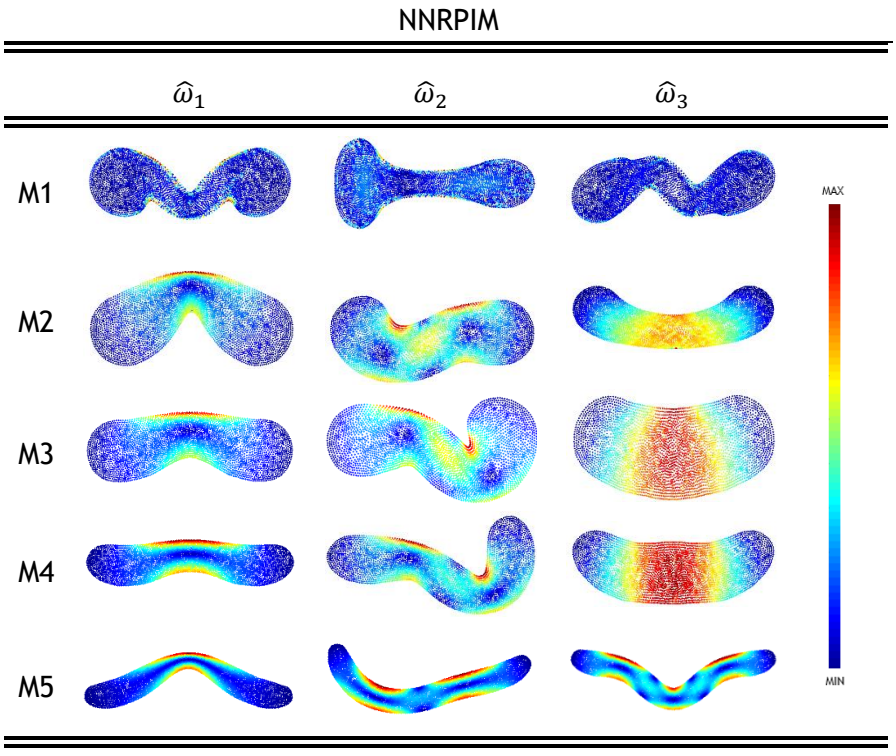

Figure 7. 6 - The potential field of the effective stress of Von Mises of 1st ($\widehat{\boldsymbol{\omega}}_1$) , 2nd ($\widehat{\boldsymbol{\omega}}_2$) and 3rd ($\widehat{\boldsymbol{\omega}}_3$) free vibration modes for numerical method NNRPIM and to the 2D sickle cell anemia model.

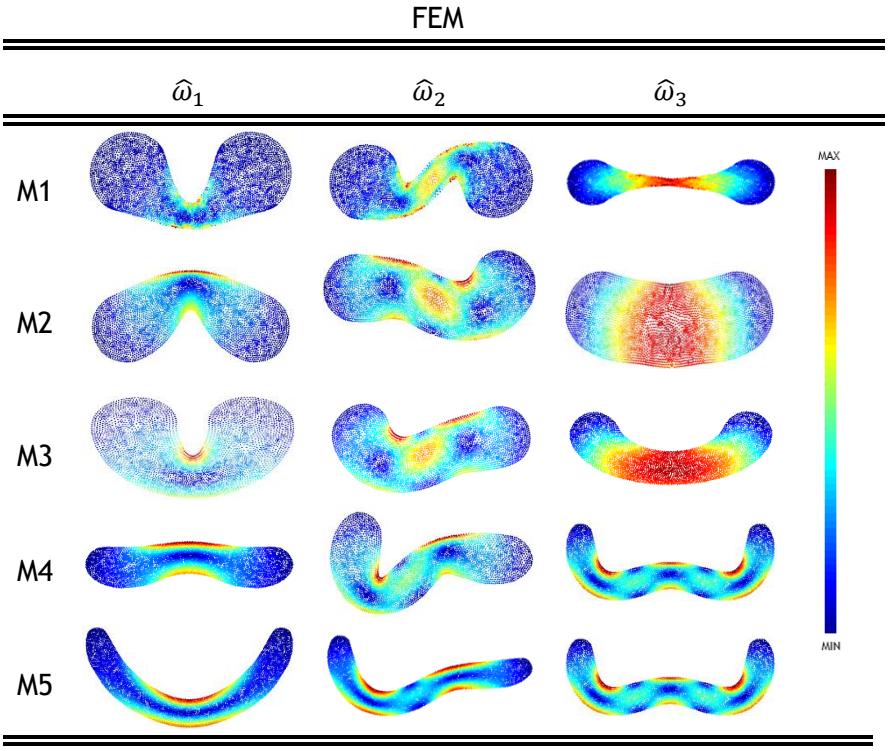

Figure 7. 7 - The potential field of the effective strain of 1st ($\widehat{\boldsymbol{\omega}}_{\mathbf{1}}$) , 2nd ($\widehat{\boldsymbol{\omega}}_{\mathbf{2}}$) and 3rd ($\widehat{\boldsymbol{\omega}}_{\mathbf{3}}$) free vibration modes for numerical method FEM and to the 2D sickle cell anemia model.

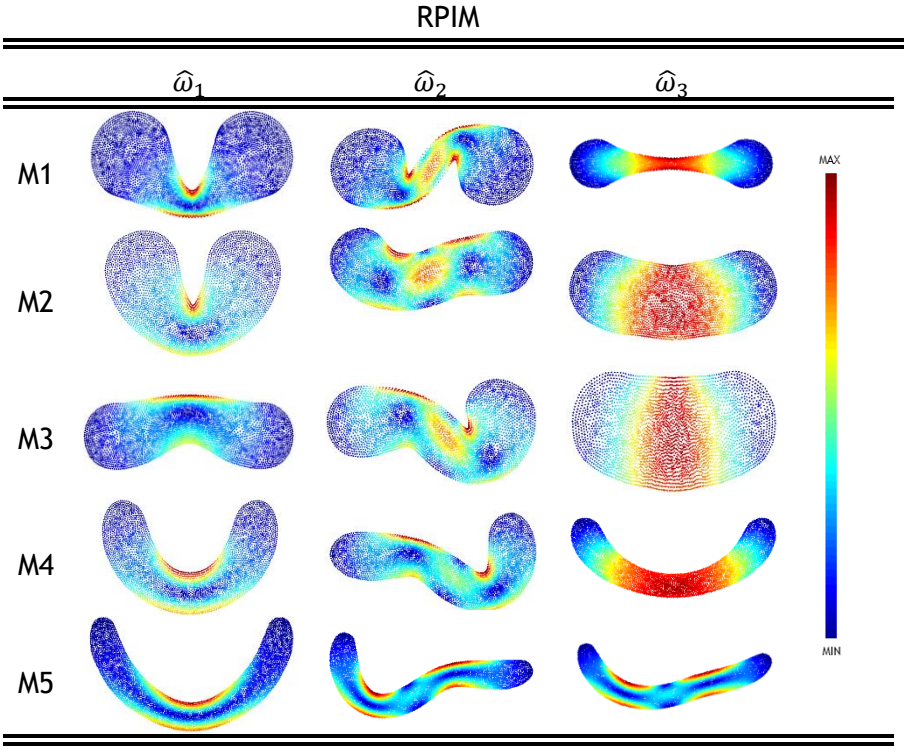

Figure 7. 8 - The potential field of the effective strain of 1st ($\widehat{\boldsymbol{\omega}}_{\mathbf{1}}$) , 2nd ($\widehat{\boldsymbol{\omega}}_{\mathbf{2}}$) and 3rd ($\widehat{\boldsymbol{\omega}}_{\mathbf{3}}$) free vibration modes for numerical method RPIM and to the 2D sickle cell anemia model.

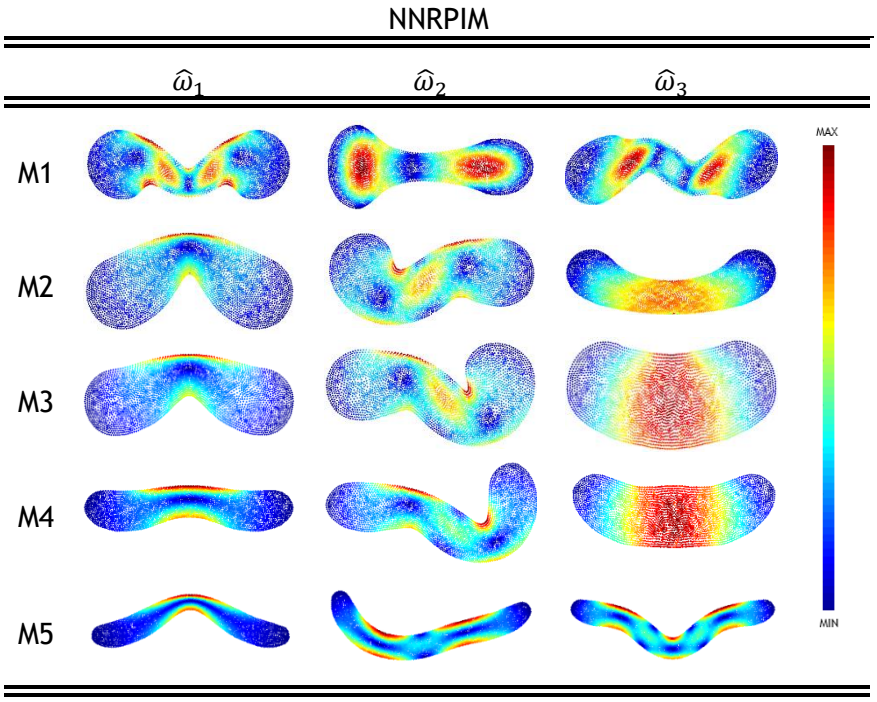

Figure 7. 9 - The potential field of the effective strain of 1st $(\widehat{\boldsymbol{\omega}}_{\mathbf{1}})$, 2nd $(\widehat{\boldsymbol{\omega}}_{\mathbf{2}})$ and 3rd $(\widehat{\boldsymbol{\omega}}_{\mathbf{3}})$ free vibration modes for numerical method NNRPIM and to the 2D sickle cell anemia model.

	Model	E $N/\mu m$	$\widehat{\omega}_1$	$\widehat{\omega}_2$ ×10^4	$\widehat{\omega}_3$
FEM	**M1**	2.6×10^{-8}	2,23	6,09	6,49
	M2	$8{,}423\times10^{-8}$	4,95	1,24	1,30
	M3	$8{,}423\times10^{-8}$	6,54	1,31	1,45
	M4	$8{,}423\times10^{-8}$	8,42	1,37	1,55
	M5	$8{,}423\times10^{-8}$	10,81	13,54	1,45
RPIM	**M1**	2.6×10^{-8}	2,06	6,43	6,01
	M2	$8{,}423\times10^{-8}$	4,93	1,24	1,30
	M3	$8{,}423\times10^{-8}$	6,52	1,31	1,45
	M4	$8{,}423\times10^{-8}$	8,41	1,37	1,54
	M5	$8{,}423\times10^{-8}$	10,80	13,53	1,45
NNRPIM	**M1**	2.6×10^{-8}	2,04	5,99	6,43
	M2	$8{,}423\times10^{-8}$	4,91	1,24	130
	M3	$8{,}423\times10^{-8}$	6,50	1,31	1,45
	M4	$8{,}423\times10^{-8}$	8,38	1,38	1,54
	M5	$8{,}423\times10^{-8}$	10,78	13,62	14,65

Table 7. 2 - The 1st ($\widehat{\omega}_1$) , 2nd ($\widehat{\omega}_2$) and 3rd ($\widehat{\omega}_3$) free vibration modes for FEM, RPIM and NNRPIM numerical methods and to the 2D ovalocytosis model.

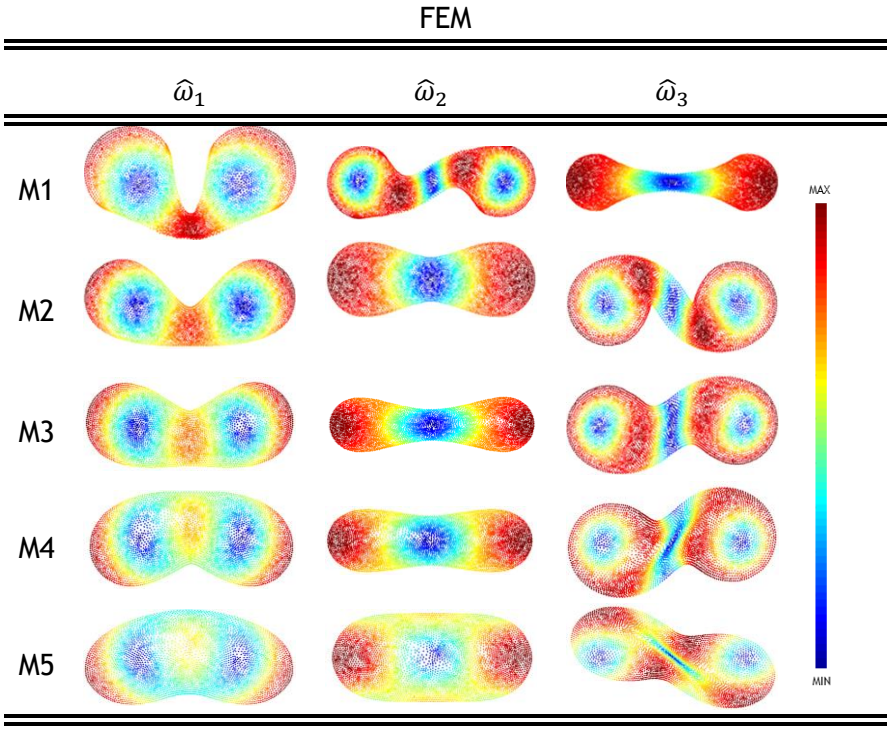

Figure 7. 10 - The 1st ($\hat{\omega}_1$) , 2nd ($\hat{\omega}_2$) and 3rd ($\hat{\omega}_3$) free vibration modes for numerical method FEM and to the 2D ovalocytosis model.

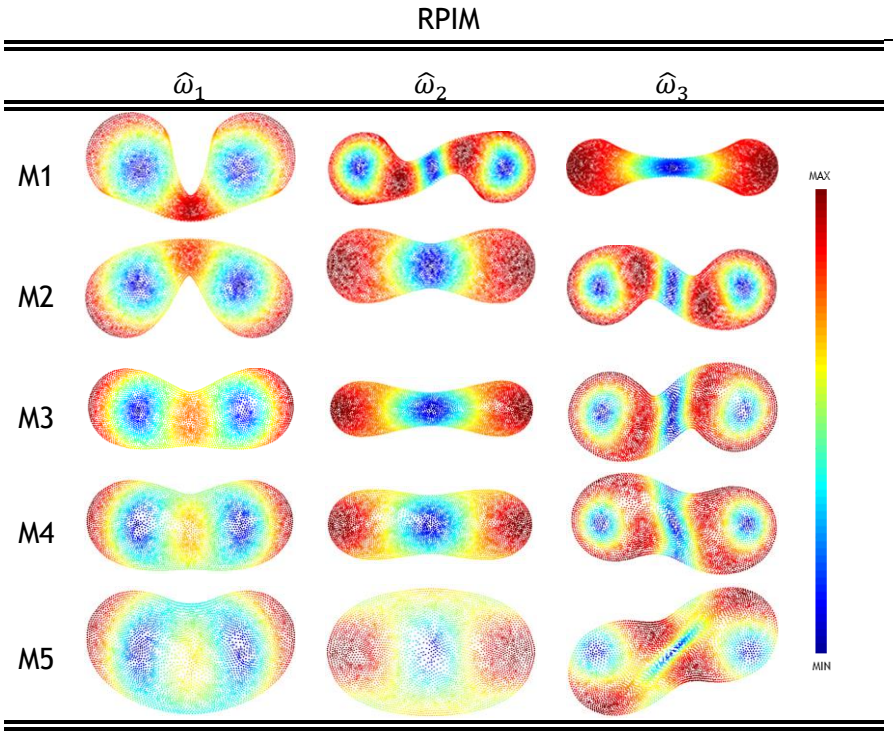

Figure 7. 11 - The 1st ($\hat{\omega}_1$) , 2nd ($\hat{\omega}_2$) and 3rd ($\hat{\omega}_3$) free vibration modes for numerical method RPIM and to the 2D ovalocytosis model.

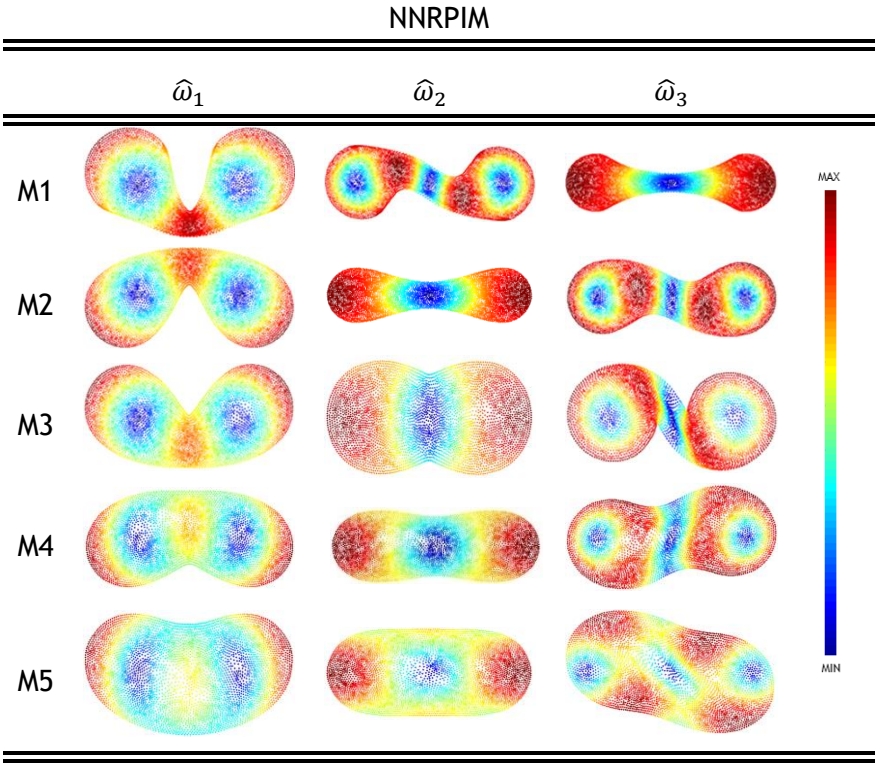

Figure 7. 12 - The 1st ($\widehat{\omega}_1$) , 2nd ($\widehat{\omega}_2$) and 3rd ($\widehat{\omega}_3$) free vibration modes for numerical method NNRPIM and to the 2D ovalocytosis model.

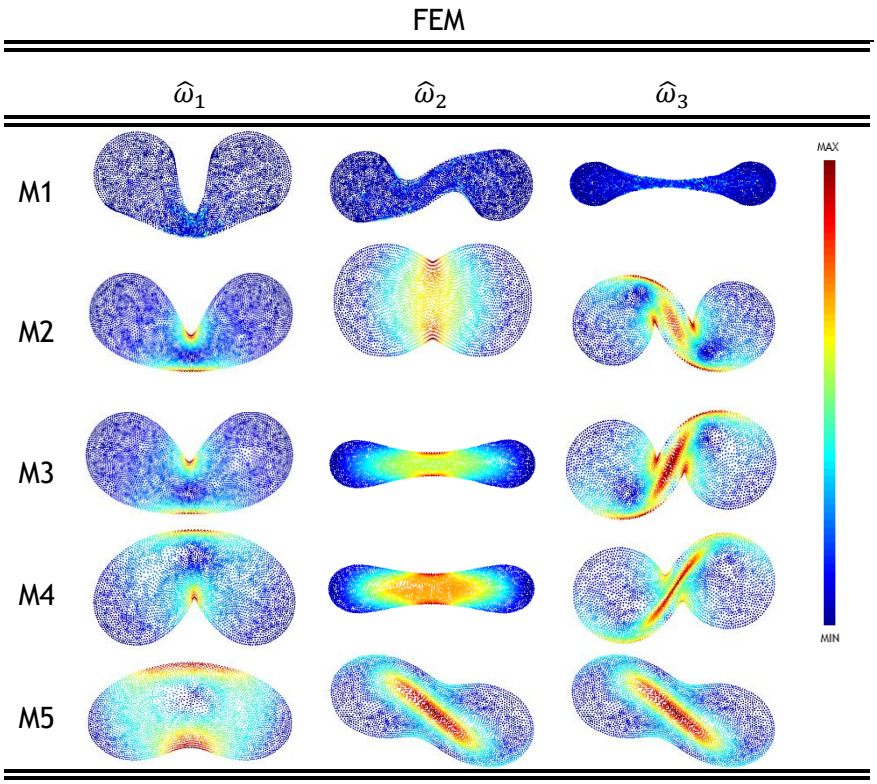

Figure 7. 13 - The potential field of the effective stress of Von Mises 1st ($\widehat{\omega}_1$) , 2nd ($\widehat{\omega}_2$) and 3rd ($\widehat{\omega}_3$) free vibration modes for numerical method FEM and to the 2D ovalocytosis model.

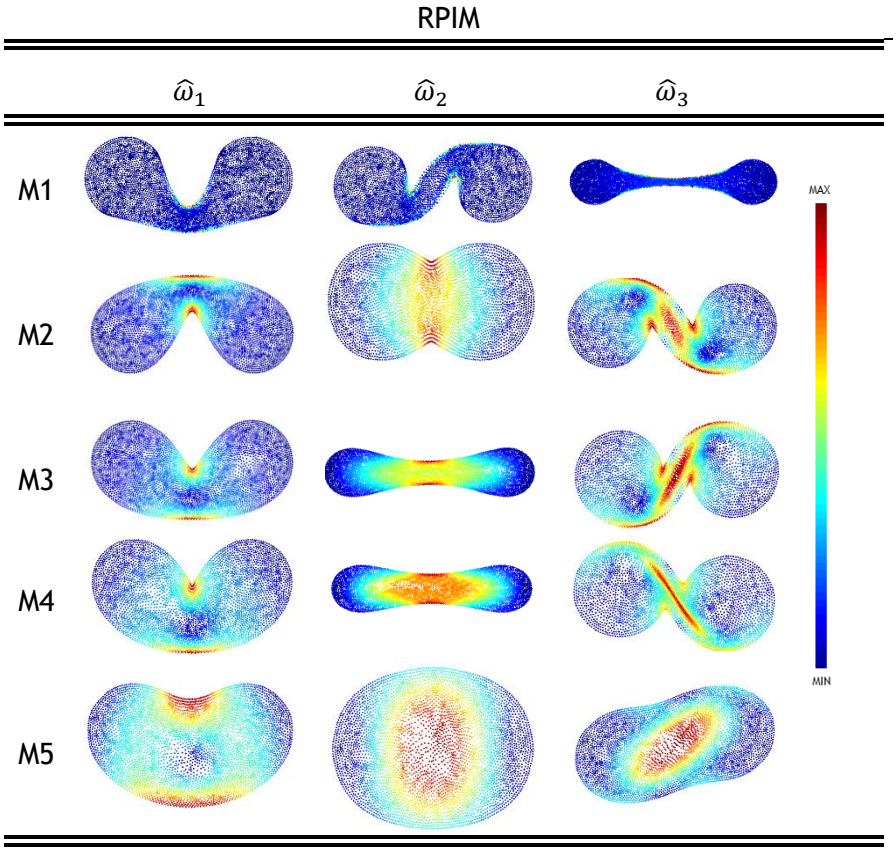

Figure 7. 14 - The potential field of the effective stress of Von Mises of 1st ($\widehat{\omega}_1$) , 2nd ($\widehat{\omega}_2$) and 3rd ($\widehat{\omega}_3$) free vibration modes for numerical method RPIM and to the 2D ovalocytosis model.

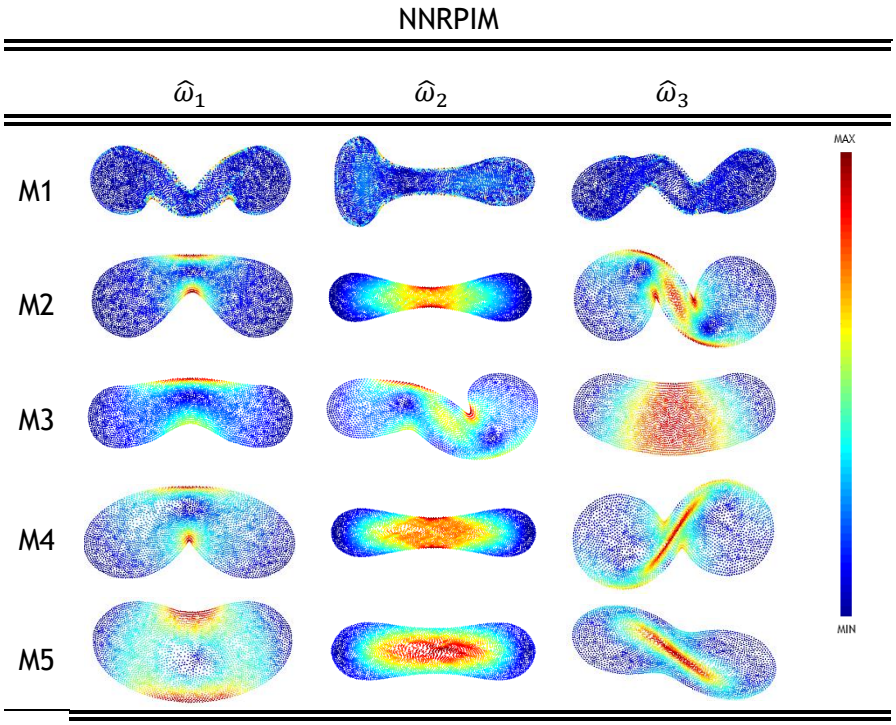

Figure 7. 15 - The potential field of the effective stress of Von Mises of 1st ($\widehat{\omega}_1$) , 2nd ($\widehat{\omega}_2$) and 3rd ($\widehat{\omega}_3$) free vibration modes for numerical method NNRPIM and to the 2D ovalocytosis model.

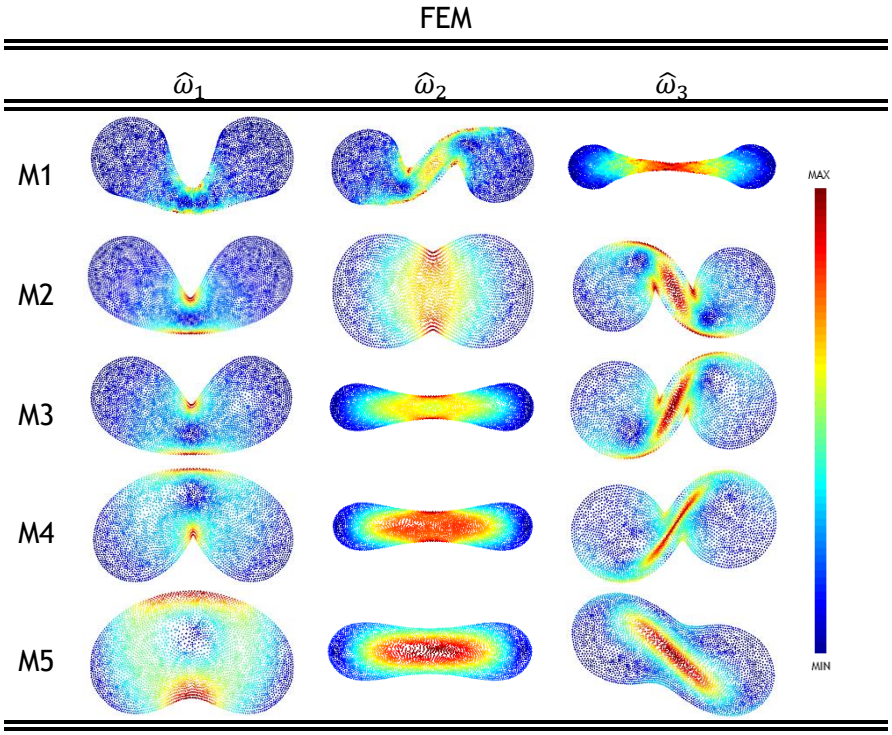

Figure 7. 16 - The potential field of the effective strain of 1st ($\widehat{\boldsymbol{\omega}}_1$) , 2nd ($\widehat{\boldsymbol{\omega}}_2$) and 3rd ($\widehat{\boldsymbol{\omega}}_3$) free vibration modes for numerical method FEM and to the 2D ovalocytosis model.

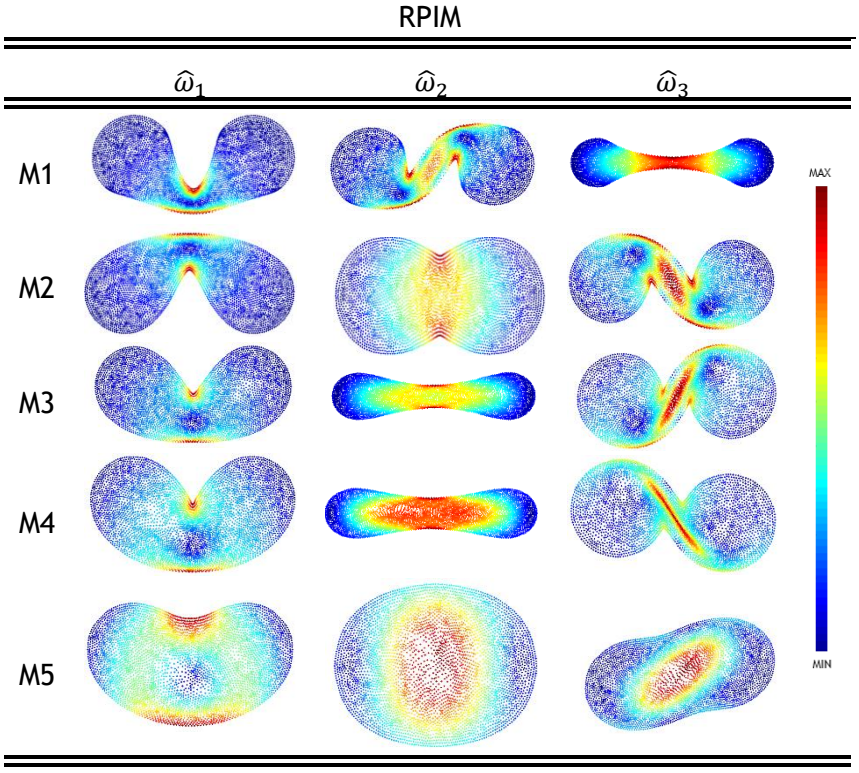

Figure 7. 17 - The potential field of the effective effective strain of 1st ($\widehat{\boldsymbol{\omega}}_1$) , 2nd ($\widehat{\boldsymbol{\omega}}_2$) and 3rd ($\widehat{\boldsymbol{\omega}}_3$) free vibration modes for numerical method RPIM and to the 2D ovalocytosis model.

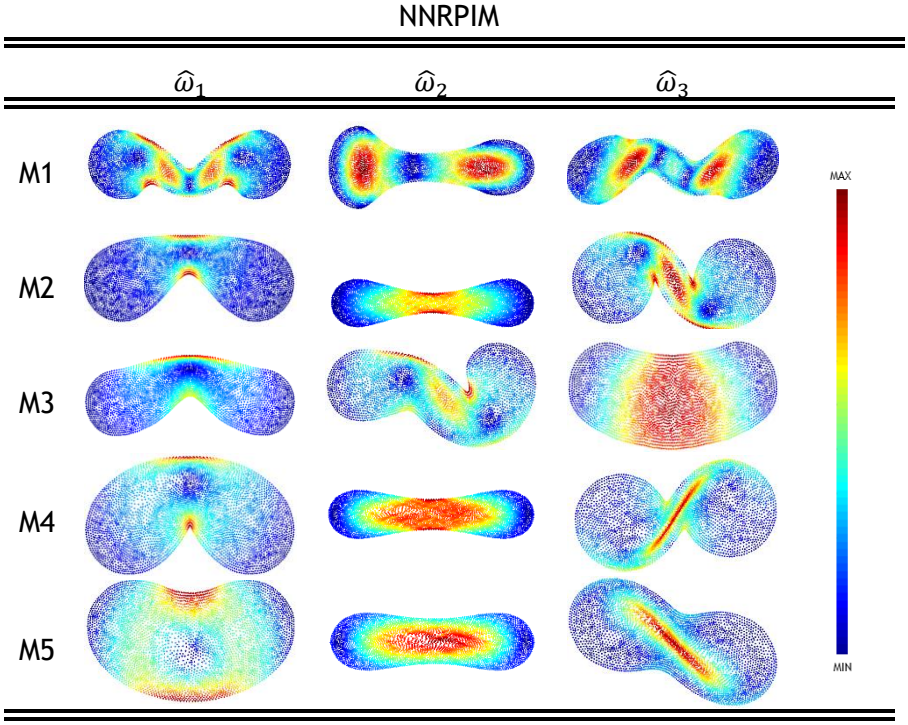

Figure 7. 18 - The potential field of the effective strain of 1st ($\widehat{\omega}_1$) , 2nd ($\widehat{\omega}_2$) and 3rd ($\widehat{\omega}_3$) free vibration modes for numerical method NNRPIM and to the 2D ovalocytosis model.

	Model	E $\times 10^{-8}\, N/\mu m$	$\widehat{\omega}_1$	$\widehat{\omega}_2$ $\times 10^4$	$\widehat{\omega}_3$
FEM	**H**	2,6	3,11	3,11	5,05
	SC	3,7143	8,03	10,18	14,54
	O	8,423	10,59	11,14	12,21
RPIM	**H**	2,6	2,79	2,79	4,45
	SC	3,7143	7,23	8,77	14,17
	O	8,423	10,26	10,76	11,98
NNRPIM	**H**	2,6	4,45	2,80	2,83
	SC	3,7143	14,17	7,26	8,82
	O	8,423	11,98	10,33	10,84

Table 7. 3 - The 1st ($\widehat{\omega}_1$) , 2nd ($\widehat{\omega}_2$) and 3rd ($\widehat{\omega}_3$) free vibration modes for FEM, RPIM and NNRPIM numerical methods and to the 3D models.

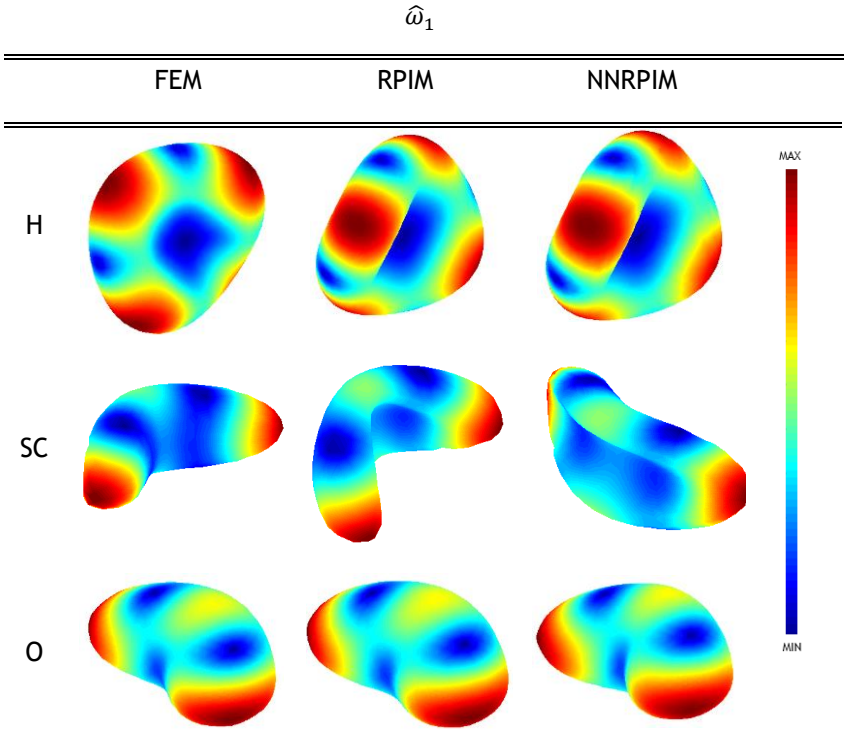

Figure 7. 19 - The 1st $(\widehat{w_1})$ free vibration mode for numerical method FEM,RPIM and NNRPIM to the 3D models.

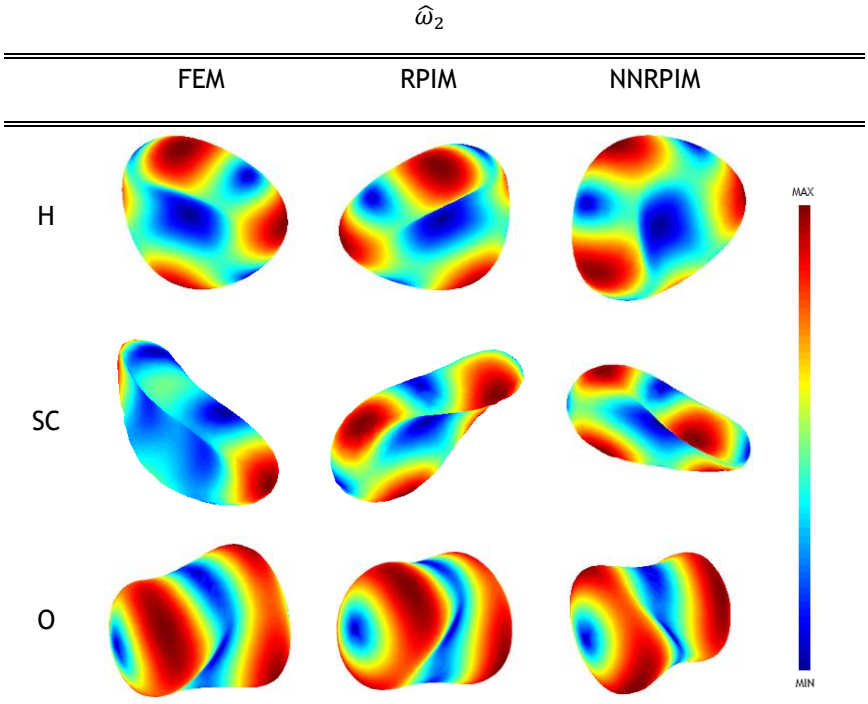

Figure 7.20 - Displacement field of 2nd $(\widehat{w}_2)$ free vibration mode for numerical method FEM,RPIM and NNRPIM to the 3D models.

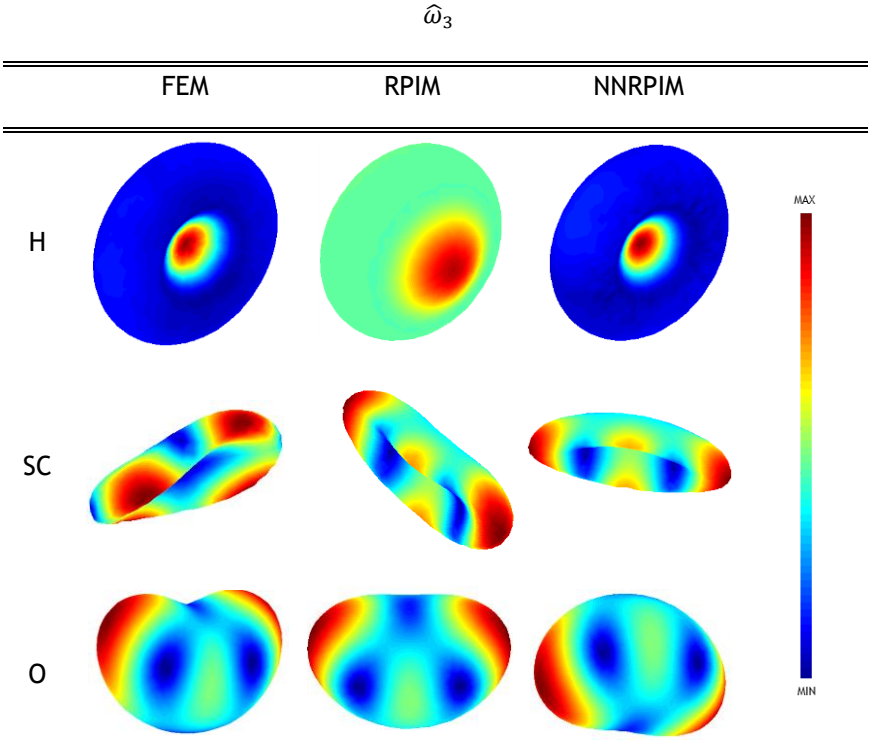

Figure 7.21 - The 3 rd $(\widehat{w_3})$ free vibration mode for numerical method FEM,RPIM and NNRPIM to the 3D models.

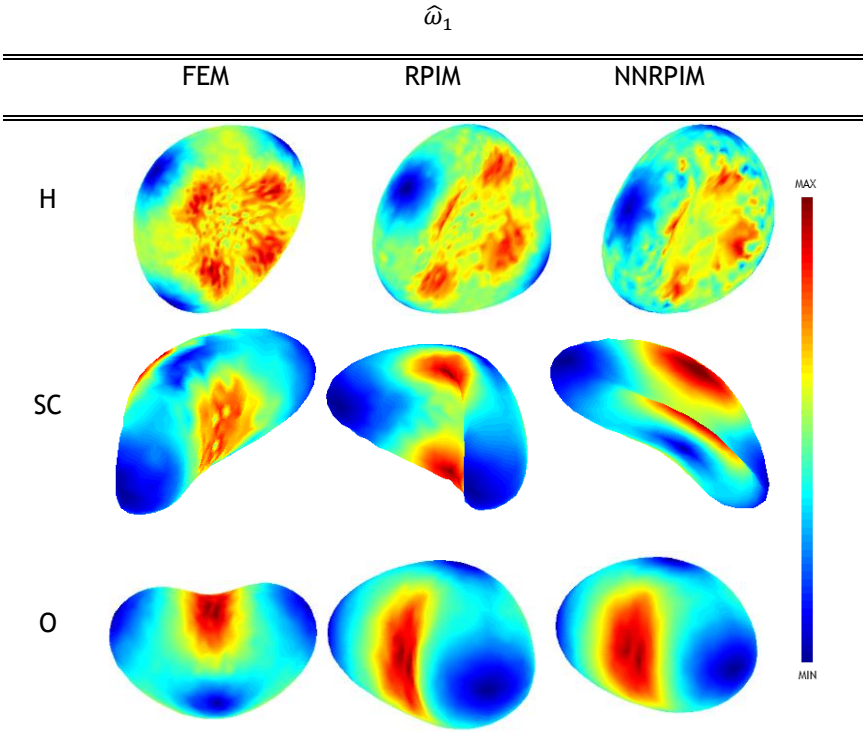

Figure 7. 22 - The potential field of the effective stress of Von Mises of 1st$(\widehat{w_1})$ free vibration mode for numerical method FEM,RPIM and NNRPIM to the 3D models.

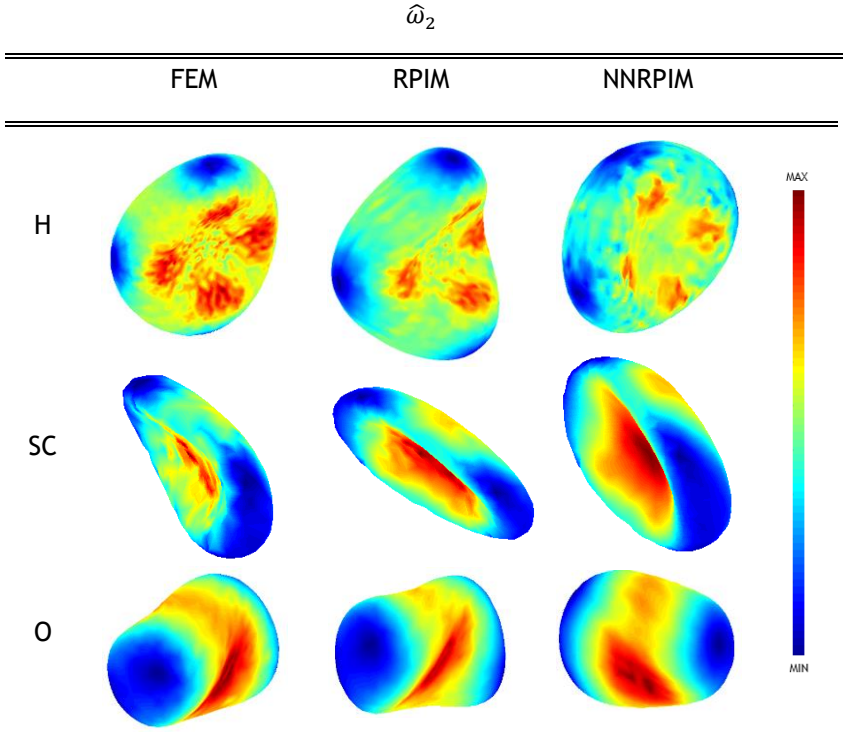

Figure 7.23 - The potential field of the effective stress of Von Mises of 2 [nd] $(\widehat{w_2})$ free vibration mode for numerical method FEM,RPIM and NNRPIM to the 3D models.

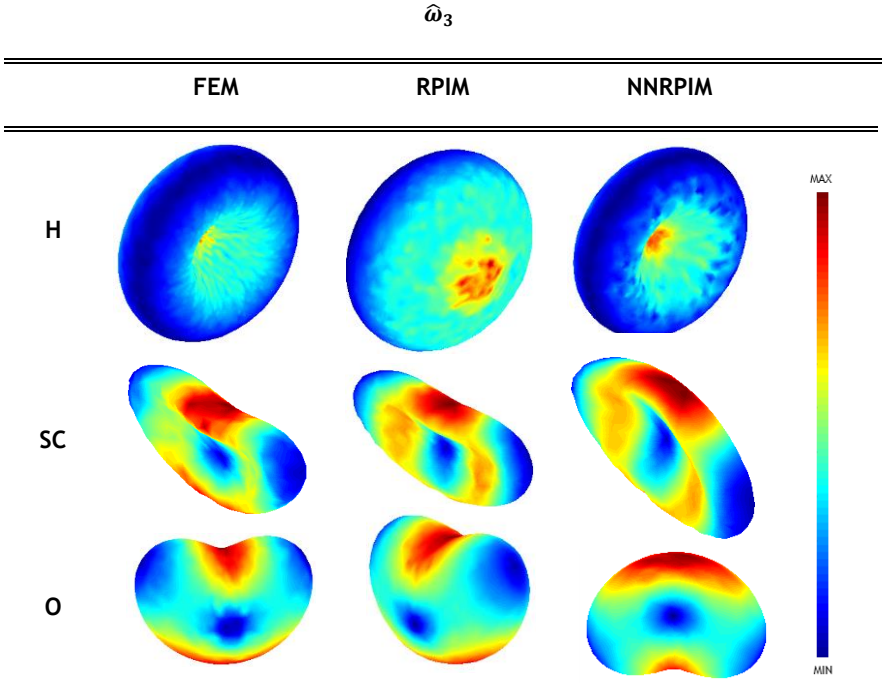

Figure 7.24 - The potential field of the effective stress of Von Mises of 3 [rd] $(\widehat{w_3})$ free vibration mode for numerical method FEM,RPIM and NNRPIM to the 3D models.

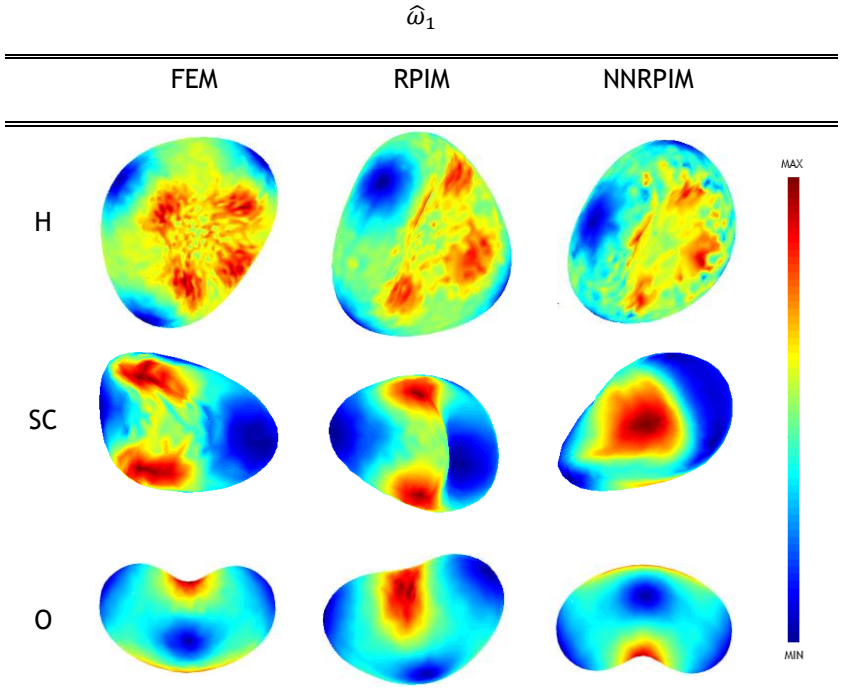

Figure 7. 25- The equivalent potential field of the effective strain of 1st $(\widehat{w_1})$ free vibration mode for numerical method FEM,RPIM and NNRPIM to the 3D models.

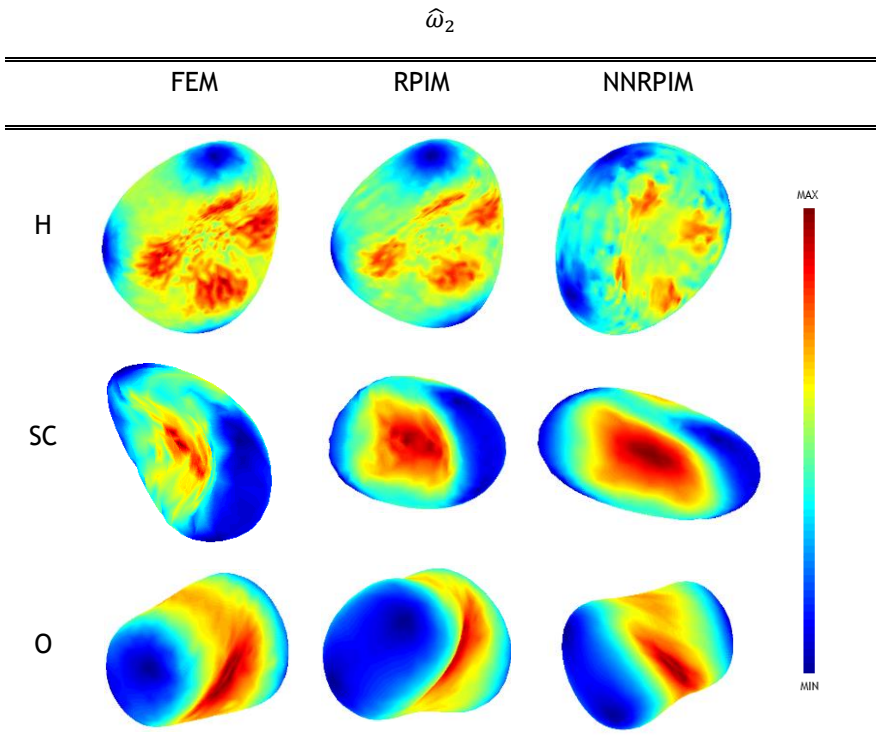

Figure 7.26 - The equivalent potential field of the effective strain of 2 nd $(\widehat{w_2})$ free vibration mode for numerical method FEM,RPIM and NNRPIM to the 3D models.

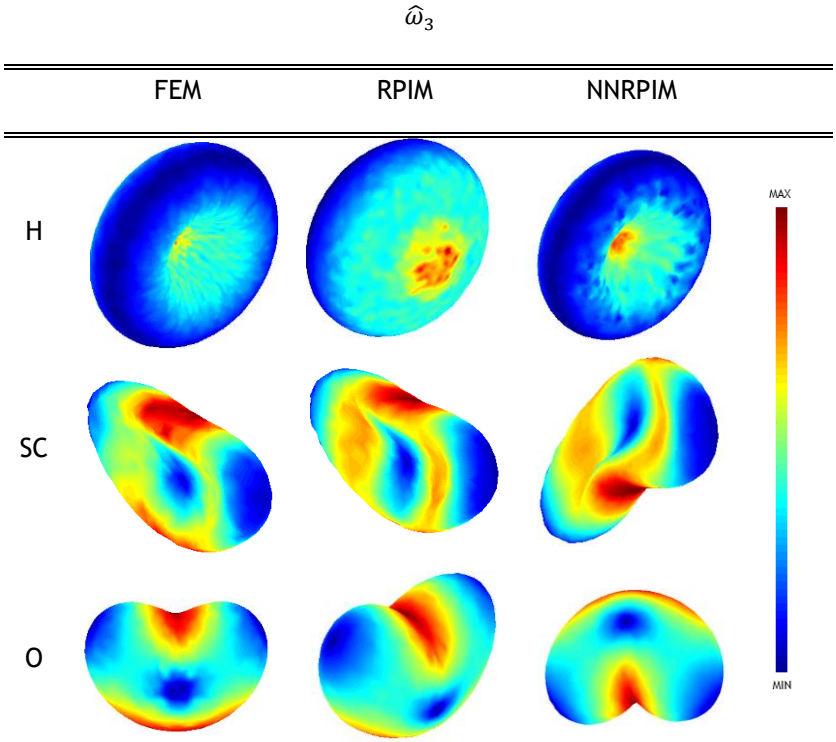

Figure 7.27 - The equivalent potential field of the effective strain of 3 rd $(\widehat{w_3})$ free vibration mode for numerical method FEM,RPIM and NNRPIM to the 3D models.

Chapter 8

Conclusions and Future Work

A profound knowledge of the mechanisms, functions and structure of RBCs is of utmost importance. RBCs appear to exhibit distinct properties in certain pathologies. These pathologies affect the quality of life of millions of people worldwide and entail very expensive costs for families and for the state. In this way, the implementation of biomechanical simulations of RBCs arouses an increased interest.

RBCs are simple biological structures that do not contain intramembrane organelles or nucleus. This feature facilitates the construction of a geometrical model. On the other hand, in the literature, it was not possible to find models indicating the constitution of the membrane and the spectrin network.

The distribution of oxygen and nutrients by the body is ensured by RBCs, as well as the elimination of carbon dioxide (released during the metabolism of all cells in the body). The high deformation capacity of the RBCs allows them to reach all parts of the organism, passing through capillaries of dimensions smaller than their own size.

This work has applied three numerical methods to simulate the mechanical behavior of such bio-structures: the finite element method (FEM) and two meshless methods – radial point interpolation method (RPIM) and the natural neigbhour RPIM (NNPIM). This work allowed to verify that, in fact, the most significant limitation of meshless methods is their high computational cost.

For better results and in order to approximate the results to reality, in the simulations carried out during this dissertation the mechanical properties of healthy RBCs were considered. Being them: the elastic modulus of shear of 5.5 μN/m, the bending elastic modulus $1{,}15 \times 10^{-9}$ nm and the Young's modulus of 26 MPa.

Thus, material elastic assumptions were considered, in both two- and three-dimensional analyses.

Regarding the simulation of RBCs, this work is the first one using RPIM and NNRPIM.

Thus in the present dissertation the static behaviors and the dynamic behavior of different red blood cells were simulated using FEM, RPIM and NNRPIM numerical methods.

The main objective was to determine the first three modes of vibration of three distinct forms of RBC: biconcave disc, sickle and oval. Through this study it was possible to verify that, as expected, each cellular form possesses a unique and characteristic vibration mode.

For the simulations, it has been found that the meshless methods represent a good alternative to the FEM, because the results are very similar to the FEM. In case of complex geometries, the meshless methods are even more advantageous with respect to the FEM, but, as already mentioned, they possess a higher cumputational cost. This fact was verified by the longer simulation time.

With the convergence study, it was also verified that meshless methods converge faster than the FEM.

In the future, it will be interesting to test models that separate the spectrin network from the cell membrane and condider the non-linearity of the material.

Bibliography

Ahmadian, M. T., K. Firoozbakhsh, and M. Hasanian. 2012. “Sharif University of Technology Simulation of Red Blood Cell Motion in Microvessels Using Modified Moving Particle Semi-Implicit Method.” *Scientia Iranica* 19(1):113–18. Retrieved (http://dx.doi.org/10.1016/j.scient.2011.12.007).

Anon. 2009. “Profile of Imported Malaria in Travelers from the North of Portugal.” 2834(Icid):9203.

Apostoli, P. et al. 1988. “Effects of Lead on Red Blood Cell Membrane Proteins.” 71–75.

Bagchi, Prosenjit. 2007. “Mesoscale Simulation of Blood Flow in Small Vessels.” *Biophysical Journal* 92(6):1858–77. Retrieved (http://dx.doi.org/10.1529/biophysj.106.095042).

Belinha, J. 2004. “Análise Elasto-Plástica Considerando O Método Livre de Elementos de Galerrkin.”

Belinha, J. 2014. *Meshless Methods in Biomechanics: Bone Tissue Remodelling Analysis*.

Belytschko, T., Y. Krongauz, D. Organ, M. Fleming, and P. Krysl. 1996. “Meshless Methods: An Overview and Recent Developments.”

Biology, Cell, Leann Tilley, Matthew W. A. Dixon, and Kiaran Kirk. 2011. “The Plasmodium Falciparum-Infected Red Blood Cell Leann.” *International Journal of Biochemistry and Cell Biology* 43(6):839–42. Retrieved (http://dx.doi.org/10.1016/j.biocel.2011.03.012).

Bommer, Christian et al. 2017. “The Global Economic Burden of Diabetes in Adults Aged 20 – 79 Years : A Cost-of-Illness Study.” *Lancet Diabetes Endocrinol* 8587(17):1–8.

Buys, Antoinette V, Mia-jean Van Rooy, Prashilla Soma, Dirk Van Papendorp, and Boguslaw Lipinski. 2013. “Changes in Red Blood Cell Membrane Structure in Type 2 Diabetes : A Scanning Electron and Atomic Force Microscopy Study Changes in Red Blood Cell Membrane Structure in Type 2 Diabetes : A Scanning Electron and Atomic Force Microscopy Study.”

Campilho, R. 2012. *Método de Elementos Finitos*.

Castillo-riquelme, Marianela, Diane Mcintyre, and Karen Barnes. 2008. “Household Burden of Malaria in South Africa and Mozambique : Is There a Catastrophic Impact ?” 13(1):108–22.

Chasis, Joel Anne and Stephen B. Shohet. 1987. “Red Cell Biochemical Anatomy and Membrane Properties.”

Chedlishvili, George M. and Nobuji M. Aeda. 2001. “Blood Flow Structure Related to Red Cell Flow : A Determinant of Blood Fluidity in Narrow Microvessels.” 51(1):19–30.

Cosby, Kenyatta et al. 2003. “Nitrite Reduction to Nitric Oxide by Deoxyhemoglobin Vasodilates the Human Circulation.” 9(12):1498–1505.

Crowl, Lindsay M. and Aaron L. Fogelson. 2010. “Computational Model of Whole Blood Exhibiting Lateral Platelet Motion Induced by Red Blood Cells.” (June 2009):471–87.

Da, Lydie, Julie Galimand, Odile Fenneteau, and Narla Mohandas. 2013. “Blood Reviews Hereditary Spherocytosis , Elliptocytosis , and Other Red Cell Membrane Disorders.” *YBLRE*. Retrieved (http://dx.doi.org/10.1016/j.blre.2013.04.003).

Dai, K. Y. and G. R. Liu. 2006. “Inelastic Analysis of 2D Solids Using a Weak-Form RPIM Based on Deformation Theory.” 195:4179–93.

Dao, M., C. T. Lim, and S. Suresh. 2003. “Mechanics of the Human Red Blood Cell Deformed by Optical Tweezers.” *Journal of the Mechanics and Physics of Solids* 51(11–12):2259–80.

Dinis, L. M. J. S., R. M.Natal Jorge, and J. Belinha. 2009. “Analysis of 3D Solids Using the Natural Neighbour Radial Point Interpolation Method.” 196(2007):2009–28.

Discher, Dennis E., David H. Boal, and Seng K. Boey. 1998. “Simulations of the Erythrocyte Cytoskeleton at Large Deformation . II . Micropipette Aspiration.” *Biophysical Journal* 75(3):1584–97. Retrieved (http://dx.doi.org/10.1016/S0006-3495(98)74076-7).

Elgsaeter, A. and A. Mikkelsen. 1991. “Shapes and Shape Changes Invitro in Normal Red Blood Cells.” *Bio* 1071:273–90.

Ellsworth, M. L. 2000. “The Red Blood Cell as an Oxygen Sensor : What Is the Evidence ?” 551–59.

Evans, E. A., R. Waugh, and L. Melnik. 1976. “ELASTIC AREA COMPRESSIBILITY MODULUS OF

RED CELL MEMBRANE.” 16(1972):585–95.
Fedosov, Dmitry A., Huan Lei, Bruce Caswell, Subra Suresh, and George E. Karniadakis. 2011. “Multiscale Modeling of Red Blood Cell Mechanics and Blood Flow in Malaria.” 7(12).
Fedosov, Dmitry A. and Hiroshi Noguchi. 2013. “Multiscale Modeling of Blood Flow : From Single Cells to Blood Rheology.”
Gallagher, Patrick G. 2004. “Hereditary Elliptocytosis: Spectrin and Protein 4.1R.” 41(2):142–64.
Hamasaki, N. and M. Yamamoto. 2000. “Red Blood Cell Function and Blood Storage.” *Vox Sang* 79(4):191–97. Retrieved (http://content.karger.com/produktedb/produkte.asp?typ=pdf&file=vox79191%5Cnhttp://www.ncbi.nlm.nih.gov/entrez/query.fcgi?cmd=Retrieve&db=PubMed&dopt=Citation&list_uids=11155068).
Hanssen, Eric, Paul J. Mcmillan, and Leann Tilley. 2010. “Cellular Architecture of Plasmodium Falciparum -Infected Erythrocytes.” *International Journal for Parasitology* 40(10):1127–35. Retrieved (http://dx.doi.org/10.1016/j.ijpara.2010.04.012).
Hartmann, Dirk. 2010. “A Multiscale Model for Red Blood Cell Mechanics.” 1–17.
Hennessee, Ian et al. 2017. “Household Costs among Patients Hospitalized with Malaria : Evidence from a National Survey in Malawi , 2012.” *Malaria Journal* 1–12.
Hochmuth, E. A.Evans M. 1976. “Membrane Viscoelasticity.” *Biophysical Journal* 16(1):1–11. Retrieved (http://dx.doi.org/10.1016/S0006-3495(76)85658-5).
Hosseini, S.Majid and James J. Feng. 2009. “A Particle-Based Model for the Transport of Erythrocytes in Capillaries.” *Chemical Engineering Science* 64(22):4488–97. Retrieved (http://dx.doi.org/10.1016/j.ces.2008.11.028).
Hosseini, S.Majid and James J. Feng. 2012. “How Malaria Parasites Reduce the Deformability of Infected Red Blood Cells.” *Biophysj* 103(1):1–10. Retrieved (http://dx.doi.org/10.1016/j.bpj.2012.05.026).
Hyakutake, Toru and Shinya Nagai. 2015. “Numerical Simulation of Red Blood Cell Distributions in Three-Dimensional Microvascular Bifurcations.” *Microvascular Research* 97:115–23. Retrieved (http://dx.doi.org/10.1016/j.mvr.2014.10.001).
Imai, Yohsuke, Toshihiro Omori, Yuji Shimogonya, and Takami Yamaguchi. 2016. “Numerical Methods for Simulating Blood Flow at Macro , Micro , and Multi Scales.” *Journal of Biomechanics* 49(11):2221–28. Retrieved (http://dx.doi.org/10.1016/j.jbiomech.2015.11.047).
Iolascon, A., R. A. Avvisati, and C. Piscopo. 2010. “Hereditary Spherocytosis.” *Transfusion Clinique et Biologique* 17(3):138–42. Retrieved (http://dx.doi.org/10.1016/j.tracli.2010.05.006).
Jensen, F. B. 2004. “Red Blood Cell pH , the Bohr Effect , and Other Oxygenation- Linked Phenomena in Blood O 2 and CO 2 Transport.” 215–27.
Kam, Wing et al. 2006. “Immersed Finite Element Method and Its Applications to Biological Systems.” 195:1722–49.
Kozlov, M. M. and V. S. Markin. 1987. “Model of Red Blood Cell Membrane Skeleton : Electrical and Mechanical Properties.” 439–52.
Krüger, Timm, David Holmes, Peter V Coveney, David Holmes, and Peter V Coveney. 2014. “Deformability-Based Red Blood Cell Separation in Deterministic Lateral Displacement Devices — A Simulation Study Deformability-Based Red Blood Cell Separation in Deterministic Lateral Displacement Devices — A Simulation Study.” 54114.
Lanotte, Luca et al. 2016. “Red Cells ’ Dynamic Morphologies Govern Blood Shear Thinning under Microcirculatory Flow Conditions.” 1–6.
Li, Hua, Ting Ye, and Lam K.Y. 2014. “Computational Analysis of Dynamic Interaction of Two Red Blood Cells in a Capillary.” 673–80.
Li, J., M. Dao, C. T. Lim, and S. Suresh. 2005. “Spectrin-Level Modeling of the Cytoskeleton and Optical Tweezers Stretching of the Erythrocyte.” *Biophysical Journal* 88(5):3707–19. Retrieved (http://dx.doi.org/10.1529/biophysj.104.047332).
Li, Xuejin, Ming Dao, George Lykotra, and George Em. 2017. “Biomechanics and Biorheology of Red Blood Cells in Sickle Cell Anemia.” 50:34–41.
Lim, C. T. and M. Dao. 2004. “Large Deformation of Living Cells Using Laser Traps.” 52:1837–

45.
Liu, Yaling and Wing Kam Liu. 2006. “Rheology of Red Blood Cell Aggregation by Computer Simulation.” 220:139–54.
Melchionna, Simone. 2011. “A Model for Red Blood Cells in Simulations of Large-Scale Blood Flows.” *Macromolecular Theory and Simulations* 20:548–61.
Membrane, Erythrocyte. 1987. “Erythrocyte Membrane Elasticity and Viscosity.” 209–19.
Mohandas, Narla, Patrick G. Gallagher, Narla Mohandas, and Patrick G. Gallagher. 2014. “Red Cell Membrane : Past , Present , and Future ASH 50th Anniversary Review Red Cell Membrane : Past , Present , and Future.” 3939–48.
Mohanty, Joy G. et al. 2010. “Alterations in the Red Blood Cell Membrane Proteome in Alzheimer ’ S Subjects Reflect Disease-Related Changes and Provide Insight into Altered Cell Morphology.” 1–9.
Navidbakhsh, M. and M. Rezazadeh. 2012. “An Immersed Boundary-Lattice Boltzmann Model for Simulation of Malaria-Infected Red Blood Cell in Micro-Channel.” *Scientia Iranica* 19(5):1329–36. Retrieved (http://dx.doi.org/10.1016/j.scient.2012.08.001).
Nayanajith, H., S. C. Saha, and T. Gu. 2013. “Deformation Properties of Single Red Blood Cell in a Stenosed Microchannel.” 1–8.
Paquette, A. M. et al. 2015. “Infection , Genetics and Evolution The Evolutionary Origins of Southeast Asian Ovalocytosis.” *INFECTION, GENETICS AND EVOLUTION* 34:153–59. Retrieved (http://dx.doi.org/10.1016/j.meegid.2015.06.002).
Peng, Zhangli et al. 2013. “Lipid Bilayer and Cytoskeletal Interactions in a Red Blood Cell.”
Pereira, M., H. Carreira, N. Lunet, and A. Azevedo. 2013. “Trends in Prevalence of Diabetes Mellitus and Mean Fasting Glucose in Portugal (1987 E 2009): A Systematic Review.” *Public Health* 128(3):214–21. Retrieved (http://dx.doi.org/10.1016/j.puhe.2013.12.009).
Pierre, Stéphane et al. 2008. “Meshless Methods : A Review and Computer Implementation Aspects.” (October 2017).
Reddy, J. N. 2005. *An Introduction to The Finite Element Method*.
Sabolovic, Domagoj et al. 1997. “Membrane Modifications of Red Blood Cells in Alzheimer â€™ S Disease.” 52(4):217–20.
Shi, Xing, Guang Lin, Jianfeng Zou, and Dmitry A. Fedosov. 2013. “A Lattice Boltzmann Fictitious Domain Method for Modeling Red Blood Cell Deformation and Multiple-Cell Hydrodynamic Interactions in Flow.” (January):895–911.
Shretta, Rima et al. 2017. “Tracking Development Assistance and Government Health Expenditures for 35 Malaria - Eliminating Countries : 1990 – 2017.” *Malaria Journal* 1–11.
Sørensen, M., F. Arneberg, T. M. Line, and T. J. Berg. 2016. “Cost of Diabetes in Norway 2011.” 2:0–8.
Sousa-uva, Mafalda De et al. 2016. “Trends in Diabetes Incidence from 1992 to 2015 and Projections for 2024 : A Portuguese General Practitioner ’ S Network Study.” *Primary Care Diabetes* 10(5):329–33. Retrieved (http://dx.doi.org/10.1016/j.pcd.2016.05.003).
Stauber, Hagit, Dan Waisman, Netanel Korin, and Josué Sznitman. 2017. “Red Blood Cell (RBC) Suspensions in Confined Microflows : Pressure-Flow Relationship.” *Medical Engineering and Physics* 48:49–54. Retrieved (http://dx.doi.org/10.1016/j.medengphy.2017.08.006).
Steck, L. 1974. “THE ORGANIZATION OF PROTEINS IN THE HUMAN RED BLOOD CELL MEMBRANE.” 62(1):1–19.
Suli, E. 2012. “Lecture Notes on Finite Element Methods for Partial Differential Equations.” (December).
Suresh, S. 2006. “Mechanical Response of Human Red Blood Cells in Health and Disease : Some Structure-Property-Function Relationships.”
Szab, Edit. 2015. “Alterations of Membrane Protein Expression in Red Blood Cells of Alzheimer ’ S Disease Patients.” 1:334–38.
Taylor, Publisher et al. 2013. “Computer Methods in Biomechanics and Biomedical Engineering A Review of Numerical Methods for Red Blood Cell Flow Simulation.” (April):37–41.

Tomaiuolo, Giovanna. 2014. “Biomechanical Properties of Red Blood Cells in Health and Disease towards Microfluidics.” *Biomicrofluidics* 8(5).

Trompeter, Sara and May-jean King. 2015. “Hereditary Spherocytosis.” *Paediatrics and Child Health* 25(8):381–86. Retrieved (http://dx.doi.org/10.1016/j.paed.2015.04.003).

Tse, W. T. and S. E. Lux. 1999. “Red Blood Cell Membrane Disorders.” *British Journal of Haematology* 104(2):2–13.

Wang, J. G. and G. R. Liu. 2002. “On the Optimal Shape Parameters of Radial Basis Functions Used for 2-D Meshless Methods.” 191:2611–30.

Wong, P. 2004. “A Hypothesis of the Erythrocyte Rigidity in Southeast Asian Ovalocytosis.” *Medical Hypotheses* 62(6):1024.

Wriggers, P. 2006. *Computational Contact Mechanics*. Retrieved (https://link.springer.com).

Wu, Tenghu, James J. Feng, Tenghu Wu, and James J. Feng. 2013. “Simulation of Malaria-Infected Red Blood Cells in Microfluidic Channels : Passage and Blockage Simulation of Malaria-Infected Red Blood Cells in Microfluidic Channels : Passage and Blockage.” 44115.

Xu, Dong et al. 2013. “Large Scale Simulation of Red Blood Cell Aggregation in Shear Flows.” *Journal of Biomechanics* 46(11):1810–17. Retrieved (http://dx.doi.org/10.1016/j.jbiomech.2013.05.010).

Yawata, Yoshihito. 2003. *Cell Membrane*.

Ye, Ting, Nhan Phan-thien, Boo Cheong Khoo, and Chwee Teck Lim. 2013. “Stretching and Relaxation of Malaria-Infected Red Blood Cells.” *Biophysj* 105(5):1103–9. Retrieved (http://dx.doi.org/10.1016/j.bpj.2013.07.008).

Ye, Ting, Nhan Phan-thien, Boo Cheong Khoo, and Chwee Teck Lim. 2014. “Numerical Modelling of a Healthy / Malaria- Infected Erythrocyte in Shear Flow Using Dissipative Particle Dynamics Method.” *JOURNAL OF APPLIED PHYSICS* 115.

Ye, Ting, Nhan Phan-thien, and Chwee Teck. 2016. “Particle-Based Simulations of Red Blood Cells — A Review.” *Journal of Biomechanics* 2255–66. Retrieved (http://dx.doi.org/10.1016/j.jbiomech.2015.11.050).

Yoon, Daegeun and Donghyun You. 2016. “Continuum Modeling of Deformation and Aggregation of Red Blood Cells.” *Journal of Biomechanics* 49(11):2267–79. Retrieved (http://dx.doi.org/10.1016/j.jbiomech.2015.11.027).